

Unraveling the Relationship Between Molecular Design and Charge Transport in Self-Assembling Systems

Temiz, C.

DOI

[10.4233/uuid:b2a5d49b-f1bf-423c-a7fb-cca7922d80cb](https://doi.org/10.4233/uuid:b2a5d49b-f1bf-423c-a7fb-cca7922d80cb)

Publication date

2024

Document Version

Final published version

Citation (APA)

Temiz, C. (2024). *Unraveling the Relationship Between Molecular Design and Charge Transport in Self-Assembling Systems*. [Dissertation (TU Delft), Delft University of Technology].
<https://doi.org/10.4233/uuid:b2a5d49b-f1bf-423c-a7fb-cca7922d80cb>

Important note

To cite this publication, please use the final published version (if applicable).
Please check the document version above.

Copyright

Other than for strictly personal use, it is not permitted to download, forward or distribute the text or part of it, without the consent of the author(s) and/or copyright holder(s), unless the work is under an open content license such as Creative Commons.

Takedown policy

Please contact us and provide details if you believe this document breaches copyrights.
We will remove access to the work immediately and investigate your claim.

**Unraveling the Relationship
Between Molecular Design and
Charge Transport in Self-
Assembling Systems**

Cansel TEMIZ

Unraveling the Relationship Between Molecular Design and Charge Transport in Self-Assembling Systems

Dissertation

for the purpose of obtaining the degree of doctor
at Delft University of Technology
by the authority of the Rector Magnificus Prof. dr. ir. T.H.J.J. van der
Hagen chair of the Board for Doctorates,

to be defended publicly on
18th of April 2024 at 10:00 o'clock

by

Cansel TEMIZ

Master of Science in Polymer Science and Technology
Middle East Technical University, Türkiye
born in Ankara, Türkiye

This dissertation has been approved by the promotor.

Prof. dr. F.C. Grozema promotor	Delft University of Technology,
Dr. R. Eelkema promotor	Delft University of Technology,

Composition of the doctoral committee:

Rector Magnificus	chairperson
Prof. dr. F.C. Grozema promotor	Delft University of Technology,
Dr. R. Eelkema promotor	Delft University of Technology,

Independent members:

Prof. dr. J.H. Van Esch	Delft University of Technology
Prof. dr. A.J. Houtepen	Delft University of Technology
Dr. A.G. Denkova	Delft University of Technology
Prof. dr. VanderZande	Hasselt University, Belgium

Other members:

Prof. dr. S.J. Picken	Delft University of Technology
-----------------------	--------------------------------

This work received financial support from the European Research Council Horizon 2020 ERC Grant Agreement No. 648433



European Research Council

Established by the European Commission

Table of Content

Chapter 1 – Introduction	1
Chapter 2 – Synthesis & Optical Spectroscopy of Discotic Hexa-<i>peri</i> hexabenzocoronene Derivatives: Self-Assembly Properties of Molecular Nanowires in Solution	57
Appendix	93
Chapter 3 – Supramolecular Organization and Charge Transport Properties of Hexa-<i>peri</i>-hexabenzocoronene Derivatives: Self-Assembly Molecular Nanowires in the Solid State	101
Chapter 4 – Charge Carrier Transport Properties of Symmetric Alkyl[1]Benzothieno[3,2-<i>B</i>][1]Benzothiophenes	123
Chapter 5 – Semiconducting Polyamides with Enhanced Charge Carrier Mobility	151
Summary	171
Samenvatting	177
Acknowledgement	183
List of Publications	189
Curriculum Vitae	191

Chapter 1

Introduction

1.1. Introduction

Since the dawn of organic electronics in the 1970s that led to the discovery of organic photovoltaic cells (OPVs)¹, light-emitting diodes (LEDs)² and field-effect transistors (FETs)³, the interest in organic optoelectronic devices and organic molecular design has gradually increased, both in academia and in industry. Advantageous characteristics of organic semiconducting materials include potential low cost-fabrication, environmental friendliness, low weight, mechanical flexibility, easier processability, and extensive non-toxic material design options.⁴ The performance of these materials has continually improved, making them increasingly attractive for applications. Although the power conversion efficiencies of organic photovoltaic cells (OPV) have been hovering in the 11-12% range for a long time, during the last few years, rapid increases have been reported, mainly because of the introduction of non-fullerene electron acceptors. The current record for OPV is well-above 17%,⁵ which is still lower than record single-junction perovskite (25.2%) and silicon (26.7%) efficiencies.⁶

In all device applications for organic semiconductors, achieving efficient charge transport, and hence a high charge carrier mobility, is crucial to optimization. The charge carrier mobility depends on the intrinsic electronic properties and the microscopic and macroscopic molecular order in the solid-state. In addition, the presence of (structural) defects plays a key role.^{7,8} While organic semiconductors have many possible advantages over inorganic materials, the reported mobilities in organic semiconductors are not yet comparable to those of state-of-the-art

inorganic semiconductors. AlGaAs/GaAs heterostructures exhibit high mobility values of approximately $35 \times 10^6 \text{ cm}^2/\text{Vs}$.⁹ For single silicon crystals, the electron mobility is $10^3 \text{ cm}^2/\text{Vs}$,¹⁰ while for perovskites values up to $600 \text{ cm}^2/\text{Vs}$ have been reported.¹¹ In contrast, the reported values are typically several orders of magnitude smaller for organic semiconductors, with the highest values in the range of $1\text{-}43 \text{ cm}^2/\text{Vs}$ for highly ordered systems.¹²⁻¹⁵

Conjugated liquid crystalline materials are a subgroup of organic semiconductors exhibiting a relatively high charge carrier mobility (up to $1 \text{ cm}^2/\text{Vs}$)¹⁶. Still, they are typically lower than crystalline materials due to the substantial orientational disorder.¹⁷ However, they offer several advantages, including easier processability, absence of grain boundaries, self-alignment between electrodes, and self-healing capabilities.¹⁸ Despite the relatively low charge carrier mobilities, conjugated liquid crystalline materials have been successfully applied in OPV devices where the active layer consists of a blend of two types of discotic liquid crystals (hexabenzocoronene and perylene diimide) . In such a device, a single-wavelength (490 nm) external quantum efficiency as high as 34% was reported.¹⁹

It is clear from this discussion that the charge carrier mobility in organic semiconductors, and conjugated liquid crystalline materials in particular, is intricately linked to the structural order in the materials on a microscopic level. Substantial improvements in mobility and an improved fundamental understanding are necessary to achieve the desired results and to engineer the packing in the materials on a molecular level. Liquid crystalline organic semiconductors are of particular interest in this regard since they explicitly rely on self—organization to form their semi-

organized liquid crystalline state. This thesis explores approaches to achieve control over the solid-state packing of these materials by explicitly engineering the intermolecular interactions between the molecules.

In the remainder of this chapter, an overview of the structure and properties of liquid crystalline materials and approaches to study charge transport in these materials are discussed. In addition, an outline of the remainder of this thesis is given.

1.2. Liquid crystals

Liquid crystals were first discovered in 1888 by Austrian botanist Friedrich Reinitzer working on crystals of cholesteryl benzoate extracted from carrot root.²⁰ Unexpectedly, the molecules exhibited two distinct melting points. The ‘first’ melting point was the temperature at which the crystal solid turned into a milky fluid and became perfectly transparent at the ‘second’ melting point, called the clearing point. Soon after this initial observation, the crystallographer Otto Lehmann analysed the intermediate cloudy phase using polarised light. In the intermediate phase, the material had characteristics of both a liquid and a solid, i.e., a solid material that flows. This ‘new’ state of matter, combining the fluidity of liquids and the orientational order of solids, led Lehmann²¹ to coin the term ‘liquid crystals’ in 1889 and has been regarded as the fourth state of matter since then.

Liquid crystalline materials (LCs) can be classified by the process of obtaining the liquid crystalline phase transition: thermotropic and lyotropic LCs. Thermotropic LCs exhibit phase transitions on changing the temperature. In addition to temperature effects, lyotropic LCs display phase transitions on adding a solvent, which can be either a concentration effect or involve specific solvation. Molecules that form liquid crystalline phases are referred to as mesogens. Depending on the anisotropic shape of the molecules, LCs can be subdivided into calamitic mesogens (rod-like), discotic mesogens (disc-like), and banana-shaped mesogens

(Figure 1.1.). In this thesis, only calamitic and discotic mesogens are considered.

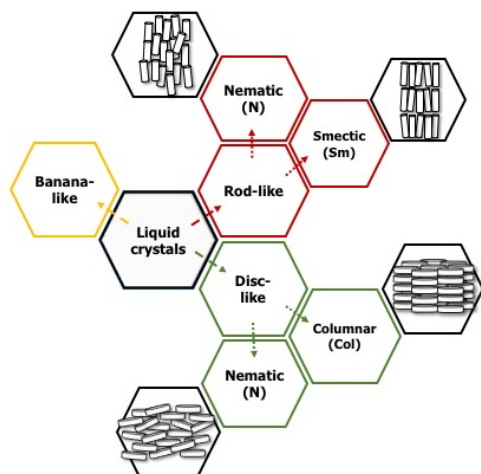


Figure 1.1. Classification of liquid crystals mesogens and their mesophases

Most liquid crystalline molecules consist of a rigid, π -conjugated core surrounded by flexible solubilizing side chains. These two distinct molecule parts give rise to different intermolecular interactions that lead to specific self-assembling properties. For instance, rigid conjugated cores tend to show relatively strong π -stacking interactions, while flexible alkyl chains do not. These distinct interactions related to different parts of the molecules can lead to materials that exhibit properties of both solids and liquids. The self-organization of liquid crystalline molecules is an energy minimization process where disorganized free molecules in solution or solid-state autonomously form stable and structurally well-defined arrangements through weak non-

covalent bonds and interactions, including π -stacking, Van der Waals interactions, ionic interaction, and hydrogen bonds.^{22,23} Since self-assembly is a reversible process, the bonds between the aggregated molecules should be of the same order of magnitude as the forces (Table 1.1.) that counteract assembly (thermal motion, mechanical stress).²⁴

Table 1.1. Energies of various non-covalent bonds and interactions²⁴

Type of bonding or interaction	Energy (kJ/mol)
Covalent bond	100-400
Coulomb	250
Hydrogen bond	4-120
Ion-ion	200-300
Ion-dipole	50-200
Dipole-dipole	5-50
Cation- π	5-80
π - π	0-50
Van der Waals forces	<5
Hydrophobic effects	Related to the solvent-solvent interaction energy
Metal-ligand	0-400

The self-assembly process in mesogens can be controlled by manipulating the weak intermolecular interactions between the different parts of neighbouring molecules. Neighbouring, rigid

aromatic cores of LC molecules interact relatively strongly by π - π -interactions, while alkyl chains interact much more weakly. This can result in a situation where the overall order in the solid is preserved by the aromatic units, while the surrounding alkyl chains can become liquid-like upon heating. The transition between the various types of mesophases, decreasing structural order from crystalline to smectic to nematic and finally to the isotropic phase, occurs at defined temperatures based on the molecular structure and packing characteristics of the molecules.

1.1.1. Calamitic mesogens: structural order

Ever since the discovery of cholesteryl benzoate liquid crystalline molecules, rod-like (calamitic) liquid crystals have been extensively used in display applications due to their optoelectronic properties. The pioneering work of Hanna and Funahashi showed temperature-dependent charge transport properties of such molecules in the liquid crystalline state, 2-(4'-heptyloxyphenyl)-6-dodecylthiobenzothiazole (7O-PBT-S12), yielding hole mobility of $5 \times 10^{-3} \text{ cm}^2/\text{Vs}$ in time-of-flight measurements.²⁵ Most rod-like liquid crystalline molecules have an elongated shape and consist of a rigid core with terminal and/or lateral solubilizing chains (Figure 1.2.) attached to it. The elongated shape of the molecule, combined with the π -conjugated nature of the cores, leads to a structure in which the elongated molecules are packed parallel to each other. This allows the rigid cores to approach each other more closely, resulting in stronger attractive Van der Waals forces. The

molecular order in mesophases can be enhanced by introducing groups capable of hydrogen bonding or other directional interactions.²⁶

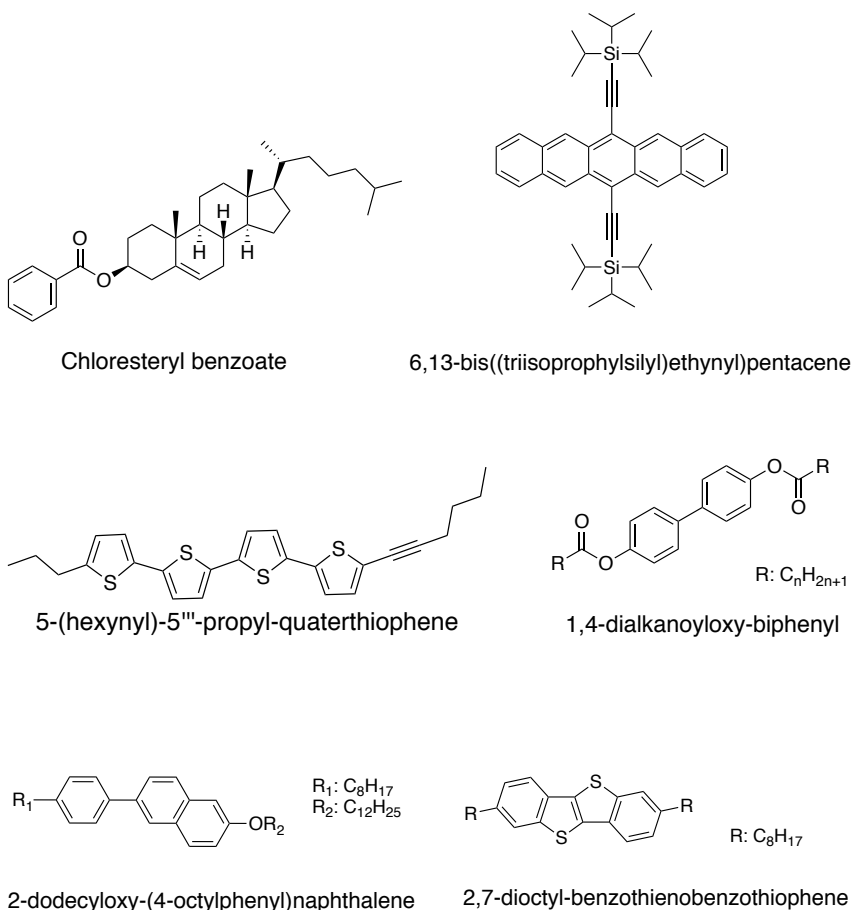


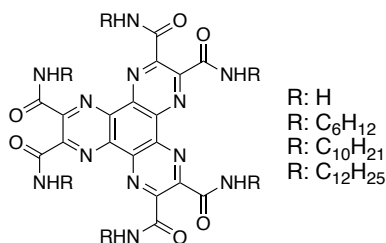
Figure 1.2. Common examples of rod-like liquid crystalline molecules with varying π -conjugated cores and solubilizing side chains^{20,27,28}

Rod-like liquid crystalline molecules exhibit two main mesophases: the nematic phase (N) and the smectic phase (Sm). The nematic phase is the least ordered of the two and is closest to the isotropic phase with a high degree of long-range orientational order but no long-range positional order. By increasing the size of the rigid core, one can achieve the more ordered smectic phase due to increased intermolecular interactions.²⁹ In this mesophase, the molecules possess both positional and orientational order. The rod-like molecules are arranged in layers and can exhibit two-dimensional charge carrier transport through the layer of rigid cores. Various types of smectic phases can be observed depending on the molecular order in the layers. In the smectic-A phase, molecules are aligned perpendicular to the layers, while in the smectic-C phase, molecules are tilted to the plane of the layer. There is no long-range positional order within the layers in these smectic phases. The smectic-B phase is the most ordered smectic phase because molecules are arranged in a hexagonal crystalline order within layers.³⁰

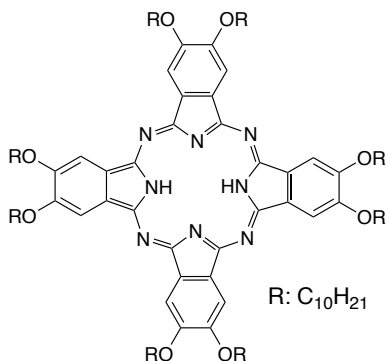
1.1.2. Discotic mesogens: Structural order

Disc-like (or discotic) liquid crystalline (DLC) molecules were first observed in 1977 by Chandrasekhar et al., who studied the phase transition behaviour of benzene with six ester side groups.³¹ Discotic liquid crystalline (DLC) molecules consist of rigid, flat π -conjugated cores surrounded by long, flexible, solubilizing alkyl chains in the periphery (Figure 1.3.). Due to

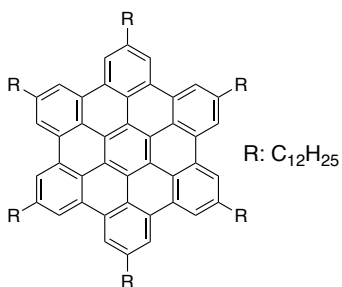
tightly overlapping π -systems in each disc-like core, they self-assemble into one-dimensional aromatic stacks that provide efficient pathways for charge transport in one dimension (Figure 1.4.a).



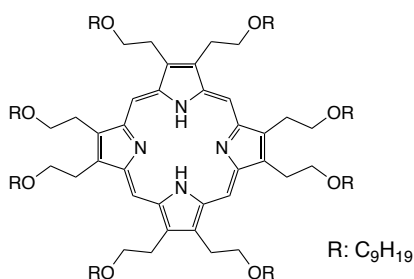
Hexacarboxamidohexaazatriphenylene



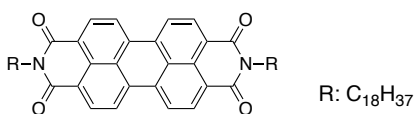
octakis(decyloxy)phthalocyanine



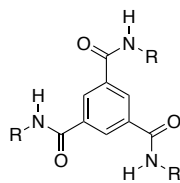
hexadecylhexabenzocoronene



octakis(2-(nonyloxy)ethyl)porphyrin



N,N'-dialkylatedperylene-tetracarboxydiimides



Benzene-1,3,5-tri-carboxamides (BTAs)

Figure 1.3. Common examples of disc-like liquid crystalline molecules with varying π -conjugated cores and solubilizing side chains^{32–38}

In general, four main types of intermolecular interactions can be classified: electrostatic interaction (dipole-dipole or, more commonly, quadrupole-quadrupole interactions), dispersion forces (London dispersion, or attractive Van der Waals interactions), induction interactions (dipole-induced-dipole), and Pauli repulsion (short-range repulsion).³⁹ In the case of the core of a DLC molecule (a polycyclic aromatic hydrocarbon), the dipole moment is often zero or very small due to the high symmetry. However, π -conjugated molecules usually have a substantial quadrupole moment. In the solid-state, the planar DLC molecules can approach each other closely at π - π stacking distances close to 3.5 Å. This close interaction optimizes the attractive dispersion forces that strongly increase with decreasing distance. Forming such face-to-face stacked structures leads to repulsive electrostatic interactions due to quadrupole-quadrupole interactions.

Balancing attractive dispersion and repulsive electrostatic interactions generally leads to parallel-displaced geometries for unsubstituted conjugated cores, where the electrostatic repulsion is minimized or even becomes attractive. The interaction between the cores can be tuned by extending the core size, introducing heteroatoms in the core, or selecting appropriate side chains. In addition, hydrogen bonding interactions or dipole-dipole interactions can

increase the intermolecular interaction or modify the stacking geometry.

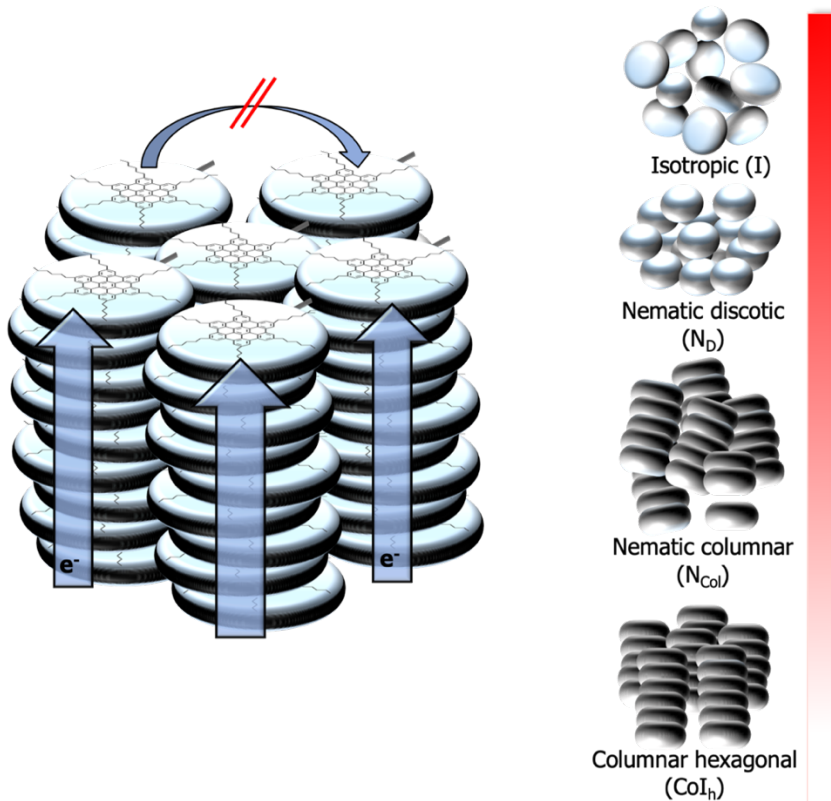


Figure 1.4. a) Representation of the one-dimensional charge transport pathway in self-assembled discotic liquid crystals b) Mesogens in thermotropic discotic liquid crystals

DLCs can form two types of mesophases: nematic (N) and columnar (Col) phases. The nematic phase has orientational order of the discs along a common direction without translational order in any direction. Stacking disc-like molecules into 1D columns with orientational and positional order results in a higher-order

columnar phase. The neighboring aromatic cores are tightly stacked, resulting in strong electronic interactions and hence a much higher charge carrier mobility than in the corresponding nematic phase (Figure 1.4.b). The cofacial distance, d_c , and intracolumnar distance, d_i , parameters between neighbouring molecules within the columnar stacks give insight into intracolumnar charge transport. In the crystalline phase (K), the discs form a tilted columnar structure with a tilt angle close to 45° along the column, i.e., the molecules adopt a parallel-displaced geometry. For DLCs in the crystalline phase, the d_c varies from 3.3 Å to 3.6 Å while d_i is in the range of 4.2- 4.8 Å. In addition to the centre-to-centre distance between the molecules, the twist angle between neighbouring molecules also plays a significant role in determining the charge transport properties, as will be discussed in Chapter 3. A larger distance (20-40 Å) between neighbouring columns (intercolumnar distance, L) leads to a more isolated structure that prevents recombination of charges in different columns.⁴⁰

The discotic molecules stack in a horizontal columnar arrangement where $d_c = d_i$ in the columnar phase. Resulting from the specific intermolecular interactions between neighbouring molecules, different degrees of internal order within the columns can be obtained: ordered (Col_o), disordered (Col_d), plastic (Col_p), and helical (H). In addition, the columnar stacks can tilt to the columnar axis, which gives rise to different two-dimensional intercolumnar lattice arrangements: hexagonal lattice (Col_h), rectangular lattice (Col_r), and oblique lattice (Col_{ob}).

1.1.3. Mesophase characterization

The phase behaviour of thermotropic liquid crystalline materials is characterized by the orientational, positional, and bond orientation order of the molecules they consist of. The differences in the types of order as a function of temperature are directly related to the intermolecular interactions between the aromatic cores and the solubilizing side chains. To characterize the different phases, the structural parameters mentioned above should be measured directly or indirectly derived from a measurement. Standard techniques that are used to indicate mesophases are polarized optical microscopy (POM), differential scanning calorimetry (DSC), and powder X-ray diffraction (XRD) studies. The static and dynamic structural properties of the discotic molecules in the solid-state can also be measured using solid-state nuclear magnetic resonance (NMR) methods. However, this is beyond the scope of this thesis.

From a DSC measurement, information is obtained on phase transition temperatures and enthalpy changes (ΔH) during the different transitions. This can also indirectly indicate the structural changes since a large value of ΔH generally indicates a significant structural difference between two mesophases. Large values for ΔH are often associated with a solid-to-mesophase transition (for instance, the melting of the flexible side chains in a discotic material) and mesophase-to-isotropic liquid transition. Mesophase-to-mesophase transitions usually result in much smaller values of

ΔH . It is possible to assign the microscopic birefringent appearance of the optical textures, which arise due to the polarizability anisotropy of the liquid crystalline molecules, by POM measurements. The change in the anisotropy while going through a phase transition changes the birefringent appearance. The magnitude and sign of the change in birefringence around specific phase transitions observed in DSC measurements can give information on the structural changes in the molecular order during the phase transition.^{41,42}

Powder X-ray crystallography is a more direct way to study structural changes during phase transitions. X-ray crystallography generally requires long-range order to yield sharp diffraction peaks, from which a detailed picture of the solid-state structure can be derived. This is possible in the crystalline phase, whereas the considerable disorder in the mesophases makes it impossible to obtain detailed structural information. Nevertheless, XRD can give valuable insight into the structure, even for partially disordered systems. In the small-angle region, data is received on the intercolumnar distance. At the same time, wide-angle reflections can be assigned to the order between neighbouring molecules within the column, for instance, the π stacking distance. In most cases, a combination of the techniques discussed here is required to assemble a picture of the structural parameters of an LC material.

1.2. Charge transport in organic molecular material

Organic semiconductors cover a wide variety of π -conjugated

materials ranging from disordered conjugated polymers to disordered small-molecule materials to highly crystalline materials. Semiconducting liquid crystalline materials can be considered amorphous and crystalline, usually forming relatively ordered one- or two-dimensional environments for charge transport.⁴³ As mentioned above, for application of these materials in optoelectronic devices such as solar cells⁴⁴, light-emitting diodes⁴⁵ and field-effect transistors⁴⁶, an essential requirement is that they can efficiently transport charge. The electrical conductivity of a material, σ (S/m), is defined as the amount of charge that is transported across a unit cross-sectional area, per time, per unit of the applied electric field. The conductivity is related to the concentration of charges and how fast they can move in an applied electric field by:

$$\sigma = n_e \mu_e e + n_h \mu_h e \quad (1.1)$$

Where n_e and n_h are the number densities (m^{-3}) of electrons and holes, respectively, μ_e and μ_h are the electron and hole mobility (m^2/Vs), and e is the elementary charge (1.602×10^{-19} C). Based on their ability to conduct charges, materials can be roughly divided into three categories: conductors/metals ($\sigma \geq 10^3$ S/cm), semiconductors ($10^3 \geq \sigma \geq 10^{-12}$ S/cm) and insulators ($\sigma \leq 10^{-12}$ S/cm).⁴⁷ To achieve effective conductivity, materials must possess two fundamental attributes:

- A high concentration of charges
- Efficient transport of those charges, as reflected in a

high charge carrier mobility

In most of the organic materials, the intrinsic concentration of charges is very low due to their relatively large bandgap. Yet, the charge carrier mobility in (organic) semiconductors can be higher than in metals.⁴⁸ The latter shows that the concentration of charges, which is very high in metals, is equally important in determining the conductivity of material as the mobility is. For the remainder of this discussion, we relate to the charge carrier mobility as this is a material-specific quantity independent of how charges are generated. The latter can be highly dependent on the device structure and measurement techniques used.

Charge transport in discotic liquid crystals

While there are some reports of very high charge carrier mobilities in organic materials, in most cases, mobilities are rather low due to considerable disorder in the molecular packing on local (amorphous/crystalline) and on macroscopic (grain boundaries) length scales. Liquid crystalline molecules offer some directions to avoid this problem via their thermally controlled molecular packing properties, i.e. mesophases, as mentioned in section 1.1. Disc-like liquid crystalline molecules self-organize into columnar phases where the charge transport is limited to one dimension. For such columnar mesophases, the mobility generally increases as the intra-columnar order is increased. The highest reported mobility for a discotic liquid crystalline material is ca. $1.1 \text{ cm}^2/\text{Vs}$ for a

hexabenzocoronene derivative.¹⁶ Peripheral substituents are introduced in DLCs to enhance liquid crystallinity, and their length and nature can strongly affect the disorder in the π -stack. Increased static and dynamic disorder along the stack results in lower charge carrier mobilities. The amount of disorder along the stack is also determined by the interaction between the aromatic core and hence depends on their structure. As an example, for triphenylenes, mobilities in the range of 10^{-2} - 10^{-4} cm^2/Vs have been reported for aliphatic side chains containing 3 to 11 carbon atoms.⁴⁹ Optimization of the sidechains has been shown to lead to more ordered stacking of triphenylene derivatives resulting in the mobility of 0.1 cm^2/Vs in the liquid crystalline phase and 0.3 cm^2/Vs in the crystalline phase.⁵⁰

Larger aryl cores, such as hexabenzocoronenes, more strongly interact, primarily through dispersion interactions, leading to less disordered stacking arrangements. This results in considerably higher mobilities, up to 1.1 cm^2/Vs in the helical columnar phase for substitution with linear dodecyl chains.¹⁶ Branching in the alkyl side chains leads to steric hindrance, especially if the branching is close to the aromatic core, resulting in decreases the π interactions between neighbouring HBC cores, and hence a lower charge carrier mobility.⁵¹

Charge transport in calamitic liquid crystals

In the case of rod-like liquid crystalline materials, the individual molecules self-assemble into lamellar layered structures

and form smectic phases where the charge transport is two-dimensional. The most representative and widely studied examples are acene molecules such as tetracene and pentacene derivatives that exhibit high record mobilities, up to $40 \text{ cm}^2/\text{Vs}$ for pentacene single crystals⁵² and $43 \text{ cm}^2/\text{Vs}$ for rubrene single crystals.⁵³ For a heteroacene derivative, benzo[thieno[3,2-b][1]benzothiophene (BTBT), an exceptionally high charge carrier mobility of $31.3 \text{ cm}^2/\text{Vs}$ for organic thin-film transistors has been reported.⁵⁴ These values are all for highly crystalline materials without flexible sidechains introducing liquid crystallinity. Introducing such a side chain usually results in more disordered materials, hence lower charge carrier mobilities. Nevertheless, Seki and co-workers have recently reported a very high mobility value, $170 \text{ cm}^2/\text{Vs}$ for holes in a liquid crystalline BTBT derivative, 2,7-didodecyl-BTBT.⁵⁵ The details of this record charge carrier mobility are discussed in Chapter 4.

1.3. Mechanisms of charge transport

From the discussion above, it is clear that the static and dynamic structural parameters determine the magnitude of the charge carrier mobility. The magnitude of the charge carrier mobility is determined by the disorder in the energetic landscape that the charge encounters and the electronic interactions between the neighbouring molecules. These parameters are directly related to the structural disorder in the material.

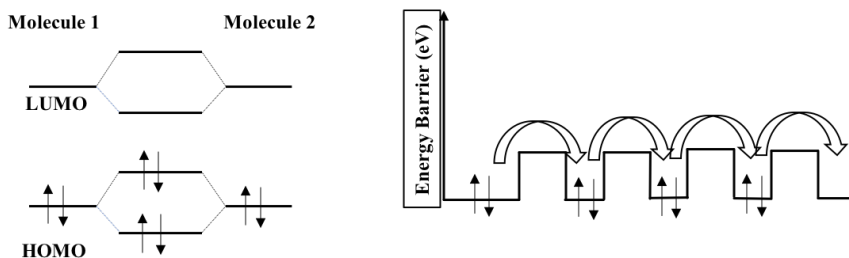


Figure 1.5. Fully delocalized band regime picture (left). Charge migration via hopping mechanism over a potential energy barrier (right)

The electronic coupling describes the electronic interactions between the electrons in different molecules. This is illustrated in Figure 1.5a for a two-level system. If two molecules are infinitely far apart, they each have their HOMO and LUMO orbitals, which have precisely the same energy. When the two molecules are brought together, both the HOMO and LUMO orbitals start mixing, leading to splitting and forming two new energy levels delocalizing over both molecules. The magnitude of the splitting between the two HOMO levels and the two LUMO levels is a measure for the electronic coupling related to holes and electrons, respectively. In this example, the initial energies of the HOMO and LUMO orbitals on the two molecules are the same. However, in a disordered material, this is generally not the case. When the energy difference is much larger than the electronic coupling, this can lead to localized states rather than delocalized electronic states. In general, the relative magnitude of the energy differences and the electronic coupling determines whether charges

are delocalized or localized. These two extreme cases are characterized by two different charge transport mechanisms, band-like transport and incoherent hopping transport, discussed below.

1.3.1. Band model

In the limit where the electronic coupling is large compared to the energetic disorder in a stack of molecules, delocalized electronic states are formed. This is analogous to the two-level system illustrated in Figure 1.5a where the electronic states are delocalized over two molecules, resulting in splitting the energy levels by two times the electronic coupling ($2J$). An infinitely long stack of molecules forms an infinite set of delocalized electronic states, resulting in a continuous band of energy levels characterized by the bandwidth. In a simple approximation, the width of the band is four times the electronic coupling between two neighbouring molecules ($4J$).⁵⁶ In such a band-like picture, electrons move relatively freely and only weakly interact (or scatter) with the environment consisting of the nuclei and other electrons. In other words, the scattering due to static energetic disorder and interaction with lattice vibrations is very weak, leading to an average mean free path between scattering events that is very long compared to the stacking distance between the molecules. In the band model, the ease with which the electrons can travel through the materials depends on the electronic coupling and hence the bandwidth. This can be expressed in an effective mass m^* that becomes smaller as the bandwidth (and the electronic coupling) increases. In the

simplest approximation, the charge carrier mobility can be related to the effective mass, m^* and the average time between scattering events, τ , through Drude's model:

$$\mu = \frac{e\tau}{m^*} \quad (1.2)$$

The scattering time depends on the thermal vibrations in the system. At high temperatures, there is a lot of thermal motion in the materials, leading to disorder and hence short times between scattering events. In contrast, the thermal disorder is minimal at very low temperatures, resulting in a long scattering time. According to equation 1.2 this leads to the specific experimental signature of band-like transport, a thermally deactivated mobility.

In organic materials, such behaviour is only observed in ultrapure highly ordered molecular crystals,²⁷ mostly at low temperatures. Although it is uncommon for π -stacked semiconductors at room temperature due to the relatively small electronic coupling between neighbouring molecules and the considerable disorder, recent reports of exceptionally high mobilities of 35 cm²/Vs (holes pentacene)⁵⁷, and 170 cm²/Vs (for 2,7-didodecyl[1]benzothieno[3,2-*b*][1]-benzothiophene (BTBT))⁵⁵ have led to the discussion of the possibility of band transport in highly pure and ordered organic semiconductors.

1.3.2. Hopping model

While there are examples of highly ordered crystalline

organic semiconductors, in many cases, they are usually disordered to some extent due to the weak intermolecular interactions between them. This is particularly important for LC materials in the mesophases that, by definition, exhibit more disorder than crystalline materials. The relatively small electronic coupling between the neighbouring molecules leads to localized electronic states that are weakly coupled to the neighbouring states. Localization of charges is enhanced by deformation of the lattice by the presence of a charge, resulting in polaron formation. In such systems with localized charges, charge transport is still possible but occurs by thermally activated hopping (Figure 1.5.b). In such a hopping mechanism, the thermal energy in the environment, in the form of (phonon) vibrations is necessary to move through the disordered energy landscape. Each hopping step can be seen as an electron transfer step that can be described by the Marcus equation:^{58,59}

$$\omega = \sqrt{\frac{\pi}{\hbar\lambda k_B T}} J^2 \exp\left(\frac{-(\Delta G^0 + \lambda)}{4\lambda k_B T}\right) \quad (1.3)$$

The charge transfer rate, ω , depends on the electronic coupling, J , the driving force or energy difference, ΔG^0 and the reorganization energy, λ . In this equation, \hbar is Planck's constant, k_B is Boltzmann's constant and T the temperature. In equation 1.3, the static energetic disorder is reflected in ΔG^0 . The possibility for polaron formation (lattice deformation) is accounted for through λ .

As the Marcus equation defines, the electron transfer rate

relates to the rate of transfer or hopping rate between only two molecules in the solid. However, in a large system, transport has to occur by sequential hopping from site to site, leading to an incoherent thermally activated hopping mechanism.⁶⁰ The Boltzmann term is essential since it defines the thermally activated nature of the transport. Opposite to band-like transport, the rate and the charge carrier mobility increase with increasing temperature.

The three parameters in the Marcus equation directly depend on the molecular structure and the interaction between neighbouring molecules along the π -stack. The reorganization energy is related to the geometry when a molecule goes from its neutral to its charged state. Photoelectron spectroscopy and density functional theory (DFT) studies reveal that large, rigid conjugated macrocycles such as pentacene, fullerenes, phthalocyanines and discotic liquid crystals exhibit the smallest reorganization energy values among their kinds of organic molecules.⁶¹

In the case of rod-like liquid crystals, the reorganization energies for BTBT isomers are around 0.2 eV,⁵⁵ while for disc-like hexa-peri-hexabenzocoronene (HBC) core, it is 0.1 eV.⁵⁹ The reorganization energy depends only on the molecular structure itself and is not sensitive to the positional/orientational order of neighbouring molecules.⁶² In contrast, positional and rotational orientations of neighbouring molecules have a significant effect on charge transfer integral (J), which describes the probability of an electron tunnelling between neighbouring molecules in self-assembled stacks. J decreases exponentially with the

intermolecular separation. For example, $J \sim \exp(-2.2z/\text{\AA})$ ⁵⁹ where z is ca. 3.5 Å for HBC molecules.

Additionally, the charge transfer integral depends on the tilt angle between neighbouring molecules in a stack. The maximum value is generally found for a fully face-to-face arrangement, and rotations between neighbouring molecules reduce its value.⁶³ This offers a particularly interesting handle to tune the charge transport properties of discotic materials since the packing geometry can be influenced directly by changes in the molecular structure. Chapter 2 discusses this in more detail, and theoretical exploration of approaches to optimize the charge transfer integral between neighbouring molecules is presented.

1.3.3. Conductivity and mobility detection techniques

Unravelling the mechanism of charge transport in a particular material typically involves measurements of the conductivity of materials as a function of temperature. In this way, it is possible to distinguish between band-like and thermally activated hopping transport. Over the last decades, various detection techniques have been developed to measure the conductivity and derive the charge carrier mobility.⁶⁴ Most of these techniques use a constant electric field (Direct Current, DC technique) which requires contact with electrodes. Alternatively, some techniques, such as microwaves or terahertz radiation, use a high-frequency oscillating electric field (Alternating Current, AC technique). The latter techniques have the advantage of being

contactless and do not require constructing a device with electrodes.

It should be noted that mobility values obtained from the different detection techniques can not always be directly compared. In DC techniques, charge transport is probed over distance typically 100 nm or more, while in high-frequency AC techniques, charge transport is probed on a much shorter distance scale. In addition, complications due to charge injection and field-dependent mobilities can hamper comparing values obtained from different techniques. The basic principles of some of the most used detection techniques for liquid crystalline materials are briefly described in the following.

1.3.3.1. Four-Contact Probe Method

One of the most straightforward DC techniques to measure conductivity is the four-contact-probe method⁶⁵, where the current-voltage relation between two contacts is used to determine conductivity (σ) at a known distance (d), as shown in the equation (4):

$$\sigma = \frac{I}{2\pi Vd} \quad (1.4)$$

I is current, and V is the measured voltage in this equation. In this method, the current is passed between two contacts and voltage change across two intermediate points is measured using a

high impedance voltmeter. Four probes with an equivalent distance (d) are aligned on semiconductor material, of which the thickness is much larger (mm) than d . Disadvantages of this method include the need to establish ohmic contacts, which requires an excellent sample homogeneity. However, the method is very sensitive and suitable to measure very low conductance values.

1.3.3.2. Time-of-Flight (TOF)

TOF is a widely used DC measurement technique to obtain charge carrier mobilities for organic materials. In this time-resolved technique, an organic layer of several microns thickness ($\sim 5\text{-}30\ \mu\text{m}$) is sandwiched between two electrodes, of which one is transparent. A short laser pulse irradiates the material through the transparent electrode to generate charge carriers. Due to the small penetration depth of incident laser light, charge carriers are generated only in a thin layer close to the electrode. Depending on the polarity of applied bias and electric DC field (in the range of $10^4 - 10^6\ \text{V/cm}$)⁶⁶, the photogenerated charge carriers (holes or electrons) migrate through the material towards the counter electrode. The collective motion of the charges in the applied electric field towards the second electrode results in a current recorded in the external circuit, using a current amplifier and storage oscilloscope, as schematically drawn in Figure 1.6.a. The current induced by the photogeneration of charges stays more or less constant until it decays to zero when the sheet of charges reaches the counter electrode (Figure 1.6.b). This time is defined as

time-of-flight or transit time, t_{tr} of the charges. A well-defined transit time is typically obtained in the case of ordered materials. In contrast, in disordered systems, the sheet of charges broadens significantly (dispersive transport), leading to a distribution of t_{tr} values across the material.⁶⁶ The mobility of holes and electrons can be obtained separately from the measured transit time, the known thickness of the sample (L) and the applied voltage (V):

$$\mu_{TOF} = \frac{L^2}{Vt_{tr}} \quad (1.5)$$

An interesting aspect of the TOF technique is that the charge carrier mobility can be obtained directly without requiring any knowledge of the concentration of charge carriers. The TOF technique is a DC technique, which means that transport is probed over a macroscopic distance. This means that a single uniform domain of the material must be formed between the electrodes for a reliable measurement of the intrinsic charge carrier mobility. For mesomorphic triphenylenes⁶⁷ successful TOF mobility measurements have been performed. However, no reliable TOF mobilities have been published for other DLCs with larger cores, such as phthalocyanines and HBCs.

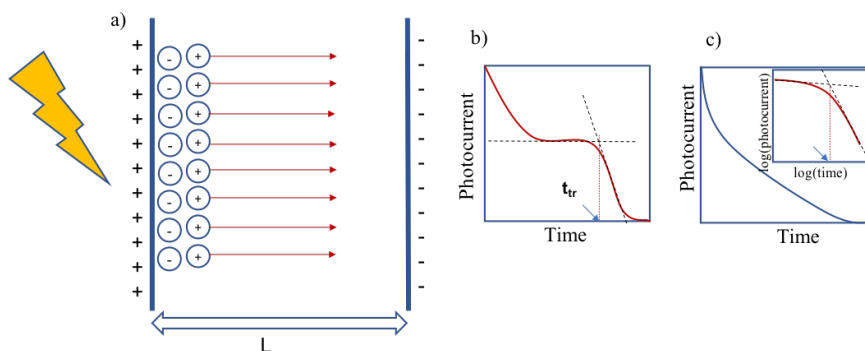


Figure 1.6. Principles of the Time of Flight (TOF) conductivity measurements a) schematic view of charge carrier generation and transport, transient photocurrent signal in b) non-dispersive transport c) dispersive transport

1.3.3.3. Space-Charge Limited Current (SCLC) “Diode Configuration”

For materials with a low concentration of charge carriers. Space-Charge Limited Current (SCLC) measurements are widely used in organic semiconductors.⁶⁸ The measurement setup used in the SCLC technique is called the ‘Diode Configuration’ since mobility values are obtained from the electrical characteristics of a diode where the organic layer is sandwiched between two electrodes. The metal electrode can be considered injecting contact; either electrons or holes can diffuse into the material at low voltage. The choice of electrodes is crucial since the Fermi level of the metal electrode needs to be close enough to the allowed levels of the studied material. Holes can be injected using high work function

metals, while low work function metals can be used to inject electrons. In the absence of traps in the material, the current density-voltage characteristics become quadratic ($J \sim V^2$). At high voltages, in the presence of charge carrier traps, the J - V characteristics become space-charge-limited, meaning that the current is limited by the injection of charge carriers from the electrode.⁶⁹ The space-charge-limited current, J , is given in equation (1.6), which is known as the Mott-Gurney equation⁷⁰:

$$J = \frac{9}{8} \varepsilon \mu_{SCLC} \frac{V^2}{d^3} \theta \quad (1.6)$$

In this equation, ε is permittivity, d is the thickness of the sample, and θ is the ratio of the number of free charges to the total number of charge carriers. θ is only considered in the presence of charge carrier traps, and it becomes 1 when the current is trap-free. In the SCLC technique, the number of injected charges reaches a certain maximum value because their electrostatic potential prevents the injection of additional charges at a low electric field.⁶⁶

Although the SCLC technique allows measuring the macroscopic mobility, it requires highly pure, trap-free samples. In the presence of traps, the J - V curves in SCLC measurements become more complex with extended intermediate regions arising from Gaussian-shaped charge carrier trap distributions.⁷¹

1.3.3.4. Organic Field-Effect Transistors (OFET)

The last DC technique considered here to obtain charge carrier mobilities for organic materials is the measurement of organic field-effect transistor (OFET) characteristics to determine the drift charge carrier mobility per unit electric field using the appropriate current-voltage (I - V) relationship. As schematically drawn in Figure 1.7. The organic semiconductor layer is deposited between the source and drain electrodes. The charge carriers are injected into the active material from a source electrode by applying positive or negative bias voltage on the gate electrode. The transport takes place between the source and the drain electrodes, while the voltage on the gate determines the charge density in the transport channel.⁷² I - V curves characteristics in OFET devices can be considered in two regimes⁶⁶:

In the linear regime where the current increases linearly with the voltage:

$$I_{SD} = \frac{W}{L} \mu_{FET} C (V_G - V_T) V_{SD} \quad (1.7)$$

and in the saturation regime:

$$I_{SD} = \frac{W}{2L} \mu_{FET} C (V_G - V_T)^2 \quad (1.8)$$

In these equations, I_{SD} and V_{SD} are current and voltage bias between source and drain electrodes, V_G is gate voltage, V_T is threshold voltage (at which the current starts increasing), C is the

capacitance of gate dielectric, $\frac{W}{L}$ is the width/length ratio of conducting channel, and μ is the charge-carrier mobility. For low source-drain voltages, the linear regime (equation 1.7) is observed where the current increases linearly, followed by the saturation regime for high voltages (equation 1.8) where the current saturates with increasing source-gate voltages, i.e. the current is independent of the source-drain voltage. Mobilities in the saturation regime are generally higher than in the linear regime due to different electric-field distributions.⁷³ FET mobilities in organic semiconductors are usually dependent on the gate voltage due to the presence of traps (structural defects and impurities).⁷⁴ This is directly related to the charge density: at a low gate voltage, not enough charges are present to fill up all traps and the transport is through these traps. At higher voltages, the charge density is high enough to fill all traps and the transport is dominated by the non-trapped charges, resulting in higher field-effect mobility.⁷⁵ Charge carrier transport is also affected by the surface topology and dielectric constant of the gate dielectric since charge transport takes place in a thin layer close to the gate electrode. Polaronic dressing of charge carriers is improved by increasing dielectric constant of gate insulator and as a consequence of enhanced polarization at the dielectric surface, the mobility is reduced.^{76,77}

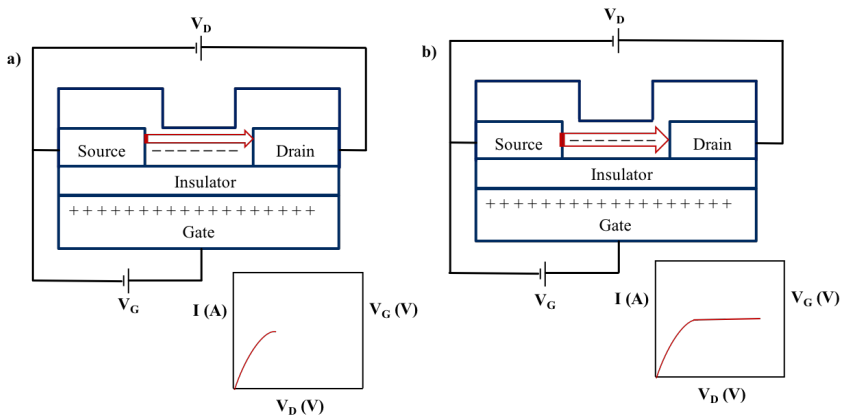


Figure 1.7. Schematic presentation of Organic Field-Effect Transistors (OFETs) operation principle during voltage application and current-voltage (I-V) relationship a) the linear regime, reaching the saturation regime b) linear and saturation regime

In the OFET technique hole and electron mobilities can be obtained separately by applying different source-drain biases and gate ($V_g < 0$, $V_d < 0$ for hole and $0 > V_g$, $0 > V_d$ for electrons). In OFET measurements based on p-type liquid crystalline molecules charge carrier mobility values up to $10^{-3} \text{ cm}^2/\text{Vs}$ for discotic liquid crystalline HBC⁷⁸ and $3 \text{ cm}^2/\text{Vs}$ for calamitic liquid crystalline BTBT⁷⁹ have been reported. A mobility as high as $0.72 \text{ cm}^2/\text{Vs}$ has been found for the n-type liquid crystalline perylene-diimide (PDI) by OFET measurements.⁸⁰ In general, understanding the temperature dependence of the charge carrier mobility and comparison of charge carrier transport with the OFET and other techniques is challenging since the measured characteristics can

depend strongly on the dielectric material, structural defects, surface topology, and geometrical structure of the device.

1.3.3.5. Pulse-Radiolysis Time-Resolved Microwave Conductivity (PR-TRMC)

In this thesis, the key approach to measure charge carrier mobilities in liquid crystalline materials is the pulse-radiolysis time-resolved microwave conductivity (PR-TRMC) technique. In contrast to the above-explained DC techniques, this AC technique uses high-frequency microwaves to probe the charge transport and requires no contact electrodes and no elaborated sample preparation. The charge carrier mobility values obtained in this way are free from domain boundary effects and space-charge effects due to the fast reversal time of microwave field in a few tens of picoseconds and the low concentrations of charges present. PR-TRMC has been applied to (bulk) solid-state as well as liquids and single polymer chains in solution. The fact that conductivity measurements can be performed in the liquid state is of particular interest for this thesis since it allows to measure the charge mobility in all mesophases, even the isotropic liquid phase. Reported mobilities from PR-TRMC measurements are often higher than those obtained by DC techniques discussed above. The mobility obtained from the PR-TRMC technique can, in many cases, be considered as the maximum attainable mobility values in defect-free samples.^{81,62,50,82-84}

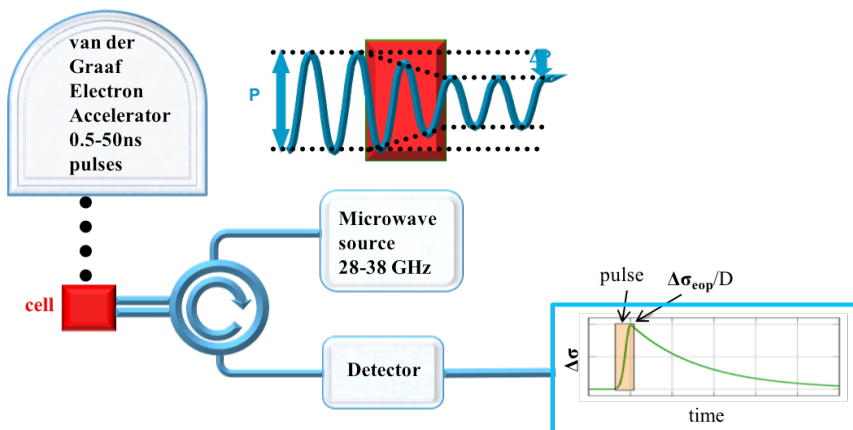


Figure 1.8. Schematic representation of Time-Resolved Microwave Conductivity (PR-TRMC) technique.

A schematic representation of the setup is shown in Figure 1.8. The sample in the PR-TRMC measurements is prepared by compressing the solid-state material into a microwave cell by hand using a close-fitting rectangular Teflon rod. The sample can either fill the cell entirely or a much smaller amount can be placed in a small polyimide sample holder that fills the total volume of the microwave waveguide. To correct the fact that the sample volume is not completely filled with material, the conductivity data is corrected by a fill factor (F), which is usually around 0.6-0.8. Charges are generated in the sample by irradiation with short pulses (from 0.5 to 50 ns) of 3 MeV electrons from a Van de Graaff accelerator. The penetration depth of 3 MeV electrons in materials of density 1 g/cm^3 (assuming the density of a material is close to 1 g/cm^3 as usual for organic materials)⁸⁵ is ca. 15 mm, which is much larger than the sample thickness of 3.5 mm.¹² Therefore, pulsed

irradiations lead to a uniform ionization within the sample with a concentration that is known from dosimetry measurements. Typically a micromolar concentration of charges is present.

In order to probe the motion of the charges, a Gunn-diode oscillator is used to generate continuous microwaves with frequencies ranging from 26.5 GHz to 38 GHz. For non-conducting materials, microwaves travel through the sample without any absorption or loss. However, if mobile charge carriers are present in the sample this leads to absorption of part of the microwave power because the oscillating electric field perturbs the motion of the charges. The fractional change in the microwave power, $(\frac{\Delta P}{P})$, absorbed by the sample is directly proportional to the change in the conductivity ($\Delta\sigma$) of the sample with a fraction of cell volume occupied by the sample (F) and the sensitivity parameter (A):

$$\frac{\Delta P}{P} = AF\Delta\sigma \quad (1.9)$$

The value of A is determined by the dimensions of the microwave cell and the dielectric properties of the sample. The conductivity obtained from these measurements can derive a charge carrier mobility if the concentration of charge generated during the pulse is known. Since we know the amount of energy deposited per unit volume from radiation dosimetry measurements, we can estimate the concentration of charges at the end of the pulse. Notably, both positive and negative charges are created by

irradiation and hence the change in conductivity is the sum of the positive and negative carrier mobilities, $\sum \mu = \mu_+ + \mu_-$

$$\sum \mu = E_p [\Delta\sigma/D]_{eop} \quad (1.10)$$

With the known energy deposition (dose, D , J/m^3), the conductivity change at the end of the pulse (eop) and the calculated average pair-formation energy (E_p , eV), the mobility of the charges can be calculated according to equation (10).⁸⁶ The measurement cell is contained in a cryostat in which the temperature can be varied from -100 to $+200$ °C. This allows for mobility measurements in the different mesophases of thermotropic liquid crystalline molecules.¹² PR-TRMC measurements have been used for various liquid crystalline molecules described later in this thesis.

1.3.3.6. Field-Induced Time-Resolved Microwave Conductivity (FI-TRMC)

Contactless TRMC methods, such as pulse-radiolysis (PR-) and flash-photolysis (FP-), serve fast and accurate measurements to achieve charge carrier mobility and carrier lifetime properties of various types of samples morphologies, including crystals⁸⁷, powders⁸⁸, thin films⁸⁹, suspensions and fluids. However, charge carriers are generated throughout the bulk of the material in these methods. However, the interfaces play an important role, especially in the applications of organic photovoltaics from both structural

and functional points of view. Material/substrate and material/air interface interactions cause molecules to adopt different orientations than their bulk state. Additionally, p- and n-type semiconductor interactions strongly influence photovoltaic response.⁹⁰

In order to understand the interfacial charge carrier mobility, Shu Seki and his team have developed a novel system referred to as field-induced time-resolved microwave conductivity (FI-TRMC).⁹¹ In this technique, a metal-insulator-semiconductor (MIS) device is initially prepared to adopt an Au/SiO₂/PMMA/semiconductor/Au configuration and set into a microwave cavity. Although the metal electrodes decrease the effective power of the reflected microwave (~9 GHz), a selectively applied gate bias enables monitoring the time dependence of both dielectric loss and injected charge carrier amounts at the interface. This method makes a direct quantification of the charge carrier concentration possible. Holes and electrons can be directly injected by the microsecond-pulse bias voltage, and field-induced charge carrier generation can be obtained at the interface of insulator PMMA and spin-coated semiconductor.

As in PR-TRMC, the generated charge carriers absorb part of the incident microwave power, resulting in a change in the power of the reflected microwaves, ΔP . As shown in the equation of 1.11, the change in the conductivity, $\Delta\sigma$, is directly proportional to the relative change in the reflected microwave power, $\frac{\Delta P_r}{P_r}$. The relation between the change in the value of the electrical conductivity generated by the applied gate bias and the change in the number of

charge carriers, ΔN , is shown in equation 1.12. The change in the number of charge carriers, ΔN , is accumulated in the MIS device due to the gate bias voltage. Here, K is an experimental proportionality factor that depends of the geometry of the sample and the characteristics of the microwave cavity used, while μ denotes the charge carrier mobility.⁹²

$$\Delta\sigma = K \frac{\Delta P_r}{P_r} \quad (1.11)$$

$$\Delta\sigma = e\mu\Delta N \quad (1.12)$$

From FI-TRMC measurements, PDI-based liquid crystalline molecules with alkyl and fluoroalkyl tails showed 0.2 and 0.3 cm^2/Vs hole and electron mobilities, respectively.⁹³ In contrast, PDI molecules with triethylene glycol and semifluoroalkyl tails showed no notable conductivity, highlighting the importance of side-chain structure on the charge transport properties. Derivatives of naphthalenedicarboximides (NDIs) showed higher electron mobilities up to 12-15 cm^2/Vs at room temperature compared to PDIs.⁹⁴ Recently, a strikingly high interfacial mobility of 170 cm^2/Vs was measured for benzothienezobenzothiophene (BTBT) derivatives at room temperature.⁹⁵ The further details of this record charge carrier mobility results measured by FI-TRMC are discussed in Chapter 4 of this thesis.

1.4. Aim and Outline of This Thesis

The aim of the research outlined in this thesis is to increase the

understanding of the relation between supramolecular order and the resulting optoelectronic properties in organic semiconductor materials, with a specific focus on liquid crystalline ones.

In **Chapter 2**, we describe the synthesis of two novel peripherally substituted discotic liquid crystalline hexa-*peri*-hexabenzocoronene (HBC) compounds and systematically study the influence of substitution position (*meta*- vs *para*-) on the aggregation properties in solution. Detailed temperature-, concentration-, and solvent- dependent study results demonstrate that the position of the substituent (*meta*- vs *para*-) has a pronounced effect on the aggregation and *para*-position substituted HBC has higher tendency to aggregate.

In **Chapter 3**, we focus the relationship between supramolecular organization and molecular design of such tailored HBC derivatives in the solid state. By performing temperature-dependent charge transport measurements, we also gain insight into the charge transport of the different mesophases in these HBC isomers. Preliminary studies show that changes in the preparation procedures and recrystallization of HBC derivatives can improve the columnar order of *meta*-position substituted HBC.

In **Chapter 4**, we examine the charge transport mechanism and intrinsic charge carrier mobility in rod-like liquid crystalline [1]benzothieno[3,2-b][1]benzothiophene (BTBT) derivatives with varying side chain length in the solid state. The temperature dependence of the charge carrier mobility and decay kinetics of C_n -BTBT- C_n ($n= 8, 10, 12$) were investigated by PR-TRMC measurements. We report remarkably high intrinsic charge carrier

mobilities following a thermally activated hopping model as the primary mechanism for charge transport for the investigated BTBT derivatives.

In **Chapter 5**, we study a series of polyamide materials that contain repeating units of conjugated semiconducting bithiophene or dicyanoperylene bisimide, with varying aliphatic spacer lengths. PR-TRMC results for these compounds show that the length of the aliphatic spacer length does not significantly affect the intracolumnar charge transport in such polyamide derivatives. The polymer backbone offers sufficient freedom for the conjugated units to be organized in a stacked fashion, as evident from the optical properties.

1.5. References

1. Tang, C. W. Two-layer organic photovoltaic cell. *Applied Physics Letters* **48**, 183–185 (1986).
2. Burroughes, J. H., Jones, C. A. & Friend, R. H. New semiconductor device physics in polymer diodes and transistors. *Nature* **335**, 137–141 (1988).
3. Tsumura, A., Koezuka, H. & Ando, T. Macromolecular electronic device: Field-effect transistor with a polythiophene thin film. *Applied Physics Letters* **49**, 1210–1212 (1986).
4. Mohammad Bagher, A. Comparison of Organic Solar Cells and Inorganic Solar Cells. *International Journal of Renewable and Sustainable Energy* **3**, 53 (2014).
5. Meng, L. *et al.* Organic and solution-processed tandem solar cells with 17.3% efficiency. *Science* **361**, 1094–1098 (2018).
6. Green, M. A. *et al.* Solar cell efficiency tables (version 54). *Progress in Photovoltaics: Research and Applications* **27**, 565–575 (2019).
7. Pisula, W., Feng, X. & Müllen, K. Charge-Carrier Transporting Graphene-Type Molecules †. *Chemistry of Materials* **23**, 554–567 (2011).
8. Schweicher, G., Olivier, Y., Lemaire, V. & Geerts, Y. H. What currently limits charge carrier mobility in crystals of molecular semiconductors? *Israel Journal of Chemistry* **54**, 595–620 (2014).

9. Umansky, V. *et al.* MBE growth of ultra-low disorder 2DEG with mobility exceeding $35 \times 10^6 \text{cm}^2/\text{Vs}$. *Journal of Crystal Growth* **311**, 1658–1661 (2009).
10. Chen, X. Y., Shen, W. Z. & He, Y. L. Enhancement of electron mobility in nanocrystalline silicon/crystalline silicon heterostructures. *Journal of Applied Physics* **97**, 024305 (2005).
11. Herz, L. M. Charge-Carrier Mobilities in Metal Halide Perovskites: Fundamental Mechanisms and Limits. *ACS Energy Letters* **2**, 1539–1548 (2017).
12. Warman, J. M. & Van De Craats, A. M. Charge Mobility in Discotic Materials Studied by Pr-Trmc. *Molecular Crystals and Liquid Crystals* **396**, 41–72 (2003).
13. Mas-Torrent, M. & Rovira, C. Role of Molecular Order and Solid-State Structure in Organic Field-Effect Transistors. *Chemical Reviews* **111**, 4833–4856 (2011).
14. Wang, C., Dong, H., Hu, W., Liu, Y. & Zhu, D. Semiconducting π -Conjugated Systems in Field-Effect Transistors: A Material Odyssey of Organic Electronics. *Chemical Reviews* **112**, 2208–2267 (2012).
15. Schweicher, G., Olivier, Y., Lemaire, V. & Geerts, Y. H. What Currently Limits Charge Carrier Mobility in Crystals of Molecular Semiconductors? *Israel Journal of Chemistry* **54**, 595–620 (2014).
16. Craats, A. M. van de *et al.* Record Charge Carrier Mobility in a Room-Temperature Discotic Liquid-Crystalline

- Derivative of Hexabenzocoronene. *Advanced Materials* **11**, 1469–1472 (1999).
17. Hanna, J., Ohno, A. & Iino, H. Charge carrier transport in liquid crystals. *Thin Solid Films* **554**, 58–63 (2014).
 18. Bushby, R. J. & Lozman, O. R. Photoconducting liquid crystals. *Current Opinion in Solid State and Materials Science* **6**, 569–578 (2002).
 19. Schmidt-Mende, L. *et al.* Self-organized discotic liquid crystals for high-efficiency organic photovoltaics. *Science* **293**, 1119–1122 (2001).
 20. Reinitzer, F. Beiträge zur Kenntniss des Cholesterins. *Monatshefte für Chemie - Chemical Monthly* **9**, 421–441 (1888).
 21. Mitov, M. Liquid-crystal science from 1888 to 1922: Building a revolution. *ChemPhysChem* **15**, 1245–1250 (2014).
 22. Hill, J. P., Shrestha, L. K., Ishihara, S., Ji, Q. & Ariga, K. Self-Assembly: From amphiphiles to chromophores and beyond. *Molecules* **19**, 8589–8609 (2014).
 23. Hoeben, F. J. M., Jonkheijm, P., Meijer, E. W. & Schenning, A. P. H. J. About supramolecular assemblies of π -conjugated systems. *Chemical Reviews* **105**, 1491–1546 (2005).
 24. Steed, J. W., Turner, D. R. & Wallace, K. *Core Concepts in Supramolecular Chemistry and Nanochemistry: From Supramolecules to Nanotechnology*. (John Wiley, 2007).

25. Funahashi, M. & Hanna, J. Fast Hole Transport in a New Calamitic Liquid Crystal of 2-(4'-Heptyloxyphenyl)-6-Dodecylthiobenzothiazole. *Physical Review Letters* **78**, 2184–2187 (1997).
26. Kajitani, T., Kohmoto, S., Yamamoto, M. & Kishikawa, K. Generation of Stable Calamitic Liquid-Crystal Phases with Lateral Intermolecular Hydrogen Bonding. *Chemistry of Materials* **16**, 2329–2331 (2004).
27. Kobayashi, H. *et al.* Hopping and band mobilities of pentacene, rubrene, and 2,7-dioctyl[1]benzothieno[3,2-b][1]benzothiophene (C₈-BTBT) from first principle calculations. *The Journal of Chemical Physics* **139**, 014707 (2013).
28. Takimiya, K., Shinamura, S., Osaka, I. & Miyazaki, E. Thienoacene-Based Organic Semiconductors. *Advanced Materials* **23**, 4347–4370 (2011).
29. Zhong, T., Mandle, R., Saez, I., Cowling, S. & Goodby, J. Rods to discs in the study of mesomorphism in discotic liquid crystals. *Liquid Crystals* **45**, 2274–2293 (2018).
30. Andrienko, D. Introduction to liquid crystals. *Journal of Molecular Liquids* **267**, 520–541 (2018).
31. Chandrasekhar, S., Sadashiva, B. K. & Suresh, K. A. Liquid crystals of disc-like molecules. *Pramana* **9**, 471–480 (1977).
32. Stals, P. J. M. *et al.* Dynamic Supramolecular Polymers Based on Benzene-1,3,5-tricarboxamides: The Influence of Amide Connectivity on Aggregate Stability and

- Amplification of Chirality. *Chemistry - A European Journal* **16**, 810–821 (2010).
33. Kumar, S., Bera, S., Nandi, S. K. & Haldar, D. The effect of amide bond orientation and symmetry on the self-assembly and gelation of discotic tripeptides. *Soft Matter* **17**, 113–119 (2021).
 34. Miao, J. & Zhu, L. Hydrogen Bond-Assisted Supramolecular Self-Assembly of Doubly Discotic Supermolecules Based on Porphyrin and Triphenylene. *Chemistry of Materials* **22**, 197–206 (2010).
 35. Gearba, R. I. *et al.* Tailoring Discotic Mesophases: Columnar Order Enforced with Hydrogen Bonds. *Advanced Materials* **15**, 1614–1618 (2003).
 36. Paraschiv, I. *et al.* H-Bond-Stabilized Triphenylene-Based Columnar Discotic Liquid Crystals. *Chemistry of Materials* **18**, 968–974 (2006).
 37. Velpula, G. *et al.* Hydrogen-Bonded Donor–Acceptor Arrays at the Solution–Graphite Interface. *Chemistry - A European Journal* **24**, 12071–12077 (2018).
 38. van de Craats, A. M. *et al.* Charge transport in mesomorphic derivatives of perylene. *Synthetic Metals* **102**, 1550–1551 (1999).
 39. Ward, M. D. & Pivovarov, A. M. Crystalline Lattices, Self-assembly of. in *Encyclopedia of Materials: Science and Technology* 1903–1908 (Elsevier, 2001). doi:10.1016/B0-08-043152-6/00346-6.

40. Kaafarani, B. R. Discotic Liquid Crystals for Opto-Electronic Applications † ‡. *Chemistry of Materials* **23**, 378–396 (2011).
41. Dąbrowski, R., Kula, P. & Herman, J. High Birefringence Liquid Crystals. *Crystals* **3**, 443–482 (2013).
42. Nesrullajev, A. Thermotropic, refracting and thermo-optical properties in three homologs of 4-n-alkyl-4'-cyanobiphenyls. *Lithuanian Journal of Physics* **55**, 24–34 (2015).
43. Kumar, S. Liquid Crystals :Experimental Study of Physical Properties and Phase Transitions. *Molecules* **6**, 1055–1056 (2001).
44. Schmidt-Mende, L. Self-Organized Discotic Liquid Crystals for High-Efficiency Organic Photovoltaics. *Science* **293**, 1119–1122 (2001).
45. Chen, H.-W., Lee, J.-H., Lin, B.-Y., Chen, S. & Wu, S.-T. Liquid crystal display and organic light-emitting diode display: present status and future perspectives. *Light: Science & Applications* **7**, 17168–17168 (2018).
46. Iino, H., Usui, T. & Hanna, J. Liquid crystals for organic thin-film transistors. *Nature Communications* **6**, 6828 (2015).
47. Taherian, R. The Theory of Electrical Conductivity. in *Electrical Conductivity in Polymer-Based Composites: Experiments, Modelling and Applications* 1–18 (Elsevier, 2019). doi:10.1016/B978-0-12-812541-0.00001-X.

48. Seki, S., Saeki, A., Sakurai, T. & Sakamaki, D. Charge carrier mobility in organic molecular materials probed by electromagnetic waves. *Phys. Chem. Chem. Phys.* **16**, 11093–11113 (2014).
49. Bengs, H. *et al.* Highly photoconductive discotic liquid crystals Structure–property relations in the homologous series of hexa-alkoxytriphenylenes. *Liquid Crystals* **15**, 565–574 (1993).
50. van de Craats, A. M. *et al.* The mobility of charge carriers in all four phases of the columnar discotic material hexakis(hexylthio)triphenylene: Combined TOF and PR-TRMC results. *Advanced Materials* **8**, 823–826 (1996).
51. Pisula, W. *et al.* Relation between Supramolecular Order and Charge Carrier Mobility of Branched Alkyl Hexa- p eri -hexabenzocoronenes. *Chemistry of Materials* **18**, 3634–3640 (2006).
52. Jurchescu, O. D., Popinciuc, M., van Wees, B. J. & Palstra, T. T. M. Interface-Controlled, High-Mobility Organic Transistors. *Advanced Materials* **19**, 688–692 (2007).
53. Takeya, J. *et al.* Very high-mobility organic single-crystal transistors with in-crystal conduction channels. *Applied Physics Letters* **90**, 102120 (2007).
54. Minemawari, H. *et al.* Inkjet printing of single-crystal films. *Nature* **475**, 364–367 (2011).
55. Tsutsui, Y. *et al.* Charge Carrier Mobility: Unraveling Unprecedented Charge Carrier Mobility through Structure Property Relationship of Four Isomers of

- Didodecyl[1]benzothieno[3,2- b][1]benzothiophene (Adv. Mater. 33/2016). *Advanced Materials* **28**, 7291–7291 (2016).
56. Troisi, A. Charge transport in high mobility molecular semiconductors: classical models and new theories. *Chemical Society Reviews* **40**, 2347 (2011).
57. Jurchescu, O. D., Baas, J. & Palstra, T. T. M. Effect of impurities on the mobility of single crystal pentacene. *Applied Physics Letters* **84**, 3061–3063 (2004).
58. Marcus, R. A. Chemical and Electrochemical Electron-Transfer Theory. *Annual Review of Physical Chemistry* **15**, 155–196 (1964).
59. Feng, X. *et al.* Towards high charge-carrier mobilities by rational design of the shape and periphery of discotics. *Nature Materials* **8**, 421–426 (2009).
60. Shuai, Z., Wang, L. & Song, C. Hopping Mechanism. in *Springer* (ed. Gu, T.) 7–41 (Springer Netherlands, 2012). doi:10.1007/978-3-642-25076-7_2.
61. Devos, A. & Lannoo, M. Electron-phonon coupling for aromatic molecular crystals: Possible consequences for their superconductivity. *Physical Review B* **58**, 8236–8239 (1998).
62. Lemaire, V. *et al.* Charge Transport Properties in Discotic Liquid Crystals: A Quantum-Chemical Insight into Structure–Property Relationships. *Journal of the American Chemical Society* **126**, 3271–3279 (2004).

63. Dong, H., Fu, X., Liu, J., Wang, Z. & Hu, W. 25th Anniversary Article: Key Points for High-Mobility Organic Field-Effect Transistors. *Advanced Materials* **25**, 6158–6183 (2013).
64. Karl, N. Charge carrier transport in organic semiconductors. *Synthetic Metals* **133–134**, 649–657 (2003).
65. Solymar, L., Walsh, D. & R.R.A. Syms. *Electrical Properties Of Materials*. (Oxford University Press, 2014).
66. Coropceanu, V. *et al.* Charge Transport in Organic Semiconductors. *Chemical Reviews* **107**, 926–952 (2007).
67. Wegewijs, B. R. *et al.* Charge-carrier mobilities in binary mixtures of discotic triphenylene derivatives as a function of temperature. *Physical Review B* **65**, 245112 (2002).
68. Zubair, M., Ang, Y. S. & Ang, L. K. Thickness Dependence of Space-Charge-Limited Current in Spatially Disordered Organic Semiconductors. *IEEE Transactions on Electron Devices* **65**, 3421–3429 (2018).
69. Blom, P. W. M., de Jong, M. J. M. & Vleggaar, J. J. M. Electron and hole transport in poly(p-phenylene vinylene) devices. *Applied Physics Letters* **68**, 3308–3310 (1996).
70. Tiwari, S. & Greenham, N. C. Charge mobility measurement techniques in organic semiconductors. *Optical and Quantum Electronics* **41**, 69–89 (2009).
71. Bäessler, H. Charge Transport in Disordered Organic Photoconductors a Monte Carlo Simulation Study. *physica status solidi (b)* **175**, 15–56 (1993).

72. Horowitz, G. Organic Field-Effect Transistors. *Advanced Materials* **10**, 365–377 (1998).
73. Rost, C., Gundlach, D. J., Karg, S. & Rieß, W. Ambipolar organic field-effect transistor based on an organic heterostructure. *Journal of Applied Physics* **95**, 5782–5787 (2004).
74. Dimitrakopoulos, C. D. Low-Voltage Organic Transistors on Plastic Comprising High-Dielectric Constant Gate Insulators. *Science* **283**, 822–824 (1999).
75. Katz, H. E. & Bao, Z. The Physical Chemistry of Organic Field-Effect Transistors. *The Journal of Physical Chemistry B* **104**, 671–678 (2000).
76. Stassen, A. F., de Boer, R. W. I., Iosad, N. N. & Morpurgo, A. F. Influence of the gate dielectric on the mobility of rubrene single-crystal field-effect transistors. *Applied Physics Letters* **85**, 3899–3901 (2004).
77. Coropceanu, V. & Brédas, J.-L. A polarized response. *Nature Materials* **5**, 929–930 (2006).
78. Shklyarevskiy, I. O. *et al.* High Anisotropy of the Field-Effect Transistor Mobility in Magnetically Aligned Discotic Liquid-Crystalline Semiconductors. *Journal of the American Chemical Society* **127**, 16233–16237 (2005).
79. Iino, H. & Hanna, J. Availability of Liquid Crystallinity in Solution Processing for Polycrystalline Thin Films. *Advanced Materials* **23**, 1748–1751 (2011).
80. Oh, J. H., Liu, S., Bao, Z., Schmidt, R. & Würthner, F. Air-stable n-channel organic thin-film transistors with high

- field-effect mobility based on N,N'-bis(heptafluorobutyl)-3,4:9,10-perylene diimide. *Applied Physics Letters* **91**, 212107 (2007).
81. Grozema, F. C. & Siebbeles, L. D. A. Mechanism of charge transport in self-organizing organic materials. *International Reviews in Physical Chemistry* **27**, 87–138 (2008).
 82. Grozema, F. C. *et al.* The formation and recombination kinetics of positively charged poly(phenylene vinylene) chains in pulse-irradiated dilute solutions. *Journal of Physical Chemistry A* **107**, 5976–5986 (2003).
 83. Grozema, F. C. & Siebbeles, L. D. A. Charge Mobilities in Conjugated Polymers Measured by Pulse Radiolysis Time-Resolved Microwave Conductivity: From Single Chains to Solids. *The Journal of Physical Chemistry Letters* **2**, 2951–2958 (2011).
 84. Warman, J. M. *et al.* Charge Mobilities in Organic Semiconducting Materials Determined by Pulse-Radiolysis Time-Resolved Microwave Conductivity: π -Bond-Conjugated Polymers versus π - π -Stacked Discotics. *Chemistry of Materials* **16**, 4600–4609 (2004).
 85. Piris, J. Optoelectronic Properties of Discotic Materials for Device Applications. (Delft University of Technology, 2004).
 86. Warman, J. M. *et al.* Charge Mobilities in Organic Semiconducting Materials Determined by Pulse-Radiolysis Time-Resolved Microwave Conductivity: π -Bond-

- Conjugated Polymers versus π - π -Stacked Discotics. *Chemistry of Materials* **16**, 4600–4609 (2004).
87. Saeki, A., Seki, S., Takenobu, T., Iwasa, Y. & Tagawa, S. Mobility and Dynamics of Charge Carriers in Rubrene Single Crystals Studied by Flash-Photolysis Microwave Conductivity and Optical Spectroscopy. *Advanced Materials* **20**, 920–923 (2008).
88. de Haas, M. P., Warman, J. M., Anthopoulos, T. D. & de Leeuw, D. M. The Mobility and Decay Kinetics of Charge Carriers in Pulse-Ionized Microcrystalline PCBM Powder. *Advanced Functional Materials* **16**, 2274–2280 (2006).
89. Crovetto, A. *et al.* Shining Light on Sulfide Perovskites: LaYS₃ Material Properties and Solar Cells. *Chemistry of Materials* **31**, 3359–3369 (2019).
90. Chattopadhyay, S., Kokenyesi, R. S., Hong, M. J., Watts, C. L. & Labram, J. G. Resolving in-plane and out-of-plane mobility using time resolved microwave conductivity. *Journal of Materials Chemistry C* **8**, 10761–10766 (2020).
91. Honsho, Y., Miyakai, T., Sakurai, T., Saeki, A. & Seki, S. Evaluation of intrinsic charge carrier transport at insulator-semiconductor interfaces probed by a non-contact microwave-based technique. *Scientific Reports* **3**, (2013).
92. Choi, W. *et al.* Non-contact, non-destructive, quantitative probing of interfacial trap sites for charge carrier transport at semiconductor-insulator boundary. *Applied Physics Letters* **105**, (2014).

93. Sakurai, T., Tsutsui, Y., Choi, W. & Seki, S. Intrinsic charge carrier mobilities at InsulatorSemiconductor interfaces probed by microwave-based techniques: Studies with liquid crystalline organic semiconductors. *Chemistry Letters* **44**, 1401–1403 (2015).
94. Inoue, J. *et al.* Rapid Evaluation of Electron Mobilities at Semiconductor-Insulator Interfaces in an Ambient Atmosphere by a Contactless Microwave-Based Technique. *ACS Omega* **2**, 164–170 (2017).
95. Tsutsui, Y. *et al.* Unraveling Unprecedented Charge Carrier Mobility through Structure Property Relationship of Four Isomers of Didodecyl[1]benzothieno[3,2-b][1]benzothiophene. *Advanced Materials* **28**, 7106–7114 (2016).

Chapter 2

Synthesis & Optical Spectroscopy of Discotic Hexa-*peri*-hexabenzocoronene Derivatives: Self-Assembly Properties of Molecular Nanowires in Solution

Abstract

This study aims to achieve control over the self-assembly properties of two novel HBCs, MetaHBC and ParaHBC, derivatives in solution by tailoring the solubilizing side chains. By combining concentration and temperature-dependent studies, we show that the position of the substituent (meta- vs para-) has a pronounced effect on the aggregation. Broadened and non-visible chemical shifts of ParaHBC and MetaHBC in ^1H NMR spectra at room temperature indicate that both derivatives exist as fully aggregated stacks at 10^{-3} M concentration, which is higher than those of analogous HBC derivatives in literature. Compared to ParaHBC aggregates, MetaHBC at various concentrations showed more distorted supramolecular arrangement since rotational freedom of phenyl rings causes an overlap between meta-substituted side chains and correspondingly weaker π - π interaction between molecules. In all solvents considered, ParaHBC exhibits a stronger tendency to aggregate than MetaHBC. These results give insight into the effect of the side chains on the aggregation behavior of HBCs, which gives direction to possible sidechain engineering to optimize the supramolecular packing in the solid state.

2.1. Introduction

Discotic liquid crystalline (DLC) materials consist of molecules that are characterized by a rigid aromatic disc-like core surrounded by flexible side chains. These molecules tend to self-assemble in columnar stacks where the aromatic core forms a π -stacked pathway surrounded by an insulation layer of side chains.^{1,2} When the side chains are sufficiently long, the materials may form one or more liquid crystalline phases where the overall π -stacked structure is maintained but with more structural disorder along the stack. Discotic materials are of considerable interest for applications in organic electronics where the π -stack forms a one-dimensional pathway for charge transport.³ The efficiency of charge transport along this π -stack is directly linked to the organization and disorder of these materials. It is known that significant differences in charge carrier mobility occur between the different crystalline and liquid crystalline phases.⁴⁻⁶

The phase behavior and disorder in discotic materials are determined by the interaction between the aromatic cores and the interactions between the (aliphatic) side chains. The aggregation of DLC molecules can be influenced by altering the size, shape, and inclusion of hetero atoms in the aromatic core and by adding chemical functionalities (e.g. hydrogen bonding units) to the side chains.⁷

Among the class of DLC materials, hexa-*peri*-hexabenzocoronene (HBC) based DLCs have attracted a lot of attention over the past decades. Their favorable self-assembling

and electronic properties make them attractive for optoelectronic devices.^{4,8,9} HBCs consist of large aromatic cores with high thermal stability and strong π - π stacking interactions that result in highly ordered columnar stacks. This high order can lead to exceptional charge carrier mobilities as has been shown for HBC-C₁₂ which contains dodecane sidechains. For this material one of the highest 1D charge carrier mobilities for solid state DLC materials (1.1 cm²/Vs) has been obtained by pulse-radiolysis time-resolved microwave conductivity measurements (PR-TRMC).¹⁰

While the reported maximum mobilities for HBCs are high, there is still significant room for improvement if the organization of the individual molecules in the solid and liquid crystalline phases can be improved, as discussed in Chapter 1. However, achieving control over molecular self-assembly is a complicated task as it depends on an interplay between different relatively weak interactions caused by different parts of the molecules. In Chapter 2, several aspects related to the self-assembly of HBCs were discussed, including the avoidance of steric hindrance of the side chains, avoiding repulsive electrostatic interactions (quadrupole-quadrupole repulsion) and some strategies to introduce specific interactions that promote a face-to-face assembly.

In this chapter, we explore one of the approaches discussed in Chapter 2; introduction of substituents in a meta-configuration, rather than in the common para-configuration. Specifically, we study the difference in aggregation tendency in solution for the meta and para varieties. The tendency to form self-assembled aggregates in solution can give important insight into the

aggregation process that can also translate into insights into packing in the solid state. The synthesis is described of two new HBC-derivatives, **ParaHBC** and **MetaHBC**, in which rigid phenyl groups are attached to the aromatic HBC core through an acetylene spacer to allow for a planar structure, see Figure 2.1. This sets them apart from the twisted structures that are generally obtained when a phenyl is directly coupled to the HBC core. From the synthetic perspective, acetylene bridging between the HBC core and the solubilizing side chains leads to higher yields and fewer side-products due to the Hagihara-Sonogashira coupling reaction protocol. However, a tedious purification step after the palladium-catalyzed cross-coupling reaction remains.^{7,11} Dodecyloxy chains are introduced on the phenyl rings in either the *meta*- or the *para*-position. These side chains provide reasonable solubility and promote high order in the columnar due to additional hydrogen bonding.¹⁰

The aggregation behavior of these new HBC derivatives in the solution (Figure 2.1) were studied by temperature- and concentration-dependent ¹H-NMR, UV/vis and photoluminescence spectroscopy studies in 1,1,2,2-tetrachloroethane-d₂ NMR solvent. In addition, the effect of solvent on HBC aggregation is investigated in various common organic solvents to identify good and bad solvents for the assembly and deposition of HBCs.

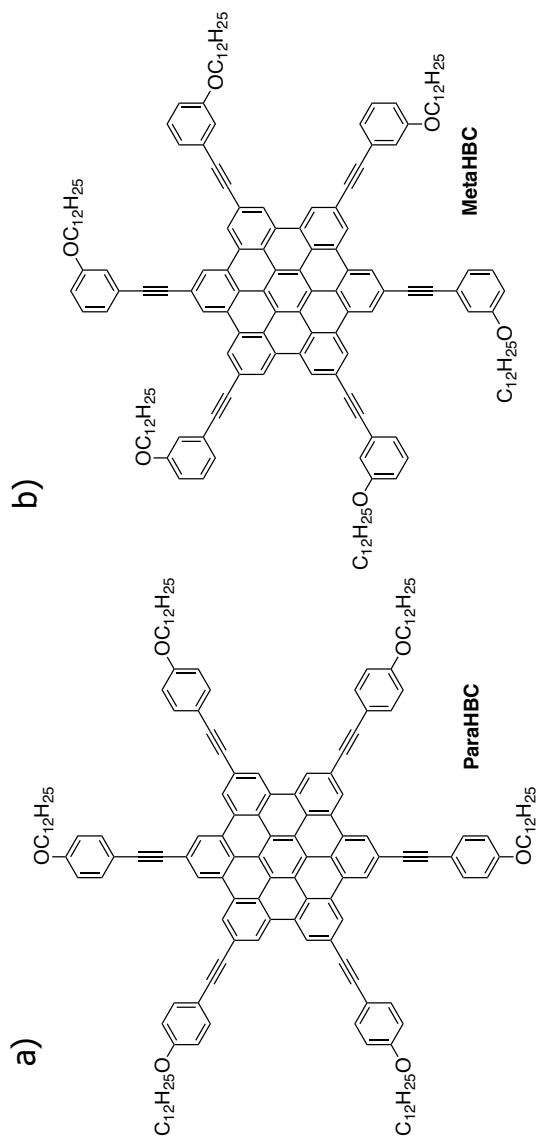


Figure 2.1. Molecular structures of HBC derivatives with solubilizing side chains attached to a) para- position, ParaHBC b) meta- position, MetaHBC

2.2. Results

In this section, we describe the synthesis of two new HBC derivatives that vary in substituent positions. Subsequently, the study of aggregation of these compounds is described using NMR spectroscopy and optical absorption/emission spectroscopy as a function of temperature and concentration. Finally, the effect of solvent on aggregation is discussed.

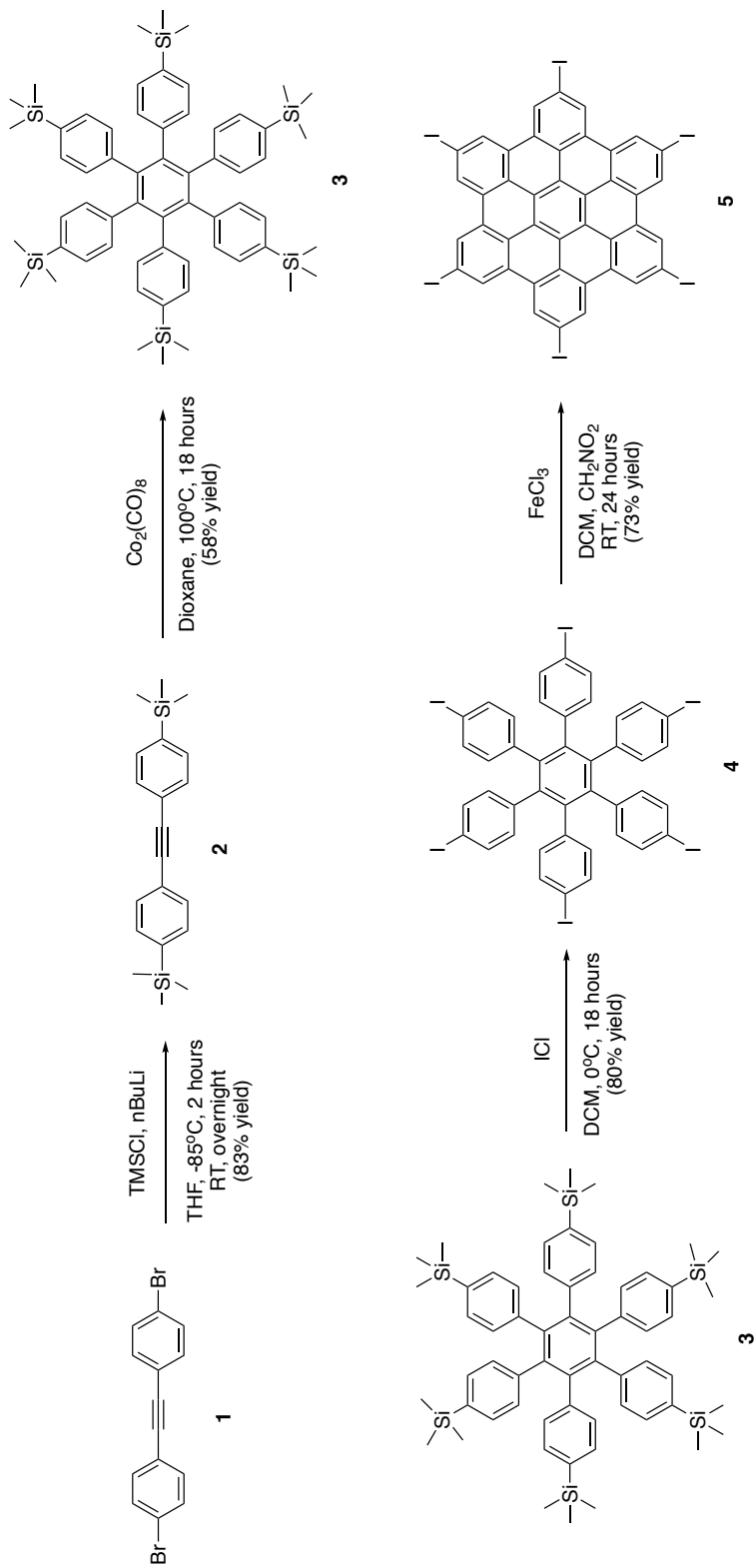
2.2.1. Synthetic Strategy

It is known that π -conjugated molecules with compatible substitutions tend to aggregate strongly in solution, leading to significant complications in the purification steps. We have synthesized and purified the HBC core and the solubilizing side chains individually and obtained **ParaHBC** and **MetaHBC** as the final compounds to minimize this problem. In the first step, insoluble but highly reactive hexaiodo-*peri*-hexabenzocoronene (**5**) was synthesized through a four-step procedure outlined in Scheme 3.1. Starting from commercially available 1,2-bis(4-bromophenyl)ethyne (**1**), the highly soluble compound (**3**) was prepared by a $\text{Co}_2(\text{CO})_8$ -catalyzed alkyne cyclotrimerization reaction¹² of (**2**) in 58% yield. On deprotection of the TMS group of (**3**) to form the iodide, the slightly soluble hexakis(4-iodo)benzene (**4**) was obtained in 80% yield. This product precipitates during the reaction, resulting in a high yield and simple purification. As the fourth and last step, the desired final compound (**5**) was obtained by oxidation of (**4**) by the Scholl reaction with

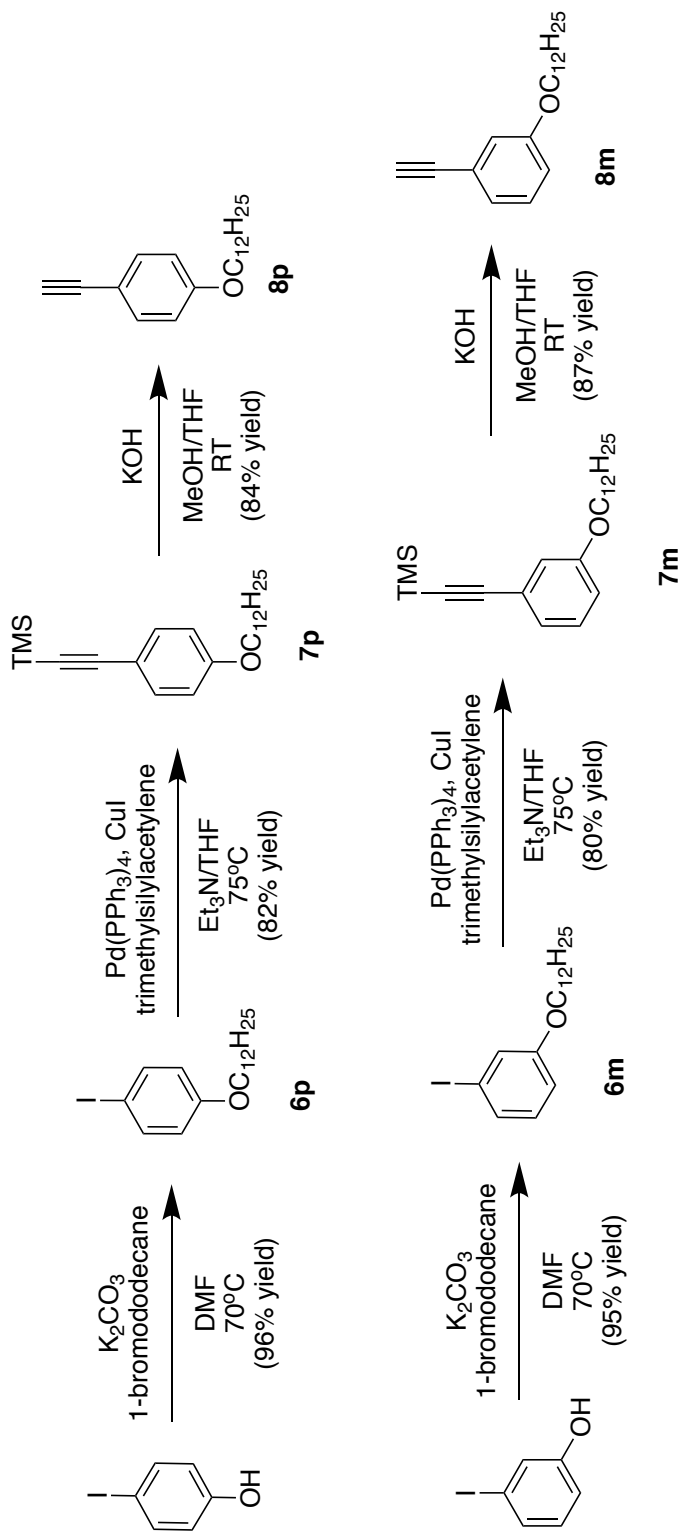
iron (III) chloride dissolved in nitromethane.¹³ After quenching and precipitation in methanol, **(5)** was obtained in 73% yield as a yellow powder. Since **(5)** is insoluble in common solvents, it was used in the next step without further purification and characterization.

For both the para- (**8p**) and meta- (**8m**) substituents the same synthetic pathway was followed, as shown in Scheme 3.2. Commercially available 4- and 3-iodophenol was substituted with a dodecyl alkane group and purified by flash column chromatography to obtain **6p** and **6m** in 96% and 95% yield, respectively. Subsequently, Hagihara-Sonogashira coupling reactions between trimethyl-silylacetylene and compounds **6p** and **6m** in the presence of a Pd(II) catalyst and a copper (I) iodide ligand were carried out. This was immediately followed by desilylation using potassium hydroxide to obtain the pure terminal alkyne compounds **8p** and **8m** in quantitative yields. Despite the insolubility of compound **(5)**, a standard Hagihara-Sonogashira coupling reaction between halogenated HBC core (**5**) and ethynyl-functionalized solubilizing side chains (**8p** & **8m**) was carried out at a high temperature in pyridine. The reaction mixture was degassed by ‘freeze-pump-thaw’ cycles three times to prevent homocoupling between the alkyne compounds. As a result, we obtained soluble **ParaHBC** and **MetaHBC** (Scheme 3.3.) in high yield (39% and 32%, respectively). The synthetic route involves four six-fold transformations and two Hagihara-Sonogashira coupling reactions, all with nearly quantitative conversion. The resulting yellow waxy HBC derivatives exhibit high solubility in

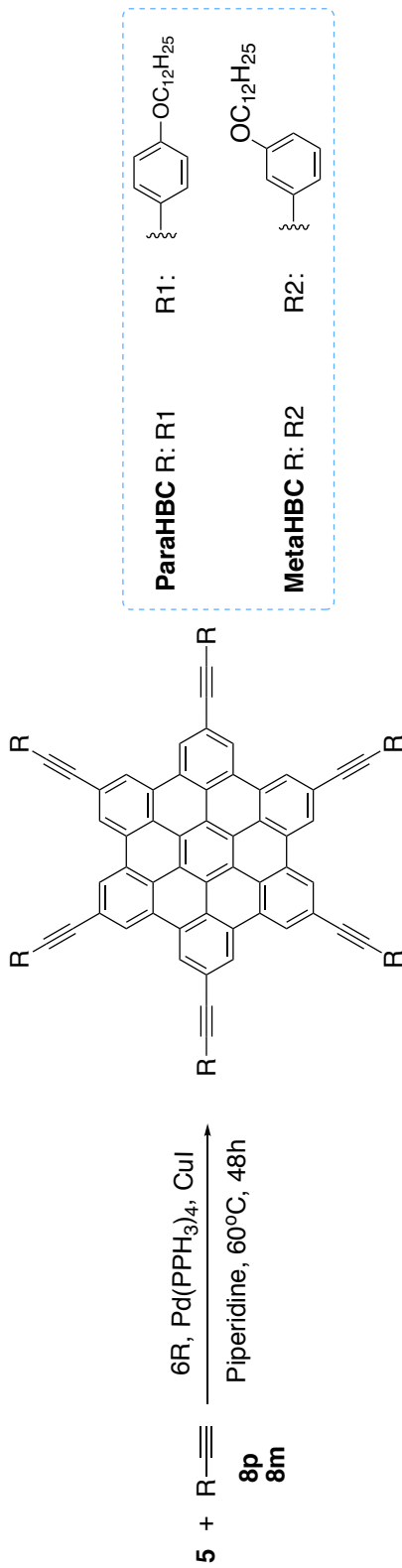
common organic solvents. The structural purity was confirmed by ^1H and ^{13}C NMR spectroscopy, matrix-assisted laser desorption ionization time-of-flight (MALDI-TOF) mass spectrometry and elemental analysis. MALDI-TOF analysis of both derivatives showed a group of isotropic signals at $m/z=2228.49$, matching up with calculated $m/z=2229.21$. The desired quantity of particular elements within **ParaHBC** and **MetaHBC** molecules was achieved by elemental analysis.



Scheme 2.1. Synthesis of HBC core (5)



Scheme 2.2. Synthesis of para- (8p) and meta- (8m) position substitutes



Scheme 2.3. Synthesis of extended HBC derivatives (ParaHBC- MetaHBC)

2.2.2. ^1H NMR spectroscopy

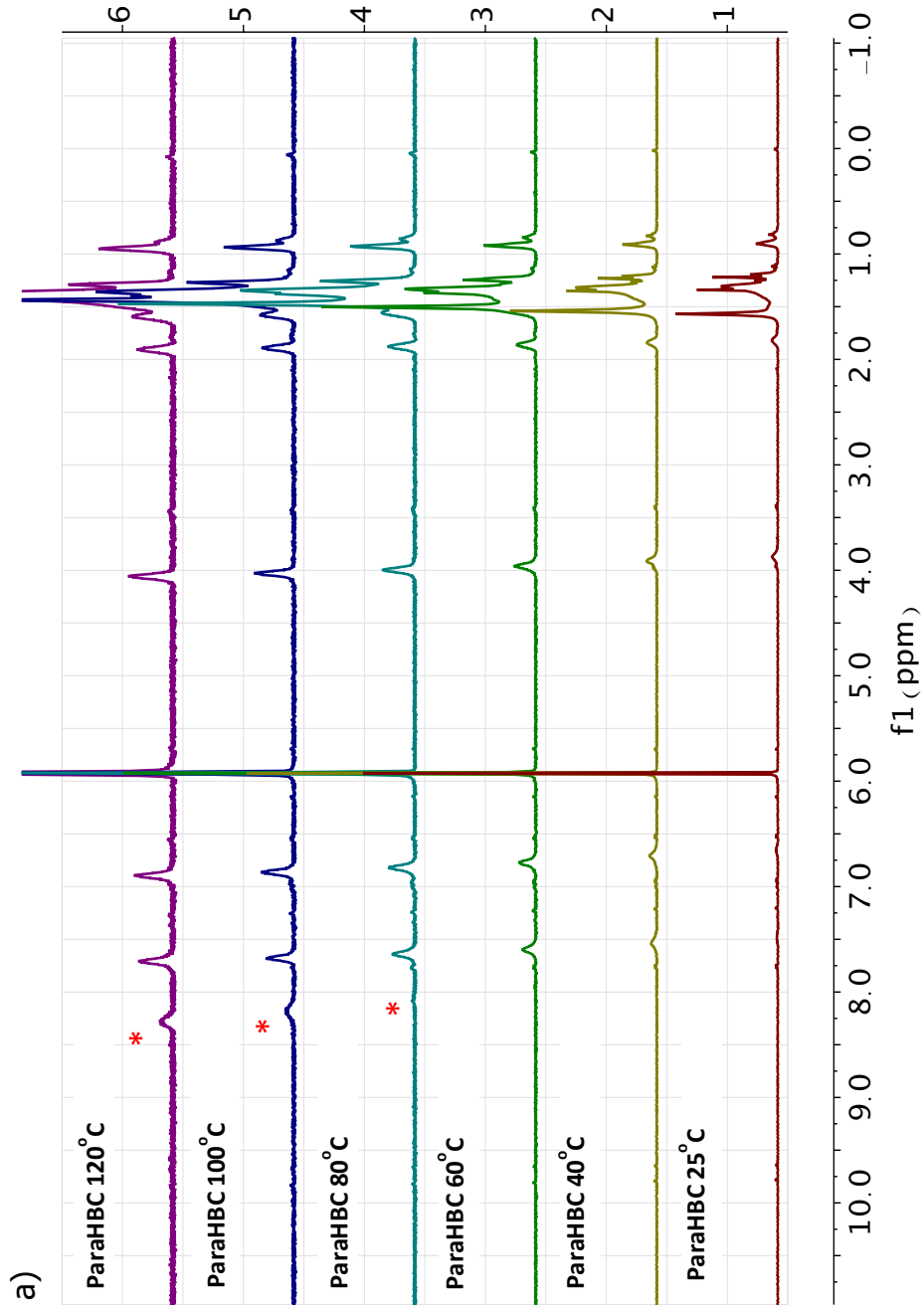
A common approach to study the aggregation of conjugated molecules in solution is by proton (^1H) NMR where the signal due to the protons attached to the aromatic core can be indicative of the aggregation process. Upon aggregation, the intensity and shape of the NMR signals can change due to shielding effects by the neighboring aromatic cores and immobilization of the protons that result in very long relaxation times. Therefore, very low or disappearing intensities for the aromatic H peaks can be observed upon aggregation. As a result, the NMR spectra give information about the molecularly dissolved molecules, non-aggregated, and aggregated molecules, and the size of the aggregates in the solution.¹⁴

For both HBC derivatives considered here, the ^1H NMR spectra were studied in two major regions: the low-field resonance region relating to the protons of the aromatic HBC core and the high-field resonance region relating to the $\alpha\text{-CH}_2$ protons on the alkoxy-phenyl group of the side chains.

The ^1H NMR spectrum for **ParaHBC** in 1,1,2,2-tetrachloroethane- d_2 (at constant concentration of 1.5×10^{-3} M) is shown for different temperatures in Figure 2.2a. In the low-field region, increasing the temperature results in a single resonance peak at 8.08 ppm, appearing around 80 °C. This peak shifts slightly to 8.27 ppm at 120 °C due to de-shielding. At room temperature, the peak is broadened to such an extent that it disappears, indicating that **ParaHBC** exists in aggregated stacks at

room temperature at 10^{-3} M concentration. A similar trend is observed in the high-field region. The α -CH₂ protons on the dodecyloxy chains appear at 3.88 ppm at room temperature and are shifted down-field by 0.17 ppm upon increasing temperature due to increased mobility of the freely rotating dodecyloxy phenyl group.¹⁴ Upon decreasing the concentration down to 3.0×10^{-5} M, the core protons of **ParaHBC** in 1,1,2,2-tetrachloroethane-d₂ at constant temperature (120 °C) shift down-field by 0.56 ppm (red star in Figure 2.2a). This down-field shift with decreasing concentration confirms that even at 120 °C, aggregates are present in the 10^{-3} M solution.¹⁵

For comparison, the ¹H NMR spectrum for **MetaHBC** in 1,1,2,2-tetrachloroethane-d₂ at a concentration of 1.5×10^{-3} M are shown in the temperature range from 25 °C to 120 °C. In the low-field region of the spectrum, isolated resonance peaks due to the core protons of **MetaHBC** appear at 8.36 ppm around 60 °C. Upon increasing the temperature, a 0.32 ppm down-field shift is observed as expected from decreasing aggregation size.¹⁶ Likewise, the α -CH₂ protons on the dodecyloxyphenyl side chains of **MetaHBC** are observed at 3.81 ppm at room temperature and show a down-field shift of 0.22 ppm at 120 °C. The chemical shift of the aromatic core proton of **MetaHBC** at 120 °C is shifted from 8.68 ppm (at 1.5×10^{-3} M) to 9.21 ppm (at 3.0×10^{-5} M), amounting to a down-field shift of 0.53 ppm within the range of decreasing concentration, shown as the black star in Figure 2.2b.



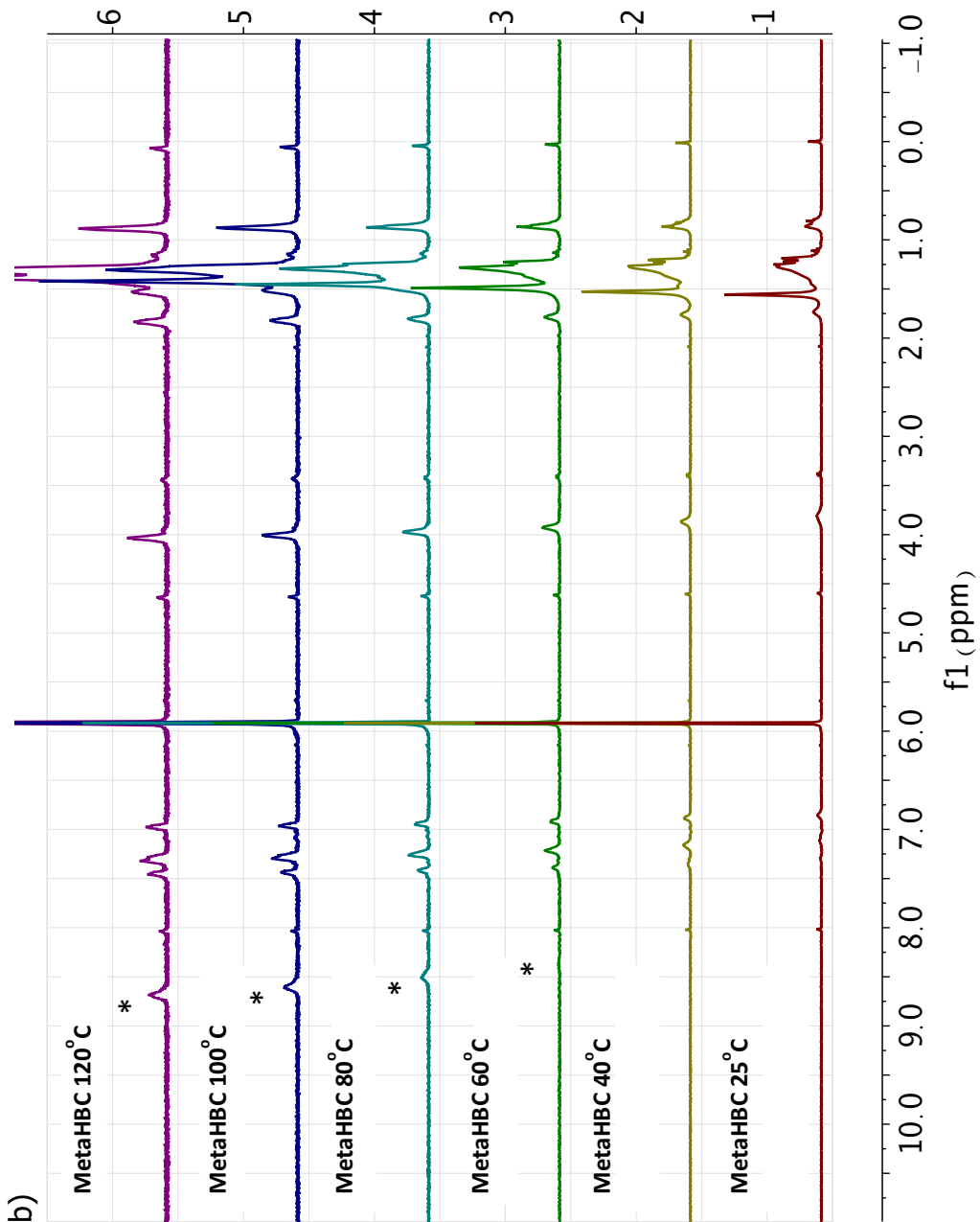


Figure 2.2. Temperature dependent ^1H NMR spectra of a) **ParaHBC** and b) **MetaHBC** in 1,1,2,2-tetrachloroethane- d_2 at $1.5 \times 10^{-3}\text{M}$, from 25 °C to 120 °C

The chemical shift of the NMR peaks due to protons attached core of HBC obtained from temperature-dependent ^1H NMR measurements at a concentration of 1.5×10^{-3} M are compared in Figure 2.3a. The aromatic core protons of **ParaHBC** shift 0.17 ppm down-field starting around 80 °C. For **MetaHBC**, the down-field shift of the core-protons that appears already at 60 °C is 0.32 ppm over this temperature range. These results indicate that **ParaHBC** shows a stronger tendency to aggregate than **MetaHBC**.⁷ A similar picture arises in concentration-dependent measurements (Figure 2.3b), where the signal due to the aromatic proton on **ParaHBC** shifts to 8.83 ppm at the lowest concentration. For **MetaHBC**, it is at 9.21 ppm. This down-field shift for **MetaHBC** compared to **ParaHBC** implies reduced interactions and possibly smaller aggregate sizes for **MetaHBC** in solution. The intensity of the NMR peaks arising from non-aggregated species imply that both derivatives do not exist as fully individually dissolved molecules at room temperature, even at low concentrations (3.023×10^{-5} M).

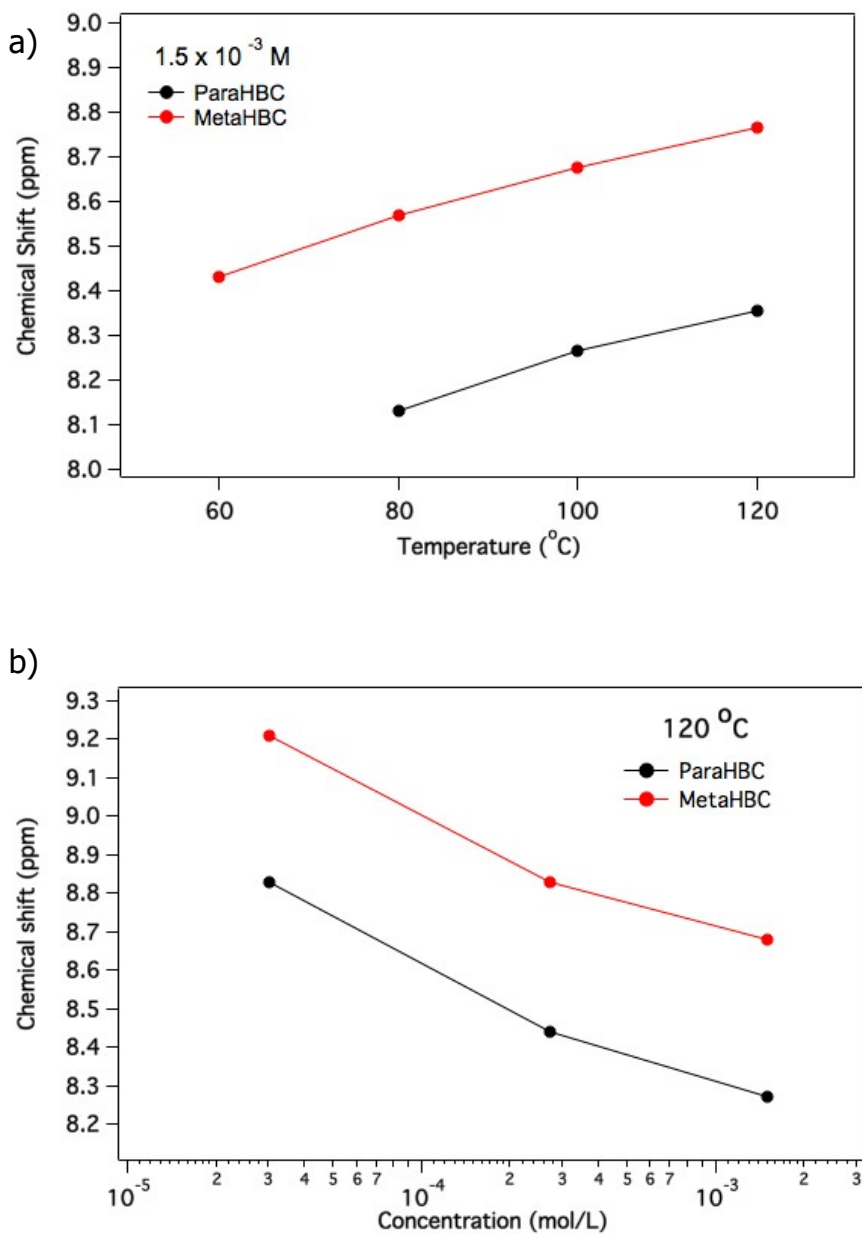


Figure 2.3. a) Temperature dependent ¹H NMR chemical shift of HBC core protons recorded in 1,1,2,2-tetrachloroethane-d₂ from 25 °C to 120 °C at constant concentration 1.5 x 10⁻³ M b)

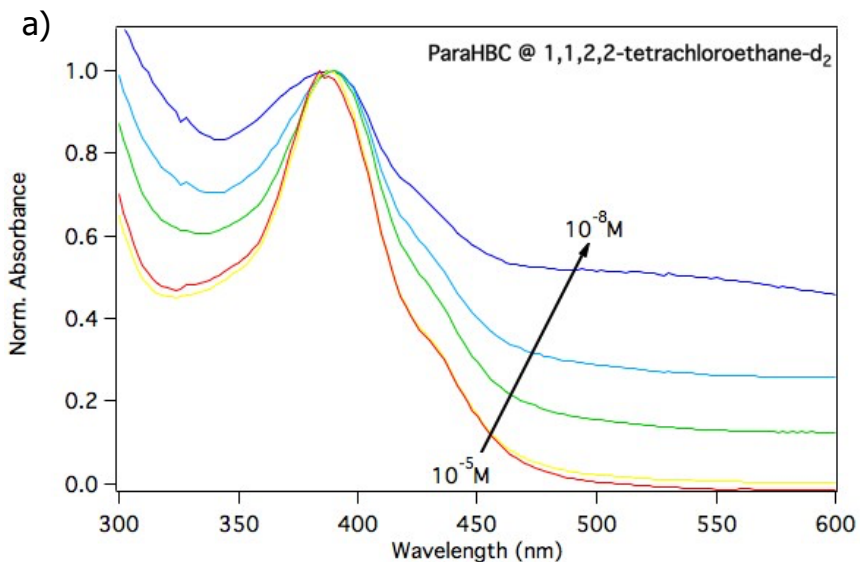
Concentration dependent spectra of ^1H NMR chemical shift of HBC core protons recorded in 1,1,2,2-tetrachloroethane- d_2 from 1.5×10^{-3} M to 3.02×10^{-5} M at constant temperature 120 °C.

2.2.3. Optical properties

While the temperature and concentration-dependent NMR measurements described above clearly show differences in the aggregation behavior of **ParaHBC** and **MetaHBC**, the concentration limitations in ^1H NMR measurements make it impossible to achieve fully molecularly dissolved HBCs. Additional insight into aggregation properties of HBC derivatives can be obtained through a concentration- and temperature-dependent UV/vis absorption and photoluminescence measurements. The formation of self-assembled aggregates via π - π interactions in solution is a typical feature of substituted HBCs. It is accompanied by changes in the intensity and the shape of the absorption and emission spectrum.^{14,17-20}

The UV/Vis absorption spectra for **ParaHBC** and **MetaHBC** are shown in Figure 2.4 in the concentration range from 10^{-5} to 10^{-9} M in 1,1,2,2-tetrachloroethane- d_2 . Both **ParaHBC** and **MetaHBC** exhibit the same maximum at ~ 390 nm, which is designated as the β -band based on Clar's nomenclature.²¹⁻²⁴ At longer wavelengths where the ρ -band appears near 420 nm, clear differences between the two compounds are observed. As the concentration decreases from $\sim 10^{-6}$ M to $\sim 10^{-7}$ M, the characteristic β -band in **ParaHBC** remains at 390 nm with a slight increase in

the intensity of ρ -band (shoulder), see Figure 2.4a. In contrast, concentration-dependent UV-vis spectra for **MetaHBC** (Figure 2.4b) display sharper and more resolved features of both the β - and ρ -bands due to the lower tendency to aggregate.¹⁶ Although the β -band for **MetaHBC** is observed at the same position (390 nm) as for **ParaHBC** at a 1.25×10^{-7} M concentration; the band is narrower with a much sharper ρ -band appearing at 419 nm upon decreasing the concentration.



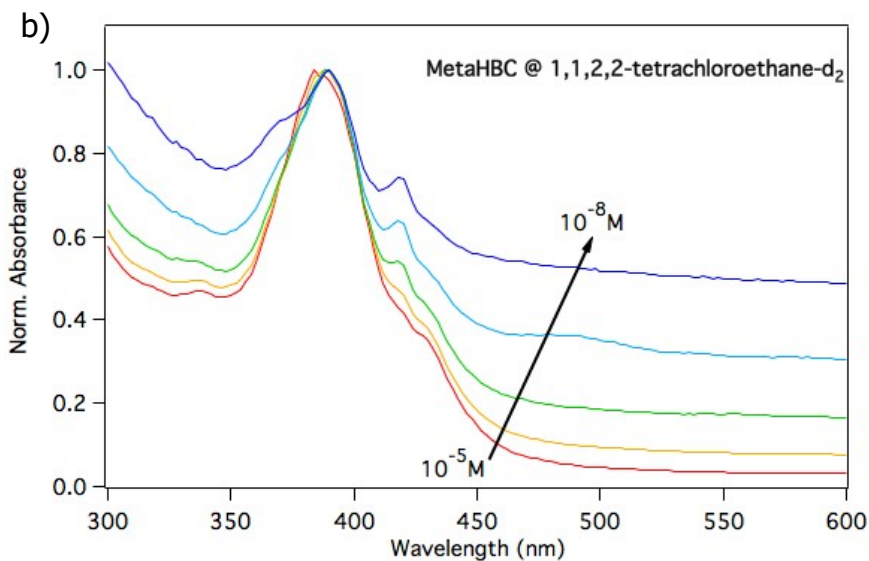


Figure 2.4. Concentration-dependent UV-vis absorption spectra of a) **ParaHBC** and b) **MetaHBC** in 1,1,2,2-tetrachloroethane-d₂ from 10⁻⁶ M to 10⁻⁹ M at a room temperature

Temperature-dependent UV-vis absorption measurements shown in Figure 2.5 give a similar picture. For **ParaHBC** shown in Figure 2.5a at a concentration of 2.48×10^{-7} M, the spectral changes related to aggregation are more clearly observed than in the concentration-dependent spectra. At 25 °C, a broad featureless β -band with a maximum at 391 nm is observed. The ρ -band at 422 nm apparent as a shoulder at 25 °C develops into a sharp band upon increasing temperature. A slightly different picture arises in the temperature-dependent UV-vis spectra for **MetaHBC** shown in Figure 2.5b. Also, the characteristic β -band and ρ -band are

observed in this case. However, the ρ -band is already clearly resolved at 25 °C and does not change much on increasing the temperature, see Figure 2.4b The presence of a sharp ρ -band is attributed to ordered dimeric species or molecularly dissolved HBCs, while formation of larger aggregates leads to broadening and eventual disappearance of this band under the β -band at 390 nm.^{25,26}

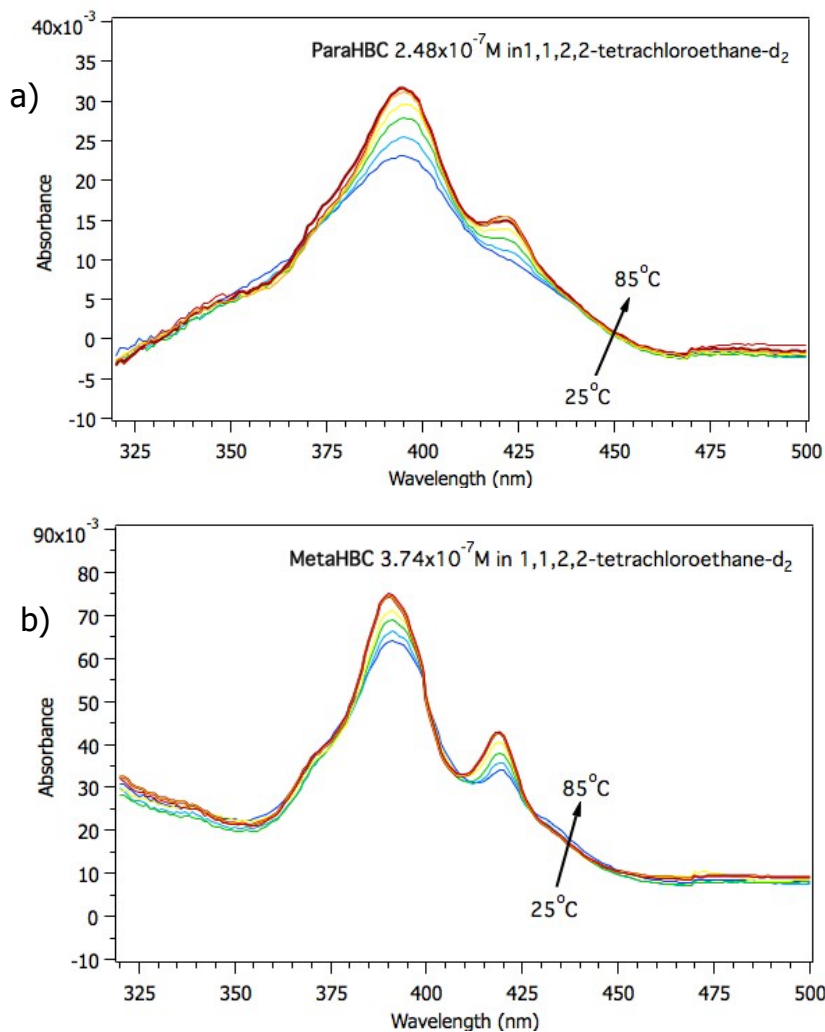


Figure 2.5. Temperature-dependent UV-vis absorption spectra of a) **ParaHBC** and b) **MetaHBC** in 1,1,2,2-tetrachloroethane-d2 from 25 °C to 85 °C at a constant concentration $\sim 3 \times 10^{-7}$ M.

An alternative optical approach to monitor aggregation is by photoluminescence, which is very sensitive to aggregation as the emission quantum yield and the shape of the emission spectrum can change substantially.²⁰ Concentration-dependent photoluminescence spectra were measured for both compounds at concentrations ranging from 10^{-9} M to 10^{-6} M, as shown in Figure 2.6. For both compounds in dilute solutions (10^{-8} - 10^{-9} M), the emission spectra are relatively narrow and characterized by a complicated vibrational fine structure. At higher concentrations, the formation of aggregates decreases the vibrational fine structure, and a significant broadening of the emission towards lower energy is observed. The relative decrease of the intensity in the high-energy peaks at 499, 510, and 521 nm in **ParaHBC** accompanied by an increase in emission intensity of the broader bands at 558 and 572 nm is indicative of the increased aggregation at higher concentrations.²⁷ For **MetaHBC**, a very similar trend is observed. Nevertheless, in this case, the shift from high energy to low energy emission occurs at somewhat higher concentrations, in agreement with the lower tendency of **MetaHBC** to aggregate concluded from NMR and UV/vis measurements above.

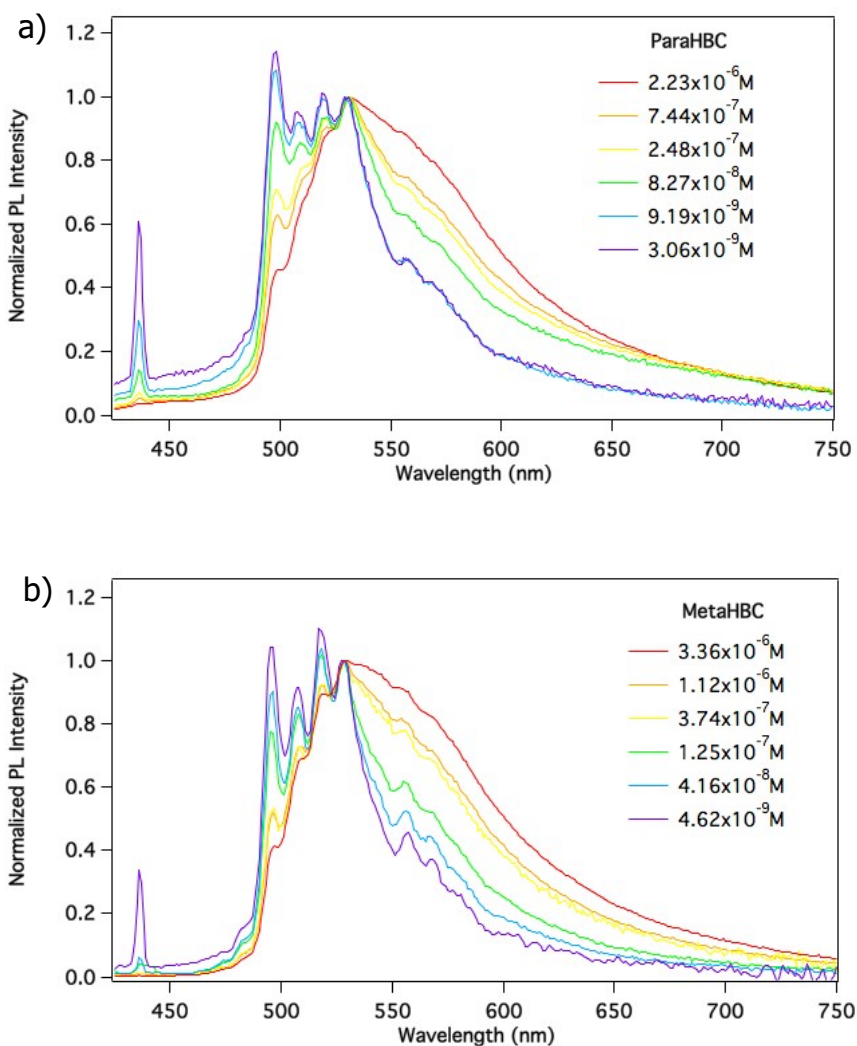


Figure 2.6. Concentration-dependent photoluminescence emission spectra of a) **ParaHBC** b) **MetaHBC** at 25 °C between the concentrations of 10^{-9} M and 10^{-6} M in 1,1,2,2-tetrachloroethane- d_2 ; normalized to the maximum band 530 nm.

2.2.4. Effect of solvent

As discussed above, both **ParaHBC** and **MetaHBC**

derivatives show a strong tendency to aggregate in 1,1,2,2-tetrachloroethane-d₂, even at very low concentrations. However, the tendency to aggregate is known to depend significantly on the nature of the solvent.²⁸ To characterize the aggregation in other solvents, concentration-dependent UV/vis measurements were performed for both compounds in different solvents chosen based on increasing solvent polarity (1,1,2,2-tetrachloroethane, toluene, THF, chloroform and trichlorobenzene) with concentrations ranging from 10⁻⁸ to 10⁻⁵ M.

Generally, HBCs exhibit a stronger tendency to aggregate in higher polarity solvents, although the polarizability and aromaticity of the solvent also play a role.^{16,29,30} In previous work, it has been reported that the aromatic chlorinated solvent trichlorobenzene is a good solvent for molecularly dissolving HBCs.^{22,31} In Figure 2.7 the UV-vis absorption spectra for **ParaHBC** and **MetaHBC** in trichlorobenzene are compared at different concentrations. For both compounds, both the β -band and the ρ -band are clearly distinguishable, in contrast to the UV-vis spectra in tetrachloroethane. This indicates better solvation and hence weaker aggregation in trichlorobenzene.²⁵ Closer inspection of the spectra in Figure 2.7 shows that the ρ -band is sharper for **ParaHBC** than for **MetaHBC** at each concentration, consistent with a higher tendency to aggregate for the latter.

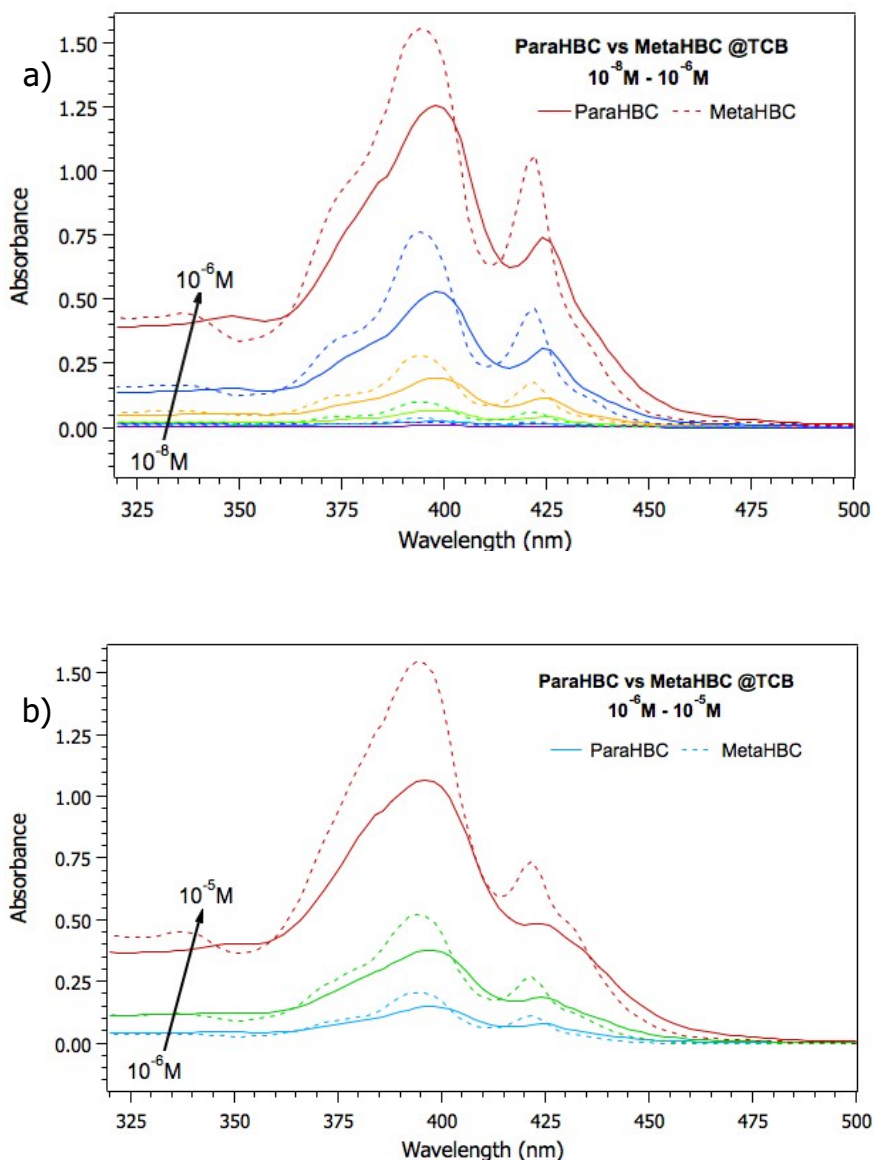
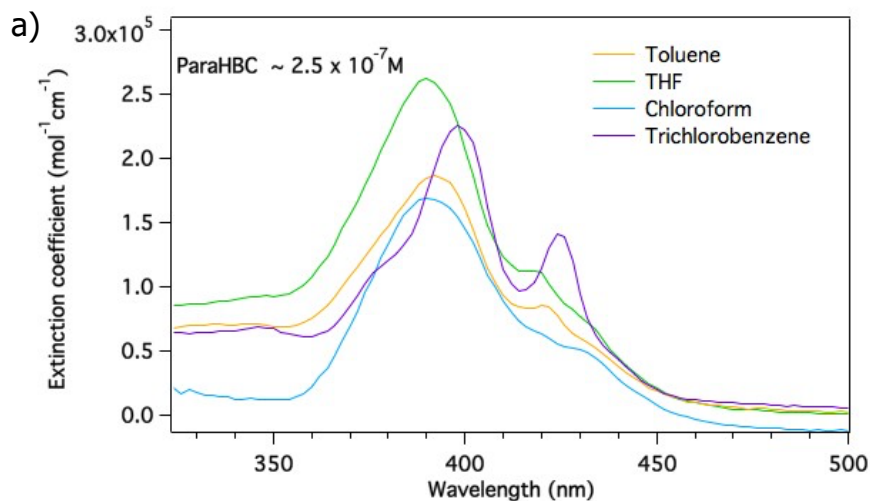


Figure 2.7. UV/vis absorption spectra of ParaHBC and MetaHBC at room temperature in the concentration of a) 10^{-8} M – 10^{-6} M in 10mm cuvette b) 10^{-6} M- 10^{-5} M in 1mm cuvette in trichlorobenzene.

Variation of the solvent (other than tetrachloroethane and trichlorobenzene) shows varying aggregation tendencies, as evident from Figure 2.8. The most apparent difference is that the sharpness of the ρ -band varies, which is an indicator of the aggregation tendency. Again, clear differences are observed between **ParaHBC** and **MetaHBC**. This is particularly evident in THF and toluene, where the ρ -band is more clearly defined for **MetaHBC** than for **ParaHBC**.



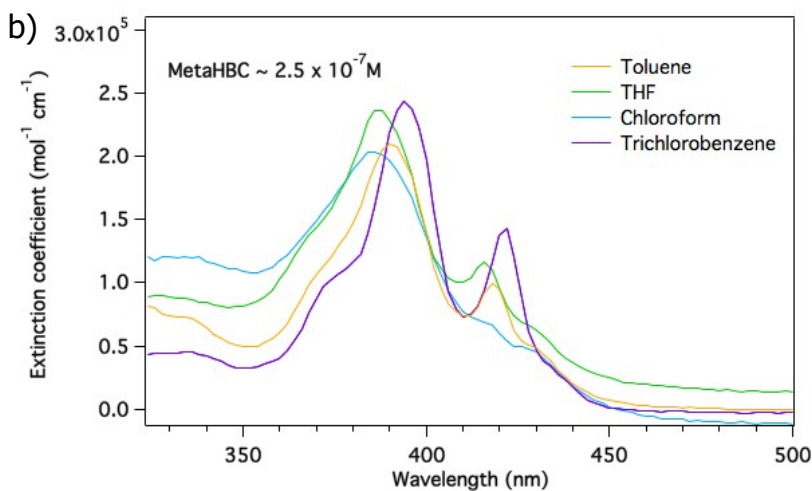


Figure 2.8. UV-vis absorption spectra of a) **ParaHBC** and b) **MetaHBC** at room temperature in the concentration of 2.5×10^{-7} M for different solvents: 1,1,2,2-tetrachloroethane-d₂, toluene, THF, chloroform, and trichlorobenzene.

2.3. Summary and Discussion

As indicated by the results presented above, the nature of the substitution of the solubilizing side chains strongly influences the aggregation of HBC derivatives in the solution. This work considers two novel HBC derivatives that only differ in the substitution position, either on the meta- or para- position of phenylacetylene connected to the HBC core. Therefore, the two molecules are isomers, and only the shape or topology of the molecules are different. However, this may significantly affect their steric interactions and stacking geometry as the steric requirements of these compounds are very different. In NMR

measurements, major differences in the position and intensity of the ^1H NMR feature due to the aromatic protons on **ParaHBC** and **MetaHBC** cores and the $\alpha\text{-CH}_2$ protons the dodecyloxy phenyl chains were observed. These provide a first indication of the aggregation properties in the solution. At a concentration of 1.5×10^{-3} M, an increasing down-field shift of the position of the aromatic protons on **MetaHBC** with increasing temperature implies a decrease in the size of the aggregates.¹⁴ Under the same conditions, the aromatic protons on the **ParaHBC** core and the side chain show significant line broadening and higher shielding than **MetaHBC**. The resulting up-field shift is associated with stronger $\pi\text{-}\pi$ interactions between the neighboring cores and the interlocking of the phenyl rings in the side chains, leading to more organized aggregates.³² Apart from the shifts in the NMR spectra, the peak related to the aromatic proton appears at 60 °C in **MetaHBC**, whereas it can only be seen at higher temperature (~80 °C) in **ParaHBC**. This clearly indicates enhanced aggregation in **ParaHBC**.

In addition, the concentration dependence of the chemical shift positions for both **ParaHBC** and **MetaHBC** is very similar due to decreased aggregation size in both derivatives. However, the position of the peaks differs considerably. At the concentration of 3.023×10^{-5} M) at 120 °C, the aromatic proton peak for **ParaHBC** appears at 8.83 ppm, while **MetaHBC** under the same conditions appears at 9.21 ppm. Interestingly, the low relative intensity of the aromatic proton peaks indicates that both derivatives do not exist as fully dispersed molecules even at low concentrations ($3.023 \times$

10^{-5} M) and high temperatures.

Due to concentration limitations in NMR, further investigation on aggregation properties of derivatives were performed by temperature and concentration-dependent UV/vis absorption and photoluminescence emission measurements. The optical spectra of both derivatives are similar to those observed with the alkyl- and alkoxy- substituted HBC derivatives.^{26,33} Lowering the concentration for both compounds lead to a sharpening of both β - and ρ -bands, which is attributed to de-aggregation of the HBC stacks.²⁵ Of particular interest in these measurements is the ρ -band, which indicates isolated (non-aggregated) molecules in solution. This is also reflected above in solvent-dependent measurements showing that the ρ -band is much more pronounced for good solvents than for bad solvents. For **MetaHBC** this band becomes pronounced at lower temperatures than for **ParaHBC**, indicating stronger aggregation in the latter. Both HBC derivatives predominantly exist as monomeric species at the highest temperature (85 °C at a concentration of 10^{-7} M). This is an almost an order of magnitude lower concentration than reported for other systems, including HBC-C₁₂ (for which the highest mobility has been reported) and analogous bulky alkoxy phenyl substituted HBC derivatives.^{7,14}

A similar picture of concentration-dependent fluorescence measurements support the outcomes of the NMR and UV-vis studies. Low concentrations lead to emission spectra will very well-defined vibrational fine structures. Increasing the concentration diminishes the high energy emission and introduces

a broad featureless emission at low energies characteristic of stacked aggregates in solution.

Overall, all measurements presented above indicate that the stacking is significantly affected by the substitution position of the flexible side chains. When they are attached in the *para*-position, the conformational freedom is smaller than *meta*-substitution, where the curved nature of the side chains allows much more disordered structures. In solution, this leads to a stronger tendency to aggregate and very likely also to the formation of larger size aggregates in the case of **ParaHBC**. It is important to realize here that the aggregation in solution is a subtle balance of interaction between the dissolved molecules themselves and the solute-solvent interaction. This means that the interactions and the resulting stacking geometries in solution-based aggregates are not necessarily the same as in the absence of solvent. This is particularly relevant for applying these materials in devices since this pertains to the solid state.

2.4. Conclusion

In this chapter, the synthesis is described of two novel HBC derivatives with sterically demanding alkoxy side chains that are strategically introduced in the *meta*- and *para*- positions on the phenyl rings attached to the HBC core. Both **ParaHBC** and **MetaHBC** display a high tendency to aggregate in solution, as shown by concentration- and temperature-dependent ¹H-NMR measurements. Due to the attachment of phenylacetylene spacers

attached to the HBC core, the expanded aromatic system results in stronger aggregation than HBC derivatives such as HBC-C₁₂ and HBC-PhC₁₂ due to stronger π - π interactions and decreased steric hindrance close to the aromatic core.

By combining concentration and temperature-dependent NMR, UV-vis absorption, and fluorescence experiments, we show that the position of the substituent (meta- vs para-) has a pronounced effect on the aggregation. In all experiments considered, the **ParaHBC** compound shows a stronger tendency to aggregate than **MetaHBC**. This is attributed to the larger conformational freedom present in **MetaHBC**, which can adopt more disordered conformations which hamper aggregation. In addition to a pronounced difference in aggregation strength, the NMR measurements also suggest very different stacking conformations for the two compounds, which can have a noticeable effect on the charge transport properties.

2.5. References

1. Wöhrle, T. *et al.* Discotic Liquid Crystals. *Chemical Reviews* **116**, 1139–1241 (2016).
2. Laschat, S. *et al.* Discotic liquid crystals: From tailor-made synthesis to plastic electronics. *Angewandte Chemie - International Edition* **46**, 4832–4887 (2007).
3. Lehn, J. M. From supramolecular chemistry towards constitutional dynamic chemistry and adaptive chemistry. *Chemical Society Reviews* **36**, 151–160 (2007).
4. Termine, R. & Golemme, A. Charge mobility in discotic liquid crystals. *International Journal of Molecular Sciences* vol. 22 1–51 (2021).
5. Warman, J. M. & van de Craats, A. M. Charge Mobility in Discotic Materials Studied by Pr-Trmc. *Molecular Crystals and Liquid Crystals* **396**, 41–72 (2003).
6. Piris, J., Debije, M. G., Watson, M. D., Müllen, K. & Warman, J. M. The Mobility and Decay Kinetics of Charge Carriers in Discotic Hexabenzocoronenes. *Advanced Functional Materials* **14**, 1047–1052 (2004).
7. Wu, J., Watson, M. D., Zhang, L., Wang, Z. & Müllen, K. Hexakis(4-iodophenyl)- p eri -hexabenzocoronene- A Versatile Building Block for Highly Ordered Discotic Liquid Crystalline Materials. *J Am Chem Soc* **126**, 177–186 (2004).

8. Kaafarani, B. R. Discotic Liquid Crystals for Opto-Electronic Applications † ‡. *Chemistry of Materials* **23**, 378–396 (2011).
9. Schmidt-Mende, L. *et al.* Self-organized discotic liquid crystals for high-efficiency organic photovoltaics. *Science (1979)* **293**, 1119–1122 (2001).
10. Craats, A. M. van de *et al.* Record Charge Carrier Mobility in a Room-Temperature Discotic Liquid-Crystalline Derivative of Hexabenzocoronene. *Advanced Materials* **11**, 1469–1472 (1999).
11. Wu, J., Watson, M. D. & Müllen, K. The Versatile Synthesis and Self-Assembly of Star-Type Hexabenzocoronenes. *Angewandte Chemie - International Edition* **42**, 5329–5333 (2003).
12. Hardesty, J. H., Koerner, J. B., Albright, T. A. & Lee, G.-Y. Theoretical Study of the Acetylene Trimerization with CpCo. *J Am Chem Soc* **121**, 6055–6067 (1999).
13. Grzybowski, M., Skonieczny, K., Butenschön, H. & Gryko, D. T. Comparison of Oxidative Aromatic Coupling and the Scholl Reaction. *Angewandte Chemie International Edition* **52**, 9900–9930 (2013).
14. Kastler, M., Pisula, W., Wasserfallen, D., Pakula, T. & Müllen, K. Influence of Alkyl Substituents on the Solution- and Surface-Organization of Hexa- p e r i - hexabenzocoronenes. *J Am Chem Soc* **127**, 4286–4296 (2005).

15. Wasserfallen, D. *et al.* Suppressing aggregation in a large polycyclic aromatic hydrocarbon. *J Am Chem Soc* **128**, 1334–1339 (2006).
16. Wu, J. *et al.* Controlled Self-Assembly of Hexa- p eri - hexabenzocoronenes in Solution. *J Am Chem Soc* **126**, 11311–11321 (2004).
17. Navale, T. S., Ivanov, M. V., Hossain, M. M. & Rathore, R. FHBC, a Hexa-*peri*-hexabenzocoronene–Fluorene Hybrid: A Platform for Highly Soluble, Easily Functionalizable HBCs with an Expanded Graphitic Core. *Angewandte Chemie - International Edition* **57**, 790–794 (2018).
18. Ito, S. *et al.* Bishexa-*peri*-hexabenzocoronenyl: A “superbiphenyl.” *J Am Chem Soc* **122**, 7698–7706 (2000).
19. Hoeben, F. J. M., Jonkheijm, P., Meijer, E. W. & Schenning, A. P. H. J. About supramolecular assemblies of π -conjugated systems. *Chemical Reviews* **105**, 1491–1546 (2005).
20. Prince, R. B., Saven, J. G., Wolynes, P. G. & Moore, J. S. Cooperative conformational transitions in phenylene ethynylene oligomers: Chain-length dependence. *J Am Chem Soc* **121**, 3114–3121 (1999).
21. Clar, E. & Stephen, J. F. The synthesis of 1:2, 3:4, 5:6, 7:8, 9:10, 11:12-hexabenzocoronene. *Tetrahedron* **21**, 467–470 (1965).
22. Clar, E., Ironside, C. T. & Zander, M. The electronic interaction between benzenoid rings in condensed aromatic hydrocarbons. 1 : 12-2 : 3-4 : 5-6 : 7-8 : 9-10 : 11-

- hexabenzocoronene, 1: 2-3: 4-5: 6-10: 11-tetrabenzoanthanthrene, and 4: 5-6: 7-11: 12-13: 14-tetrabenzoperopyrene. *Journal of the Chemical Society (Resumed)* 142 (1959) doi:10.1039/jr9590000142.
23. Zander, M. Polycyclic Hydrocarbons. Band II. Von E. Clar. Academic Press, London-New York; Springer-Verlag, Berlin-Göttingen-Heidelberg 1964. 1. Aufl., LVIII, 487 S., 153 Abb., geb. DM 78.40. *Angewandte Chemie* **77**, 876–876 (1965).
 24. Fetzer, J. C. THE CHEMISTRY AND ANALYSIS OF LARGE PAHs. *Polycyclic Aromatic Compounds* **27**, 143–162 (2007).
 25. J.M., H. *et al.* High quality dispersions of hexabenzocoronene in organic solvents. *J Am Chem Soc* **134**, 12168–12179 (2012).
 26. Kastler, M., Schmidt, J., Pisula, W., Sebastiani, D. & Müllen, K. From Armchair to Zigzag Peripheries in Nanographenes. *J Am Chem Soc* **128**, 9526–9534 (2006).
 27. Samuel, I. D. W., Rumbles, G. & Collison, C. J. Efficient interchain photoluminescence in a high-electron-affinity conjugated polymer. *Physical Review B* **52**, R11573–R11576 (1995).
 28. Biasutti, M. *et al.* Photophysical properties of a new class of discotic liquid crystalline compounds: Hexa (dodecyl) hexa peri benzyl coronene. *Bulletin des Sociétés Chimiques Belges* **106**, 659–664 (1997).

29. Wu, J., Li, J., Kolb, U. & Müllen, K. A water-soluble hexa-peri-hexabenzocoronene: Synthesis, self-assembly and role as template for porous silica with aligned nanochannels. *Chemical Communications* 48–50 (2006) doi:10.1039/b511868a.
30. Tsai, C. Y. *et al.* Enhancing the emission of hexa-peri-hexabenzocoronene-containing polynorbornene via electron donating, unsymmetric constitution and solvent effects. *Polymer Chemistry* **8**, 3327–3332 (2017).
31. Hendel, W., Khan, Z. H. & Schmidt, W. Hexa-peri-benzocoronene, a candidate for the origin of the diffuse interstellar visible absorption bands? *Tetrahedron* **42**, 1127–1134 (1986).
32. Jenneskens, L. W. *et al.* [5]Paracyclophane. *J Am Chem Soc* **107**, 3716–3717 (1985).
33. Wang, Z., Watson, M. D., Wu, J. & Müllen, K. Partially stripped insulated nanowires: a lightly substituted hexa-peri-hexabenzocoronene-based columnar liquid crystal. *Chem. Commun.* **4**, 336–337 (2004).

Appendix

Synthesis

General information:

All chemicals and solvents were used without further purification. All reactions were carried out under inert atmosphere. Prior to the reactions, all solid reagents were kept under vacuum and inert atmosphere for 15 minutes each.

1,2-bis(4-(trimethylsilyl)phenyl)ethyne (2): To a stirred solution of commercially available **1** (1.5 g, 4.46 mmol) in anhydrous THF (72 mL) was added TMSCl (1.24 g, 11.4 mmol) and mixture was cooled to -85 °C under nitrogen atmosphere. Then n-BuLi (4.5 mL, 10.27 mmol) was added dropwise. The reaction was stirred at -85 °C for 2 hours and then allowed to come to room temperature overnight. The reaction was quenched with brine and extracted with ethyl acetate (x3). The combined organic layers were dried over MgSO₄ and solvent was evaporated. The remaining solid was recrystallized in ethanol to obtain **3** as a white solid (1.20 g, 83% yield). ¹H NMR (400 MHz, Chloroform-*d*) δ 7.49 (s, 8H), 0.27 (s, 18H) ¹³C NMR (101 MHz, Chloroform-*d*) δ 141.01, 133.18, 130.66, 123.56, 89.90, -1.25.

(3',4',5',6'-tetrakis(4-(trimethylsilyl)phenyl)-[1,1':2',1''-terphenyl]-4,4''-diyl)bis(trimethylsilane) (3): Into a solution of **2** (0.9 g, 2.79 mmol) in 1,4-dioxane, Co₂(CO)₈ (0.190 g, 0.55 mmol) was added under nitrogen atmosphere. After the addition of

$\text{Co}_2(\text{CO})_8$, the mixture turned to black immediately. The solution mixture was heated to reflux for 18 hours. After completion of reaction, the solvent evaporated and the remaining solid washed with ether. The ethereal suspension was filtered and the filtrate was diluted with cold ethanol to precipitate the product. The mixture was filtered with suction filter and washed with ethanol several times to yield **3** as a white solid (1.56 g, 58% yield). ^1H NMR (400 MHz, Chloroform-*d*) δ 6.96 (d, $J=8.0$ Hz, 12H), 7.77 (d, $J=8.0$ Hz, 12H), 0.08 (s, 54H). ^{13}C NMR (101 MHz, Chloroform-*d*) δ 141.0, 140.2, 136.3, 131.3, 130.7, -1.2.

4,4''-diiodo-3',4',5',6'-tetrakis(4-iodophenyl)-1,1':2',1''-terphenyl (4): A solution of **3** (0.5 g, 0.52 mmol) in anhydrous DCM (25 mL) was cooled to 0 °C by using an ice bath under inert atmosphere. Then, ICl (3.1 mL, 3.1 mmol) was added dropwise at 0 °C. After completion of addition, the reaction mixture was stirred at room temperature for 18 hours. The precipitated product was filtered from the mixture and washed with 1,4-dioxane. The poorly soluble compound **4** was obtained as a white solid (533 mg, 80% yield). ^1H NMR (400MHz, $\text{C}_5\text{D}_5\text{N}$) δ 7.44 (d, $J=4.0$ Hz, 12H), 6.92 (d, $J=8.0$ Hz, 12H). ^{13}C NMR (100 MHz, $\text{C}_5\text{D}_5\text{N}$) δ 140.5, 140.4, 137.3, 136.0, 134.2.

2,5,8,11,14,17-hexaiodoheptabenzocoronene (5): To a mixture of **4** (500 mg, 0.49 mmol) and anhydrous DCM (250 mL) is added FeCl_3 (2.49 g, 15.4 mmol) in nitromethane (6.6 mL) under nitrogen atmosphere. The mixture was stirred for 24

hours at room temperature. Then, the reaction was quenched with methanol to precipitate the yellow product. The mixture was filtered and the residue washed with DCM to yield the insoluble product **5** as a yellow solid (362 mg, 73% yield). Due to the insolubility, no analysis was done and the product was used as such for the further step.

1-(dodecyloxy)-4-iodobenzene (6p): A solution of commercially available 4-iodophenol (3 g, 13.6 mmol) in 20 mL DMF was added into anhydrous potassium carbonate (11.3 g, 81.8 mmol) under inert atmosphere. The solution mixture heated to 70°C and 1-bromododecane (3.96 mL, 16.5 mmol) was added into mixture, stirred overnight. Solution was then poured into 100 mL water and extracted with DCM (3x50 mL). Combined organic layer was washed with 1M HCl and brine several times and dried over MgSO₄. After the evaporation of solvent, the residue product was purified by a flash column (hexane) to give **6p** as a white solid (5.08 g, 96% yield). ¹H NMR (400 MHz, Chloroform-*d*) δ 7.55 – 7.49 (ddd, 2H), 6.68 – 6.62 (ddd, 2H), 3.89 (t, *J* = 6.6 Hz, 2H), 1.74 (dq, *J* = 8.3, 6.6 Hz, 2H), 1.41 (q, *J* = 7.5 Hz, 2H), 1.25 (s, 16H), 0.91 – 0.83 (m, 3H). ¹³C NMR (101 MHz, Chloroform-*d*) δ 159.00, 138.11, 116.91, 68.10, 31.90, 29.64, 29.61, 29.57, 29.54, 29.34, 29.33, 29.12, 25.97, 22.67, 14.10.

1-(dodecyloxy)-3-iodobenzene (6m): A solution of commercially available 3-iodophenol (3 g, 13.6 mmol) in 20 mL DMF was added into anhydrous potassium carbonate (11.3 g, 81.8 mmol) under

inert atmosphere. The solution mixture heated to 70 °C and 1-bromododecane (3.96 mL, 16.5 mmol) was added into mixture, stirred overnight. Solution was then poured into 100 mL water and extracted with DCM (3x50 mL). Combined organic layer was washed with 1M HCl and brine several times and dried over MgSO₄. After the evaporation of solvent, the residue product was purified by a flash column (hexane) to give **6m** as a white solid (5.03 g, 95%yield). ¹H NMR (400 MHz, Chloroform-*d*) δ 7.88 (ddd, 1H), 7.84 (ddd, 1H), 7.02 - 6.98 (ddd, 2H), 4.00 (t, *J* = 6.6 Hz, 2H), 1.86 (dq, *J* = 8.3, 6.6 Hz, 2H), 1.44 (q, *J* = 7.5 Hz, 2H), 1.31 (s, 16H), 0.96 – 0.86 (m, 3H). ¹³C NMR (101 MHz, Chloroform-*d*) δ 158.20, 137.40, 131.10, 121.2, 116.71, 94.10, 69.10, 31.80, 29.67, 29.62, 29.61, 29.42, 29.37, 29.32, 29.20, 25.80, 22.62, 14.12.

((4-(dodecyloxy)phenyl)ethynyl)trimethylsilane (7p): A mixture of **6p** (1 g, 2.57 mmol), bis(triphenylphospine)palladium(II) dichloride (105 mg, 0.15 mmol), copper(I) iodide (29 mg, 0.15 mmol) in THF (20 ml) was cooled down to 0 °C under nitrogen atmosphere. Ethynyltrimethylsilane (0.57 mL, 4.12 mmol) was added into mixture dropwise. Then, triethylamine (10 mL) was added, and the mixture was stirred for 20 hours at room temperature in dark. After completion the reaction, solvent was evaporated and the crude mixture purified by column chromatography (hexane/DCM 1:1) to obtain pure **7p** as a yellow liquid (757 mg, 82% yield). ¹H NMR (400 MHz, Chloroform-*d*) δ 7.36 (ddd, 2H), 7.03 (ddd, 2H), 4.10 (t, *J* = 7.43, 2H), 1.81 (m, 2H), 1.37 – 1.23 (m,

18H), 0.86 (m, 3H), 0.3 (s, 9H). ^{13}C NMR (101 MHz, Chloroform-*d*) δ 158.5, 133.4, 123.1, 114.3, 105.0, 99.0, 69.1, 31.8, 29.3-29.4, 25.8, 22.6, 14.0, 0.00

((4-(dodecyloxy)phenyl)ethynyl)trimethylsilane (7m): A mixture of **6m** (1 g, 2.57 mmol), bis(triphenylphosphine)palladium(II) dichloride (105 mg, 0.15 mmol), copper(I) iodide (29 mg, 0.15 mmol) in THF (20 ml) was cooled down to 0°C under nitrogen atmosphere. Ethynyltrimethylsilane (0.57 mL, 4.12 mmol) was added into mixture dropwise. Then, triethylamine (10 mL) was added and the mixture was stirred for 20 hours at room temperature in dark. After completion the reaction, solvent was evaporated and the crude mixture purified by column chromatography (hexane/DCM 2:1) to obtain pure **7m** as a yellow liquid (738 mg, 80% yield). ^1H NMR (400 MHz, Chloroform-*d*) δ 7.70 (ddd, 2H), 7.29 – 7.27 (t, 2H), 6.91 (ddd, $J = 8.2$ Hz, 1H), 3.99 (t, 2H), 1.83 (m, 2H), 1.37 (t, 2H), 1.23 (m, 18H), 0.86 (m, 3H), 0.3 (s, 9H). ^{13}C NMR (101 MHz, Chloroform-*d*) δ 153.0, 131.8, 129.6, 122.1, 116.7, 110.9, 105.0, 99.0, 69.1, 31.8, 29.4, 29.3-29.4, 25.8, 22.6, 14.0, 0.00.

1-(dodecyloxy)-4-ethynylbenzene (8p): To a solution of **7p** (500 mg, 1.39 mmol) in anhydrous THF (6 ml) was added potassium hydroxide (391 mg, 6.97 mmol) in methanol (12 ml) under nitrogen atmosphere. The mixture was stirred for 4 hours at room temperature. When the reaction is completed, the reaction mixture was quenched with saturated aqueous solution of ammonium chloride. The mixture was extracted with diethyl ether and water.

Combined organic layers were dried with MgSO₄. The solvent was evaporated to yield the product **8p** (335 mg, 84% yield) as a colourless liquid. ¹H NMR (400 MHz, Chloroform-*d*) δ 7.36 (ddd, 2H), 6.89 (ddd, 2H), 4.10 (t, *J* = 7.43, 2H), 2.82 (s, 1H), 1.82 (m, 2H), 1.37-1.23 (m, 18H), 0.86 (m, 3H). ¹³C NMR (101 MHz, Chloroform-*d*) δ 158.5, 133.4, 121.7, 114.3, 83.2, 80.0, 69.1, 31.8, 29.4-29.3, 25.8, 22.6, 14.0.

1-(dodecyloxy)-4-ethynylbenzene (8m): To a solution of **7m** (500 mg, 1.39 mmol) in anhydrous THF (6 mL) was added potassium hydroxide (391mg, 6.97mmol) in methanol (12 mL) under nitrogen atmosphere. The mixture was stirred for 4 hours at room temperature. When the reaction is completed, the reaction mixture was quenched with saturated aqueous solution of ammonium chloride. The mixture was extracted with diethyl ether and water. Combined organic layers were dried with MgSO₄. The solvent was evaporated to yield the product **8m** (347 mg, 87% yield) as a colourless liquid. ¹H NMR (400 MHz, Chloroform-*d*) δ 7.70 (ddd, 2H), 7.29 – 7.27 (t, 2H), 6.91 (ddd, *J* = 8.2 Hz, 1H), 3.99 (t, 2H), 1.83 (m, 2H), 1.37 (t, 2H), 1.23 (m, 18H), 0.86 (m, 3H), 0.3 (s, 9H). ¹³C NMR (101 MHz, Chloroform-*d*) δ 153.0, 131.8, 129.6, 123.7, 116.7, 116.7, 110.9, 83.2, 80.0, 69.1, 31.8, 29.4, 29.3-29.4, 25.8, 22.6, 14.0.

2,5,8,11,14,17-hexakis((4-(dodecyloxy)phenyl)ethynyl)hexabenzob[bc,ef,hi,kl,no,qr]coronene (ParaHBC): To a mixture of **5** (250 mg, 0.195 mmol), CuI (12 mg, 0.06 mmol) and tetrakis(triphenylphosphine) palladium(0) (34

mg, 0.03 mmol) was added piperidine (20 mL) under nitrogen atmosphere. The mixture was degassed with three freeze-vacuum-thaw cycles. Then **8p** (0.683 g, 2.39 mmol) was added and the mixture was heated to 60 °C. After two hours more **8p** (0.2 g, 0.7 mmol) was added to the mixture. After the reaction completion (~24 hours), the mixture was cooled down to room temperature. The product was precipitated with HCl and washed with MeOH several times. The crude product was finally purified by column chromatography (chloroform) to yield of the desired product **ParaHBC** as yellow waxy solid with 39%.

2,5,8,11,14,17-hexakis((3-(dodecyloxy)phenyl)ethynyl)hexabenzob[bc,ef,hi,kl,no,qr]coronene (MetaHBC): To a mixture of **5** (250 mg, 0.195 mmol), CuI (12 mg, 0.06 mmol) and tetrakis(triphenylphosphine) palladium(0) (34 mg, 0.03 mmol) was added piperidine (20 mL) under nitrogen atmosphere. The mixture was degassed with three freeze-vacuum-thaw cycles. Then **7m** (0.7 g, 2.44 mmol) was added and the mixture was heated to 60 °C. After two hours more **8m** (0.2 g, 0.7 mmol) was added to the mixture. After the reaction completion (~24 hours), the mixture was cooled down to room temperature. The product was precipitated with HCl and washed with MeOH several times. The crude product was finally purified by column chromatography (chloroform) to yield of the desired product **MetaHBC** as yellow waxy solid with 32%.

Chapter 3

Supramolecular Organization and Charge Transport Properties of Hexa-*peri*-hexabenzocoronene Derivatives: Self-Assembly Molecular Nanowires in the Solid State

Abstract

This work investigated the relationship between the temperature-dependent supramolecular organization and charge transport dynamics of tailored hexa-*peri*-hexabenzocoronene (HBC) derivatives in the solid state. Both HBC isomers retained their liquid crystalline properties across all temperature ranges (from $-100\text{ }^{\circ}\text{C}$ to $>400\text{ }^{\circ}\text{C}$) with no clear isotropization temperature. Contrary to our hypothesis, strategically located alkoxy side chains on novel **MetaHBC** did not increase the columnar organization. Using the pulse-radiolysis time-resolved microwave conductivity (PR-TRMC) technique, the temperature-dependent charge carrier mobility was measured, and the hopping mechanism was present in both isomers. At room temperature, we achieved high mobilities for **ParaHBC** and **MetaHBC** of $0.135\text{ cm}^2/\text{Vs}$ and $0.062\text{ cm}^2/\text{Vs}$, respectively. Our preliminary studies suggest that optimizing solvent evaporation methods can play a vital role in intermolecular interaction, crystal orientation, supramolecular aggregation, and charge carrier mobilities. In future work, adding hydrogen bonding to the structure design might be necessary to achieve stronger interlocking.

3.1. Introduction

The aim of this chapter is to understand the impact of the nature of the solubilizing side chains on the charge carrier mobility of hexa-*peri*-hexabenzocoronene (HBC) derivatives in the solid state. We have varied the substitution position and have analyzed the effect of this on the supramolecular organization in the solid state. The aromatic core of the HBC is surrounded by flexible aliphatic chains, resulting in discotic liquid crystals (DLCs) that self-assemble into columnar mesophases through π - π stacking. DLCs create an efficient pathway for 1D charge carrier mobility along these columns.¹⁻³ HBC-based DLCs are highly sought after for the strong π - π interactions due to their large conjugated cores. The columnar phases have an extraordinarily high thermal stability, high columnar order⁴, and good self-assembly properties. It has been shown that very high 1D charge carrier mobilities can be achieved, up to 1.1 cm²/Vs in the solid state⁵, as measured by pulse-radiolysis time-resolved microwave conductivity (PR-TRMC).

Charge transport in organic semiconductors generally occurs via the thermally activated hopping mechanism. The rate of the individual hops, the charge transfer rate (ω) is a critical factor in achieving efficient charge transport. The higher the hopping rate, the faster the charge transport along the columns and the higher the corresponding charge carrier mobility. An estimate of the charge transfer rate can be obtained by Marcus theory (equation 1.3, Chapter 1), which expresses the charge transfer rate (ω) between two neighboring molecules in terms of two main parameters: the reorganization energy λ and the transfer integral J . As described in detail in Chapter 1, reorganization energy is strongly related to the geometric and electronic structure of the material. Typical values for the internal

reorganization energies of different sizes of conjugated cores are given in Table 3.1., which shows that λ typically decreases as the size of the conjugated core increases. Even a slight increase (0.2 eV) in the reorganization energy has been shown to reduce the charge carrier mobility by one order of magnitude.⁶ With its increased conjugated core size and smaller reorganization energy, the HBC core, is an excellent candidate for efficient charge transport.

Table 3.1. Internal reorganization energies of different sizes of polyaromatic hydrocarbon cores, calculated using quantum chemical calculations.⁶⁻⁹

Compound	λ, eV
Triphenylene	0.18
Anthracene	0.14
Coronene	0.13
Tetracene	0.11
Hexabenzocoronene (HBC)	0.1
Pentacene	0.09

The second key parameter, the charge transfer integral, is related to molecular overlap, but also to the position and exact orientation of the neighboring molecules. Density functional theory calculations have shown that the steric hindrance of the side chains usually results in a substantial 30° rotation of the neighboring HBC molecules, leading to a much smaller transfer integral than would be obtained at 0° angle. Although exact face-to-face stacking (0° or 60°) leads to the highest charge transfer integral (see

Figure 3.1.)¹⁰, this conformation is not favorable for substituted HBC molecules due to the strong steric hindrance of the side chains. However, even approaching a 0° rotational angle between two HBC molecules can dramatically increase the charge transfer integral, leading to higher values of the charge transfer rate and charge carrier mobility, especially since the charge transfer rate scales with the square of the charge transfer integral.

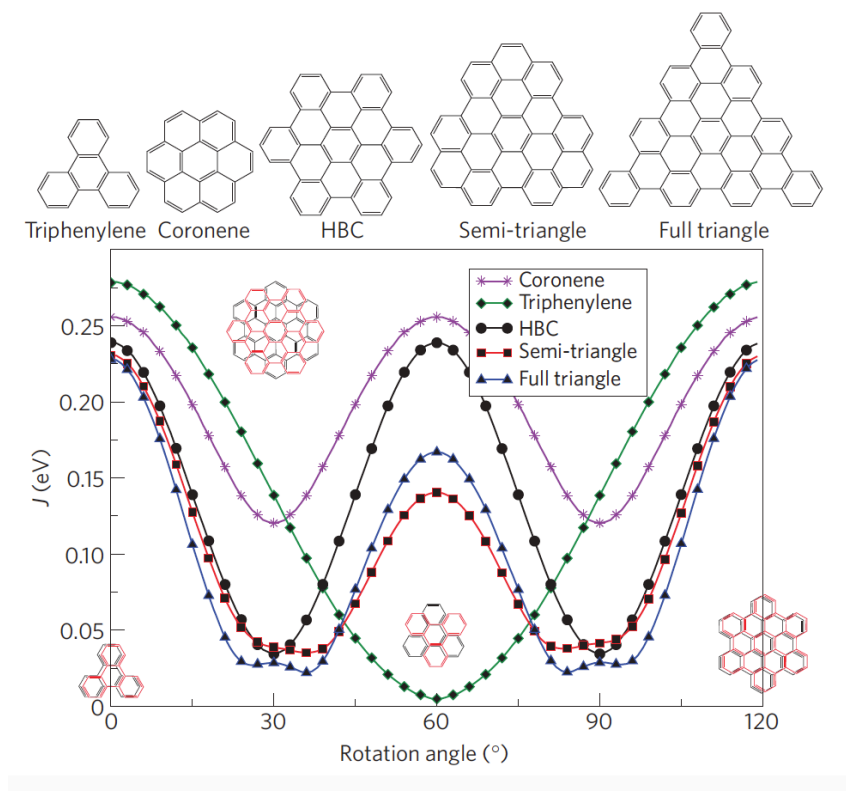


Figure 3.1. The absolute values of the charge transfer integral, J , of various symmetric polyaromatic hydrocarbon cores as a function of the rotational angle. The separation between the rigid core was fixed at 0.36 nm.¹⁰

Therefore, from a fundamental point of view, supramolecular order in mesophases is the crucial parameter for achieving efficient charge transport through self-assembled DLC columns. However, other criteria should be fulfilled when utilizing the liquid crystalline properties of desired molecules for device applications. The desired material should possess good solubility in a good solvent to allow easy processing, and the material should have a low clearing point to enable processing by thermal annealing. Moreover, the material with a low clearing point should be in its liquid crystalline phase at ambient or sub-ambient temperatures, and liquid crystalline mesophases should be thermally stable over an adequately broad temperature range.¹¹ However, with increased steric hindrances between side chains, i.e., branched or bulky substituents, the isotropic temperature decreases as the order of the molecules is reduced.¹¹ Therefore, tuning the thermotropic behavior and, thus, the mesophase characteristics is another crucial key in the design of DLCs.

The effects of various side chains on HBC molecules have been extensively studied, mainly by Müllen and coworkers.^{2,12,13} However, the impact of the steric aspects of the side-chain position on the solid state organization has not been deeply investigated. Using phenyl rings with alkoxy-solubilizing units located strategically in the *meta*-position instead of the commonly used *para*-position has not been studied to date. *Meta* position-substituted chains may occupy alternating positions between neighboring HBC molecules and reduce the steric hindrance. This may lead to yield lower rotational angles between neighboring stacked molecules and result in higher charge mobilities.

In this chapter, we study the solid-state properties of the unique *meta*-position substituted HBCs and compare them to the more common *para*-

position substitution on the HBC compounds for which the aggregation properties in solution were studied in Chapter 2. In both ParaHBC and MetaHBC derivatives (Figure 3.2.), bulky, rigid phenyl groups are attached to the aromatic HBC core, separated by an ethynyl spacer to allow a planar conformation. Introducing alkoxy side chains on different positions on the ring is expected to lead to different solid-state packings and, as a result, different charge carrier mobilities in the solid state.

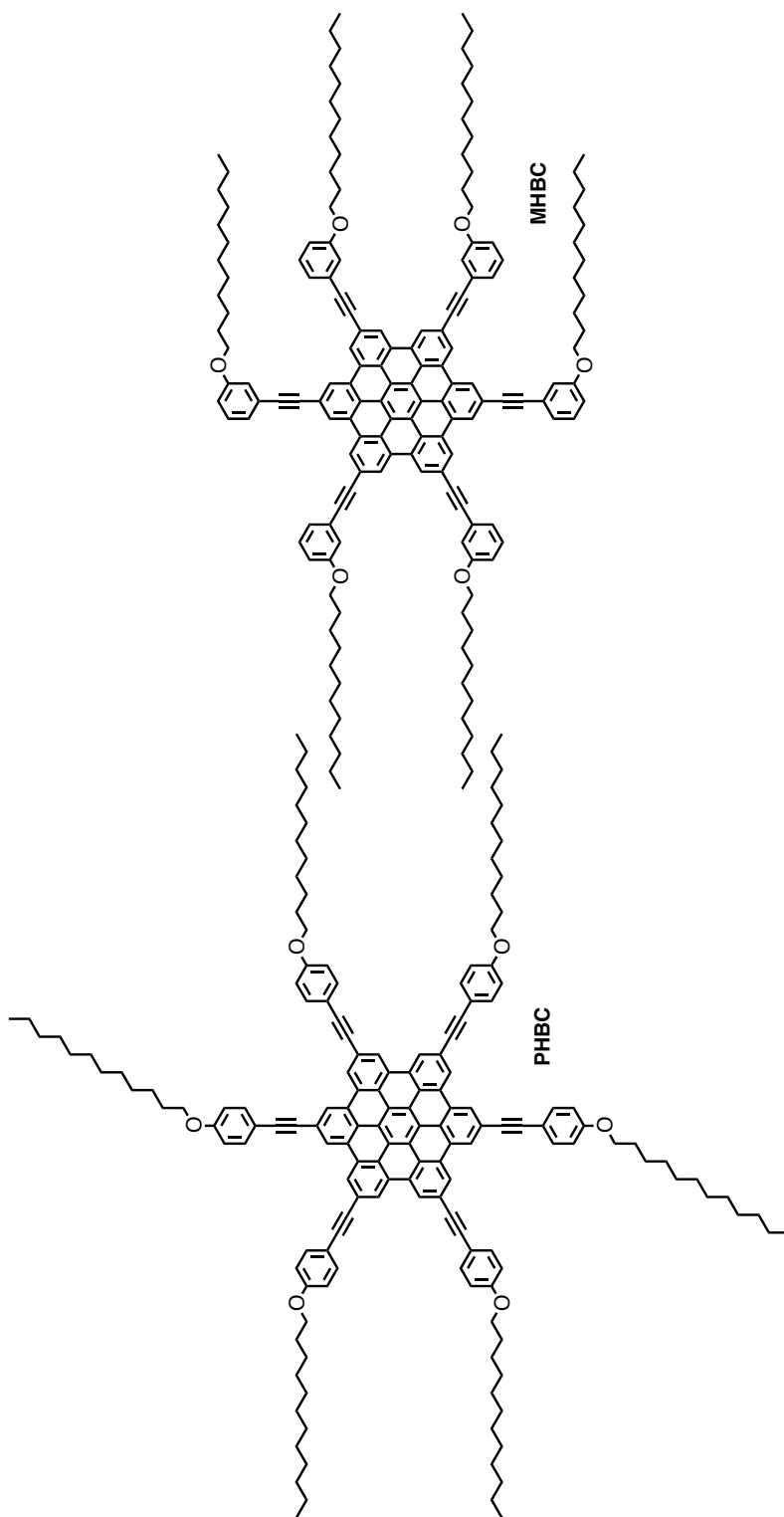


Figure 3.2. Chemical structure of **ParaHBC** and **MetaHBC**

3.2. Results & Discussion

In order to gain insight in the effect of the positioning of the side chains on the molecular packing and the charge transport properties, we have studied the thermotropic liquid crystalline (LC) behaviors of ParaHBC and MetaHBC in the solid state by differential scanning calorimetry (DSC), X-ray diffraction, and polarized optical microscopy (POM). The pulse-radiolysis time-resolved microwave conductivity (PR-TRMC) technique was used to measure charge carrier mobility.

3.2.1. DSC & POM

DSC was used to determine the thermotropic phase behavior of ParaHBC and MetaHBC from $-75\text{ }^{\circ}\text{C}$ to $200\text{ }^{\circ}\text{C}$ ($10\text{ }^{\circ}\text{C}/\text{min}$), while the mesophase characteristic textures were observed using POM from ambient temperature to $500\text{ }^{\circ}\text{C}$. These data give insight into the thermal stability of the mesophases and the transition enthalpies depending on the supramolecular organization of **ParaHBC** and **MetaHBC** in the solid state. As expected, the substitution position substantially influenced the thermal behavior and supramolecular order (Table 3.2).

Table 3.2. Thermal characterization of ParaHBC and MetaHBC

		Phase	T [°C] (ΔH°) [J·g ⁻¹]	Phase	T [°C] (ΔH°) [J·g ⁻¹]	Phase	T [°C] (ΔH°) [J·g ⁻¹]	Phase
ParaHBC	Heating	Col ₁	-3.4 (2.19)	Col ₂	19.7 (0.51)			
						Col ₃		
	Cooling	Col ₄	1.5 (-3.40)		-			
MetaHBC	Heating	Col ₁	8.7 (2.31)	Col ₂	39.7 (14.31)		154.7 (-4.17)	
						N _{col}		
	Cooling	Col ₃	3.5 (-7.03)		-		-	

The DSC curve of **ParaHBC** (Figure 3.3) exhibits two broad endothermic peaks at -3.4 and 19.7 °C with transition enthalpies of 2.19 and 0.51 J/g, respectively. Based on the POM analysis, the DSC peak at -3.4 °C was assigned to the LC to LC phase transition (Col₁→ Col₂), whereas the peak at 19.7 °C is attributed to the Col₂→Col₃ phase transition. **ParaHBC** showed a consistent texture starting from the ambient temperature to 500 °C, suggesting that **ParaHBC** is in an LC phase at room temperature and remains in the columnar phase without any observed clearing temperature. Around 500 °C, the textures observed by POM demonstrated cross-linking, which might be due to triple bonds in the molecular structure. However, on cooling to room temperature, **ParaHBC** revealed only one phase transition, directly from Col₃ to Col₁ or a different positional ordered columnar LC phase, Col₄, at 1.5 °C.

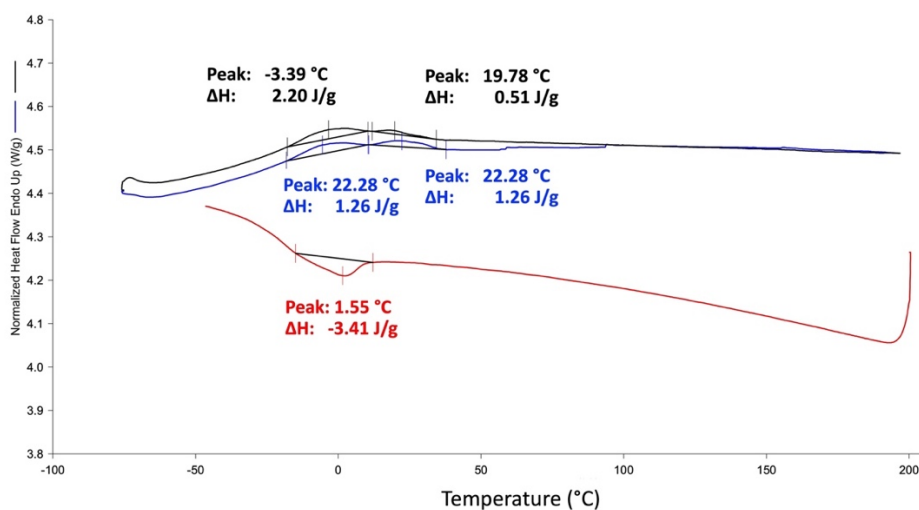


Figure 3.3. Differential Scanning Calorimetry analysis of ParaHBC

In contrast to *para*-position substitution (**ParaHBC**), *meta*-position substitution (**MetaHBC**) yielded a much wider variety of LC phases (Figure 3.4). **MetaHBC** also showed two endothermic peaks at slightly higher temperatures, around 8.7 and 39.7 °C. A broad endothermic peak at 8.7 °C is assigned to an LC to LC phase transition ($Col_1 \rightarrow Col_2$). Upon heating, **MetaHBC** transformed into nematic phase (N) at 39.7 °C with substantially higher enthalpy changes, as shown by the colorimetric changes observed in POM. On further heating, **MetaHBC** showed an additional exothermic peak at 154.7 °C. The textures observed using POM showed that chemical degradation or cross-linking might have started in **MetaHBC** around this temperature. On further heating, the less ordered **MetaHBC** remained in the N_{col} phase until 350 °C, where it either cross-linked through acetylene linkages between the core and the side chains or chemically degraded. On cooling, similar to **ParaHBC**, only one sharp

exothermic phase transition was observed at 3.5 °C. The textures revealed that **MetaHBC** showed a phase transition directly from N to Col₃ during the cooling process.

Interestingly, on the second heating, the DSC curves of **MetaHBC** displayed only one phase transition arising at 16.75 °C with a relatively large transition enthalpy value of 10.02 J/g. The textures observed using POM show that the **MetaHBC** soft solid transforms into a more ordered columnar phase rather than a columnar nematic phase. As for most HBCs, **ParaHBC** and **MetaHBC** do not exhibit clearing point up to 400 °C due to strong π - π stacking interactions between the aromatic cores in the mesophases.

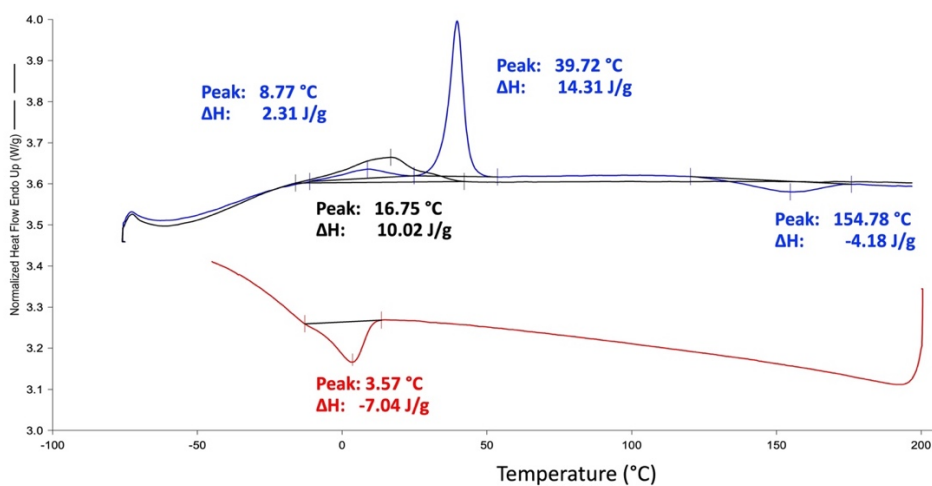


Figure 3.4. Differential Scanning Calorimetry analysis of MetaHBC

3.2.2. X-ray diffraction (XRD)

More information on the supramolecular arrangement of **MetaHBC** and **ParaHBC** in the solid state has been obtained from powder X-ray diffraction (XRD) at room temperature, as shown in Figure 3.5. Consistent with the DSC and POM studies, **ParaHBC** has a phase transition from a soft crystal to a columnar LC phase around 20 °C. The XRD patterns of **ParaHBC** contained a set of reflections in the low- and high-angle regions, indicative of a long-range, highly ordered two-dimensional (2D) hexagonal lattice of cylindrical columns (Col_{ho}).¹⁴ Detailed quantitative low-angle region peak analysis could not be conducted due to instrumental limitations. Accordingly, the intercolumnar distance of **ParaHBC** and **MetaHBC** could not be calculated. The sharp peaks assigned to (110) and (200) reflections might instead be assigned to the hexagonal structure of the columnar discotic phase for **ParaHBC**.^{15,16}

In the mid- and high-angle regions, the XRD patterns showed additional reflections, specifically, doublet reflections, which correspond to a distance possessing positional order. These doublet reflections are a signature of the columnar plastic phase.^{17,18} The first broad peak centered around 22° is typically observed for DLC. This peak was assigned to the lateral distance (d) between the molten side chains and was calculated as 4.5 Å using Bragg's Law.¹² The second peak, around 30°, was assigned to the (001) reflection, or the lattice parameter c , and corresponds to the intracolumnar distance between neighboring cores in the columnar stacks. The intracolumnar distance, c , was 3.45 Å for **ParaHBC** and 3.52 Å for **MetaHBC**. The presence of this peak indicates a certain degree of order along both **ParaHBC** and **MetaHBC** columns. The corresponding structure is likely to be a hexagonal column ordered mesophase, with a mean intra-columnar stacking distance close to 3.5 Å.¹⁹

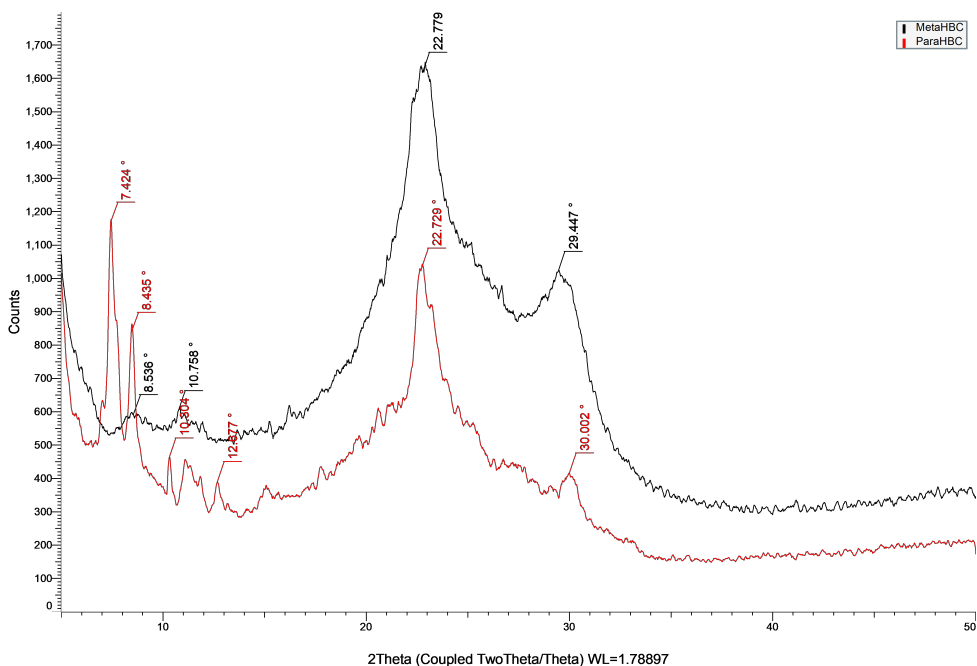


Figure 3.5. Powder X-ray diffraction patterns of **ParaHBC** (red) and **MetaHBC** (black) in the columnar plastic crystalline phase at room temperature.

3.2.3. PR-TRMC

In order to gain insight in the charge transport properties of the HBC compounds PR-TRMC measurements were performed in a temperature range between $-100\text{ }^{\circ}\text{C}$ and $+100\text{ }^{\circ}\text{C}$, starting from room temperature ($22\text{ }^{\circ}\text{C}$). From the end-of-pulse conductivity, the sum of the intracolumnar charge carrier mobilities, $\Sigma\mu_{1D}$, was derived as a function of temperature (see Equation 1.10, Chapter 1).

For **ParaHBC**, a room temperature value of $0.135\text{ cm}^2/\text{Vs}$ was derived for μ_{1D} , as shown in Figure 4.6. On cooling, an almost negligible

increase in mobility was observed at the LC-LC phase transition ($\text{Col}_2 \rightarrow \text{Col}_1$) around $-10\text{ }^\circ\text{C}$, resulting in a value of $0.139\text{ cm}^2/\text{Vs}$. As observed in the DSC studies, no evidence of recrystallization was found down to $-75\text{ }^\circ\text{C}$, and upon further cooling, the charge carrier mobility was found to decrease to $0.11\text{ cm}^2/\text{Vs}$ at $-100\text{ }^\circ\text{C}$, consistent with a thermally activated hopping mechanism. After heating to room temperature, the charge carrier mobility decreased by a factor of approximately 2.5 to $0.056\text{ cm}^2/\text{Vs}$. On heating, **ParaHBC** entered the $\text{Col}_2 \rightarrow \text{Col}_3$ mesophase transition slightly above room temperature, and the charge carrier mobility dropped to $0.029\text{ cm}^2/\text{Vs}$ due to increased freedom of motion and hence greater (dynamic) structural disorder due to the “melting” of peripheral side chains.²⁰ When **ParaHBC** was cooled to room temperature from $+100\text{ }^\circ\text{C}$, the charge carrier mobility ($0.024\text{ cm}^2/\text{Vs}$) did not recover and the final value was a factor of almost 6 lower than the initial value at room temperature. This shows that irreversible structural changes occur on heating, which can only be reversed on re-precipitation from solution.

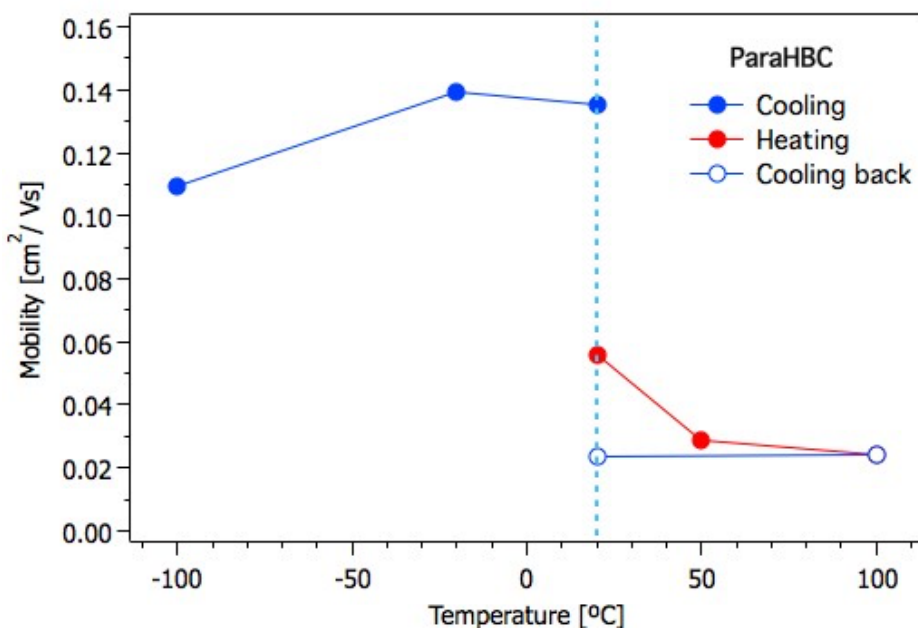


Figure 3.6. Temperature dependence of intracolumnar mobilities, μ_{1D} , for **ParaHBC** with varying phase transition behaviors upon cooling (filled blue dots), heating (filled red dots), and cooling to room temperature (unfilled blue dots).

PR-TRMC measurements on **MetaHBC** (Figure 3.7) show a room temperature mobility of $\mu_{1D} = 0.06 \text{ cm}^2/\text{Vs}$. On cooling, the mobility decreases monotonically as typically observed for DLCs and other organic semiconductors.²¹ On heating from room temperature, **MetaHBC** goes through the $\text{Col}_2 \rightarrow \text{N}$ phase transition at around $50 \text{ }^\circ\text{C}$ as observed in the DSC and POM measurements. A dramatic decrease in the charge carrier mobility to $0.042 \text{ cm}^2/\text{Vs}$ (at $+100 \text{ }^\circ\text{C}$) occurred, as the structural disorder in the nematic phase is much higher than in the columnar phase, with some orientational order but no positional order.²² Following cooling to room

temperature the initial columnar structure did not recover and the initial room temperature mobility was not reached. The final charge carrier mobility of **MetaHBC** was measured to be $0.03 \text{ cm}^2/\text{Vs}$ at room temperature, which is almost the same as for **ParaHBC** after cooling and heating cycles.

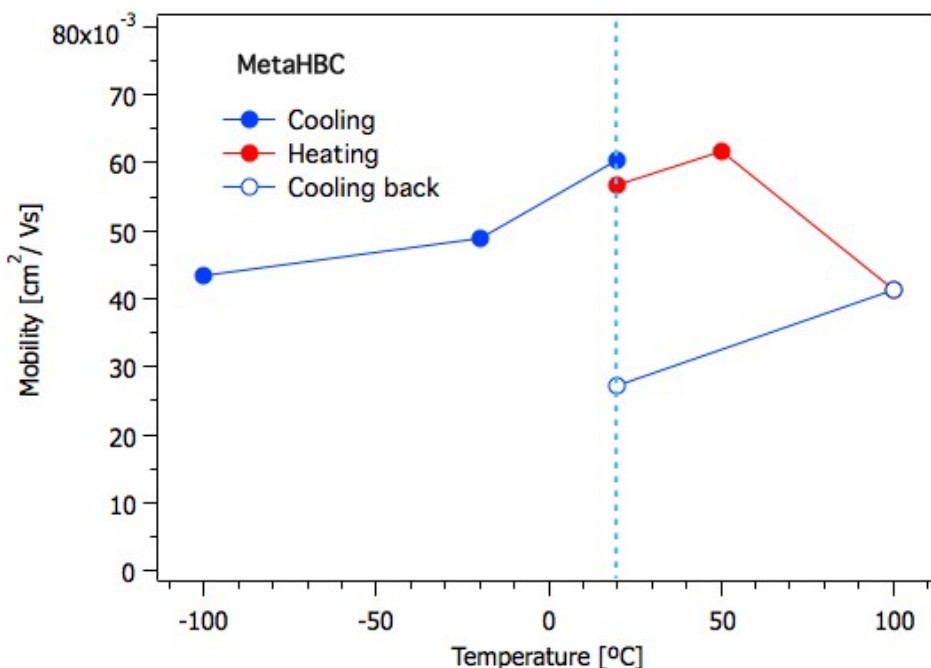


Figure 3.7. Temperature dependence of intracolumnar mobilities, μ_{ID} , for **MetaHBC** with varying phase transition behaviors upon cooling (filled blue dots), heating (unfilled red dots), and cooling back to room temperature (unfilled blue dots) cycles.

3.3. Conclusions

In this chapter we have examined the effect of the nature of the side chain on the solid state organization and charge transport properties of HBC derivatives. The introduction of alkoxy side chains on a unique *meta*-position (3-alkoxy phenyl) compared to the well-studied *para*-position (4-alkoxy phenyl) to the HBC core via acetylene linkage in principle allows controlling the thermal behavior and supramolecular organization of the different mesophases. We found that both HBC derivatives exhibit LC properties from low ($-100\text{ }^{\circ}\text{C}$) to high ($>400\text{ }^{\circ}\text{C}$) temperatures with no clear isotropization temperature. **ParaHBC** exhibits a plastic crystalline phase at sub-ambient temperatures and a thermally stable ordered columnar phase starting with ambient temperature. In addition to ordered columnar supramolecular structures in the solid state, **ParaHBC** demonstrated a charge carrier mobility of $0.135\text{ cm}^2/\text{Vs}$ at room temperature. However, the charge carrier mobility drops abruptly on heating and does not recover into the higher-mobility organization on cooling back to room temperature. While the initial room temperature mobility is promising, the solid state processing and possible self-healing properties pose significant problems for application in devices.

For **MetaHBC** a similar columnar liquid crystalline order was observed at room temperature, while a nematic columnar phase is obtained at elevated temperatures. **MetaHBC** showed a charge carrier mobility of $0.06\text{ cm}^2/\text{Vs}$ at room temperature, less than half of the charge carrier mobility measured in **ParaHBC**. This reduction is likely to be due to a decrease in a long-range order. Also for **MetaHBC** the initial solid state ordering with high mobility is not recovered on cooling for the high-temperature phase. These preliminary studies show that the solid state order critically depends on the preparation procedures, including

recrystallization either from solution or melt. This indicates that a more detailed study into the precipitation and aggregation behavior of **ParaHBC** and **MetaHBC** may be needed to examine the initial hypothesis that MetaHBC may organize with a smaller rotation angle between neighboring molecules.

3.4. References

1. Sergeyev, S., Pisula, W. & Geerts, Y. H. Discotic liquid crystals: A new generation of organic semiconductors. *Chem Soc Rev* **36**, 1902–1929 (2007).
2. Kumar, M. & Kumar, S. Liquid crystals in photovoltaics: A new generation of organic photovoltaics. *Polym J* **49**, 85–111 (2017).
3. Wöhrle, T. *et al.* Discotic Liquid Crystals. *Chem Rev* **116**, 1139–1241 (2016).
4. Wu, J., Watson, M. D., Zhang, L., Wang, Z. & Müllen, K. Hexakis(4-iodophenyl)-peri-hexabenzocoronene- A Versatile Building Block for Highly Ordered Discotic Liquid Crystalline Materials. *J Am Chem Soc* **126**, 177–186 (2004).
5. Craats, A. M. van de *et al.* Record Charge Carrier Mobility in a Room-Temperature Discotic Liquid-Crystalline Derivative of Hexabenzocoronene. *Advanced Materials* **11**, 1469–1472 (1999).
6. Lemaur, V. *et al.* Charge Transport Properties in Discotic Liquid Crystals: A Quantum-Chemical Insight into Structure–Property Relationships. *J Am Chem Soc* **126**, 3271–3279 (2004).
7. Andrienko, D., Kirkpatrick, J., Marcon, V., Nelson, J. & Kremer, K. Structure–charge mobility relation for hexabenzocoronene derivatives. *physica status solidi (b)* **245**, 830–834 (2008).
8. Coropceanu, V. *et al.* Hole- and Electron-Vibrational Couplings in Oligoacene Crystals: Intramolecular Contributions. *Phys Rev Lett* **89**, 275503 (2002).

9. Troisi, A. Charge dynamics through pi-stacked arrays of conjugated molecules: effect of dynamic disorder in different transport/transfer regimes. *Mol Simul* **32**, 707–716 (2006).
10. Feng, X. *et al.* Towards high charge-carrier mobilities by rational design of the shape and periphery of discotics. *Nat Mater* **8**, 421–426 (2009).
11. Sergeyev, S., Pisula, W. & Geerts, Y. H. Discotic liquid crystals: A new generation of organic semiconductors. *Chem Soc Rev* **36**, 1902–1929 (2007).
12. Laschat, S. *et al.* Discotic liquid crystals: From tailor-made synthesis to plastic electronics. *Angewandte Chemie - International Edition* **46**, 4832–4887 (2007).
13. Seyler, H., Purushothaman, B., Jones, D. J., Holmes, A. B. & Wong, W. W. H. Hexa-peri-hexabenzocoronene in organic electronics. *Pure and Applied Chemistry* **84**, 1047–1067 (2012).
14. Alameddine, B. *et al.* Influence of linear and branched perfluoroalkylated side chains on the π - π stacking behaviour of hexa-peri-hexabenzocoronene and thermotropic properties. *Supramol Chem* **26**, 125–137 (2014).
15. Herwig, P., Kayser, C. W., Müllen, K. & Spiess, H. W. Columnar mesophases of alkylated hexa-peri-hexabenzocoronenes with remarkably large phase widths. *Advanced Materials* **8**, 510–513 (1996).
16. Palmans, A. R. A., Vekemans, J. A. J. M., Fischer, H., Hikmet, R. A. & Meijer, E. W. Extended-Core Discotic Liquid Crystals Based on the Intramolecular H-Bonding in N -Acylated 2,2'-Bipyridine-

- 3,3'-diamine Moieties. *Chemistry - A European Journal* **3**, 300–307 (1997).
17. Brand, R., Lunkenheimer, P. & Loidl, A. Relaxation dynamics in plastic crystals. *J Chem Phys* **116**, 10386–10401 (2002).
 18. Wang, Y., Zhang, C., Wu, H. & Pu, J. Synthesis and mesomorphism of triphenylene-based dimers with a highly ordered columnar plastic phase. *J Mater Chem C Mater* **2**, 1667 (2014).
 19. Pisula, W., Feng, X. & Müllen, K. Tuning the columnar organization of discotic polycyclic aromatic hydrocarbons. *Advanced Materials* **22**, 3634–3649 (2010).
 20. Warman, J. M. *et al.* Charge Mobilities in Organic Semiconducting Materials Determined by Pulse-Radiolysis Time-Resolved Microwave Conductivity: π -Bond-Conjugated Polymers versus π - π -Stacked Discotics. *Chemistry of Materials* **16**, 4600–4609 (2004).
 21. Debije, M. G. *et al.* The Optical and Charge Transport Properties of Discotic Materials with Large Aromatic Hydrocarbon Cores. *J Am Chem Soc* **126**, 4641–4645 (2004).
 22. Kouwer, P. H. J., Jager, W. F., Mijs, W. J. & Picken, S. J. Synthesis and Characterization of a Novel Liquid Crystalline Polymer Showing a Nematic Columnar to Nematic Discotic Phase Transition. *Macromolecules* **33**, 4336–4342 (2000).

Chapter 4

Charge Carrier Transport Properties of Symmetric Alkyl[1]Benzo[thieno[3,2-*B*][1]Benzo]thiophenes

Abstract

In this part of the thesis, we focus on the investigation of charge transport mechanism and comparison of series of rod-like liquid crystalline alkyl[1]benzo[thieno[3,2-*b*][1]benzo]thiophene derivatives with varying side chain lengths in solid-state by using temperature-dependent pulse radiolysis time-resolved microwave conductivity technique. All C_n -BTBT- C_n ($n= 8, 10, 12$) derivatives exhibit herringbone packing motifs that results in 2D lamellar structure for charge transport. The conductivity measurements show that all derivatives exhibit remarkably high intrinsic charge carrier mobilities at room temperature, as consistent with values reported previously. However, at lower temperatures (down to $-100\text{ }^\circ\text{C}$) the significant decrease in decay kinetics and charge carrier mobility is observed, strengthened the argument for a thermally activated hopping model as the primary mechanism for charge transport in C_n -BTBT- C_n derivatives in solid state.

4.1. Introduction

Organic semiconductors have attracted a large amount of interest over the last decades as a promising alternative to inorganic semiconductors due to their tunability, solution processability, and mechanical flexibility, allowing for low-cost, large-area, and lightweight fabrication techniques.¹ However, the exact mechanism of charge carrier transport in these materials is not clear in all cases. A clear understanding of transport mechanisms is of fundamental academic interest and crucial to optimize the transport properties for specific applications. In particular, efficient charge transport is important for device speed, reduced power loss, and higher efficiency can be achieved in promising devices such as organic light-emitting diodes (OLEDs), displays, organic field-effect transistors (OFETs), integrated circuits, or organic photovoltaics (OPVs).^{2,3}

The key quantity that characterizes charge transport in organic semiconductors is the mobility of charge carriers (electrons and/or holes). Important parameters that influence the charge transport mechanisms in π -conjugated materials include the crystalline organization, disorder, the purity of the molecule, defects, traps, temperature, charge-carrier density, molecular size & weight, electric fields, and pressure.⁴ These important characteristics can lead to significant differences in the measured charge carrier mobility. A more detailed review of charge carrier transport models can be found in Chapter 1.

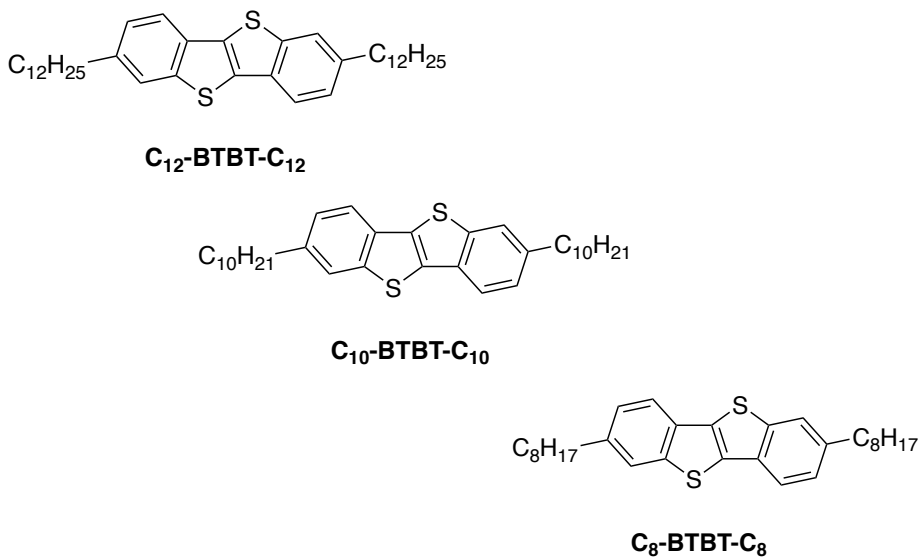


Figure 4.1. Chemical structures of 2,7-didodecyl-BTBT (C₁₂-BTBT-C₁₂), 2,7-didecyl-BTBT (C₁₀-BTBT-C₁₀), and 2,7-dioctyl-BTBT (C₈-BTBT-C₈)

The demand to increase the charge carrier mobility of organic semiconductors and to understand the charge transport mechanisms in these materials have motivated scientists to synthetically, experimentally, and theoretically explore the relationship between mobility and molecular structure on the molecular and mesoscopic scale. Among rod-like liquid crystals, [1]benzothieno[3,2-b][1]benzothiophene (BTBT) derivatives with alkyl side chains of varying length have attracted a significant amount of attention due to their high charge carrier mobility, which exceeds 10 cm²/Vs, the viability of their synthetic route, and their superior ambient stability.⁵⁻¹¹ Although the results from charge carrier mobility measurement have been promising, some of the values reported suffer from overestimation and/or reproducibility, especially in the context of OFET applications.^{12,13}

In this Chapter, we investigate the charge carrier mobility and charge transport mechanism of C_n -BTBT- C_n isomers ($n = 8, 10, 12$) (Figure 4.1) by using the unique PR-TRMC technique. This technique aims to determine the charge carrier mobility in bulk-state BTBT isomers as a function of temperature.

4.2. Results & Discussion

4.2.1. DSC & POM

The chemical structures and synthetic procedures of the symmetrical C_n -BTBT- C_n series ($n = 8, 10, 12$) of interest have previously been reported by Geerts et al.^{8,14,15} In addition to synthetic studies, the effect of substituted side chains on the molecular organization and charge transport characteristics of these materials at room temperature have also been reported by various research groups, both theoretically and experimentally.¹⁶⁻¹⁸ In particular, the temperature-dependent microscopic and macroscopic properties of these thermotropic rod-like liquid crystals must be known in detail to draw clear links between their structural properties and their charge transport characteristics.

The thermal behavior of the different symmetrical C_n -BTBT- C_n compounds, which have several characteristics in common due to the presence of their linear alkyl chains ($n = 8, 10, 12$), are summarized in Table 4.1. The DSC traces and POM textures showed that all derivatives are in a Cr phase at room temperature. Around 110 °C, all derivatives undergo a phase transition from the Cr phase to a low-ordered liquid crystalline SmA phase. Upon further heating, C₈-BTBT-C₈, C₁₀-BTBT-

C₁₀, and C₁₂-BTBT-C₁₂ melt at relatively low temperatures (126.4, 124.2, and 118.4°C, respectively).¹⁸ It should be noted that lowering the molecular order of the material during the transition from the Cr phase to the SmA phase at a low clearing point (I) results in lower thermal durabilities.⁵ The charge carrier mobility of fabricated crystalline C₁₀-BTBT-C₁₀ films for OFET applications has been shown to decrease dramatically after being subjected to thermal stresses above 100°C for 5 min. At this temperature, the C₁₀-BTBT-C₁₀ derivative is in the less-ordered SmA phase and melts into droplets, exhibiting poor film uniformity and a rough surface morphology.¹⁹

Table 4.1. The thermal transition temperatures of C₈-BTBT-C₈, C₁₀-BTBT-C₁₀, and C₁₂-BTBT-C₁₂ derivatives based on DSC analysis.

Compound	T _{Cr → T_{SmA}} [°C]	T _{SmA → T_I} [°C]
C₁₂-BTBT-C₁₂	111.1	118.4
C₁₀-BTBT-C₁₀	112.2	124.2
C₈-BTBT-C₈	110.1	126.4

Cr: crystalline phase; SmA: smectic A phase; I: isotropic phase

4.2.2. XRD

It is important to determine the molecular organization of the material and its temperature dependence to link the charge transport properties to the supramolecular organization. Izawa¹⁸ previously reported the crystalline structure of the C_n -BTBT- C_n series ($n = 8, 10, 12$). Thin films of these compounds exhibit a well-ordered single-crystalline structure, as observed by XRD measurements in bulk material at room temperature.^{18,20,21} The XRD pattern of C_n -BTBT- C_n bulk samples at room temperature exhibit a series of peaks that can be attributed to (00 l) reflections, indicating a long-range lamellar structural order. The interlayer distance (spacing) along the c -axis calculated from the primary (001) reflection was found to be 29.0, 33.3, and 37.5 Å for C_8 -BTBT- C_8 , C_{10} -BTBT- C_{10} , and C_{12} -BTBT- C_{12} respectively.¹⁷ The intermolecular stacking distance of the 2,7-dialkyl derivatives (C_n -BTBT- C_n , $n = 8, 10, 12$) slightly decreased as the chain length of the alkyl groups increased.²² This can be explained by the ‘zipper effect’ exhibited by long alkyl chains due to increased intermolecular van der Waals interactions, which tighten the molecular packing in the solid state.^{23,24} Regardless of slight differences between the interlayer and intermolecular distances, similar molecular packing structures with a herringbone motif were found, with no evidence of the interdigitation of the linear alkyl chains. Consequently, the Cr phase is monoclinic for all three compounds, with the same $P2_1/a$ space group. It consists of a lamellar arrangement of C_8 -BTBT- C_8 , C_{10} -BTBT- C_{10} , and C_{12} -BTBT- C_{12} molecules that are self-organized with a herringbone packing motif, resulting in the 2D pathway for charge transport as presented in Figure 4.2.

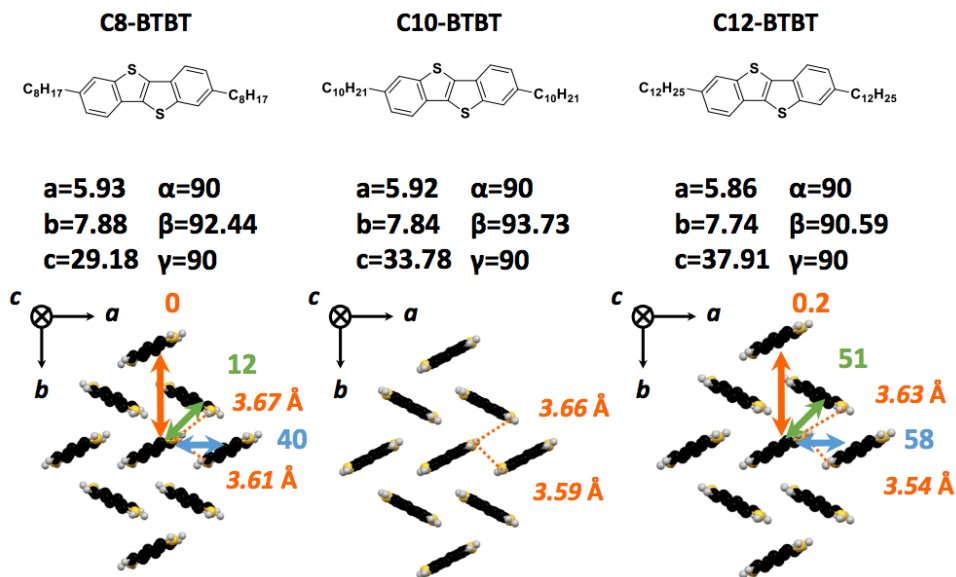
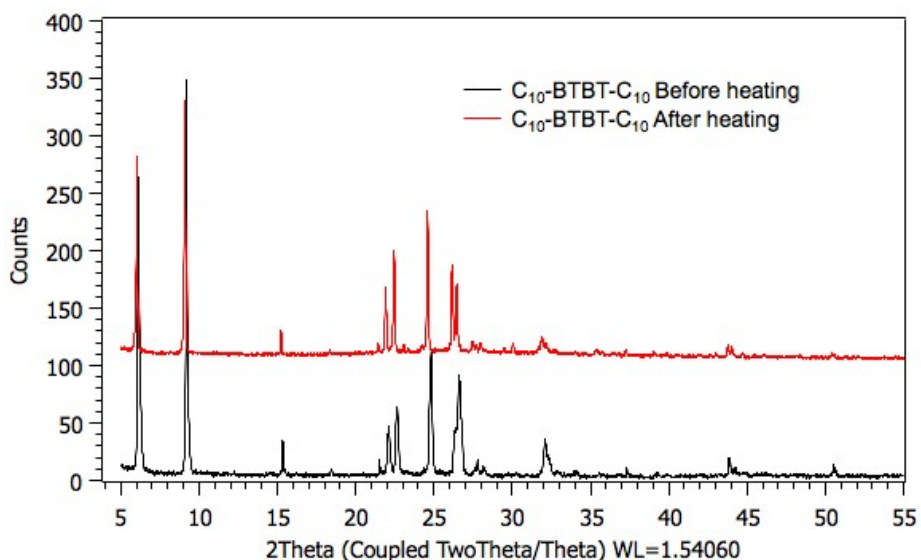
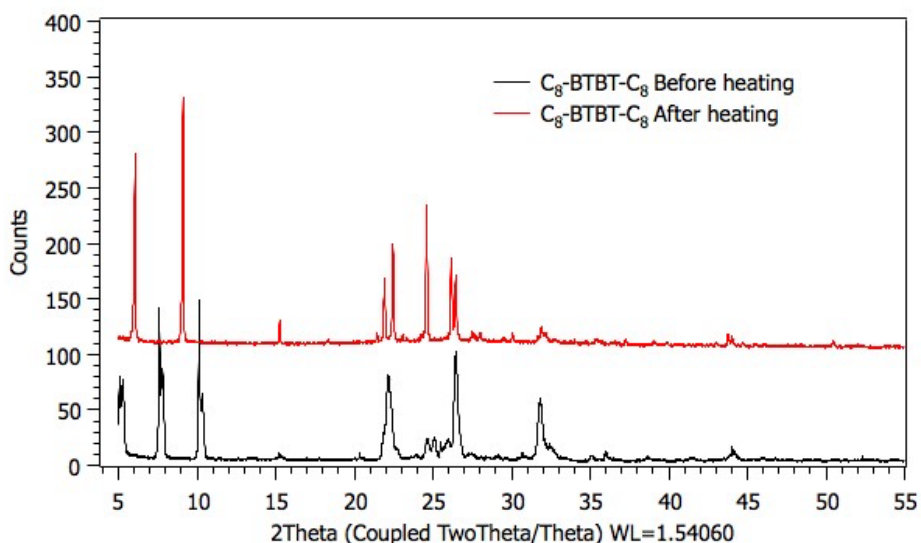


Figure 4.2. The molecular arrangement of BTBTs for J.

As expected, the temperature-dependent XRD analysis reveals that the C_n -BTBT- C_n series exhibits mesophase transitions upon heating and cooling. Figure 4.3 shows that, at room temperature before and after thermal stress (heated to above its melting temperature of $\sim 120^\circ\text{C}$ for 1 min), all molecules were confirmed to be arranged in ordered crystalline structures, as evident from sharp diffraction peaks with high intensities. However, as a result of thermal stress, changes in the position and intensity of XRD peaks are observed in all BTBT materials after they were cooled back down to room temperature from the isotropic phase. Several small-angle X-ray peaks of C_8 -BTBT- C_8 slightly shifted to lower values, indicating that the interlayer distance between these molecules increased after thermal stress. While C_{10} -BTBT- C_{10} did not exhibit any observable shifts at small angles, the change in the high-angle peaks ($18^\circ < 2\theta$) to lower values with decreased intensities indicate a change in the ordering

and crystallinity of the material. For C_{12} -BTBT- C_{12} similar changes are seen as in C_{10} -BTBT- C_{10} . This XRD analysis shows that while ordered structures are recovered after heating to the isotropic phases, clear changes in the supramolecular order and crystallinity of the samples occur that may have an effect on the charge transport properties.



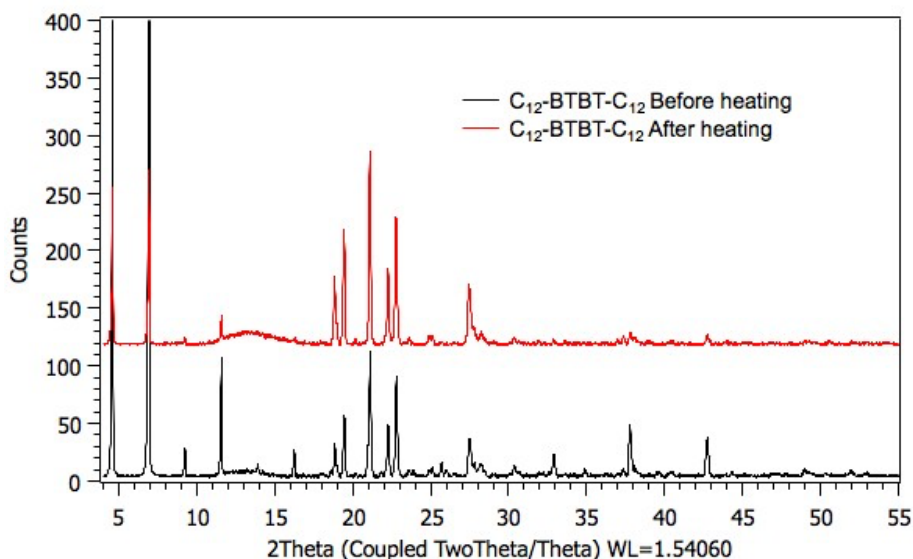


Figure 4.3. XRD analysis of the C_n -BTBT- C_n compounds before and after heating to the isotropic phase.

4.2.3. Temperature-dependent PR-TRMC Studies

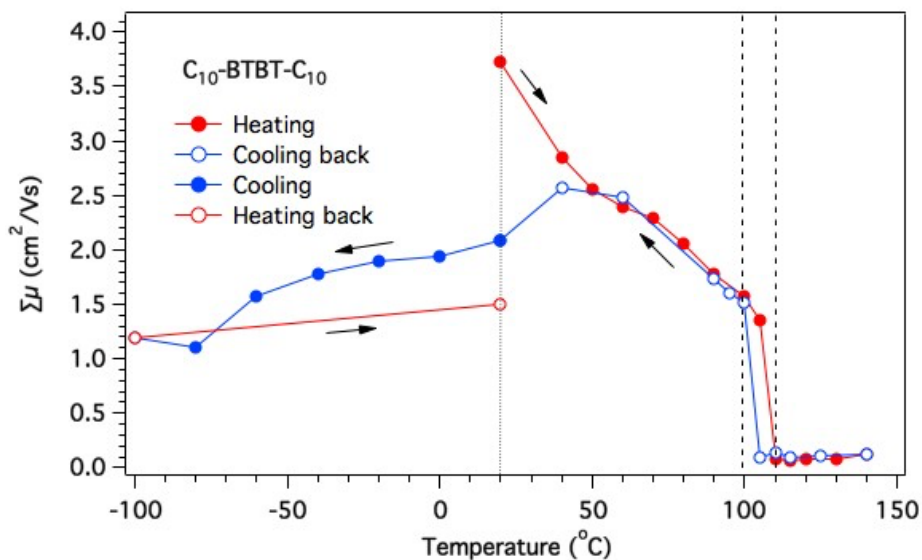
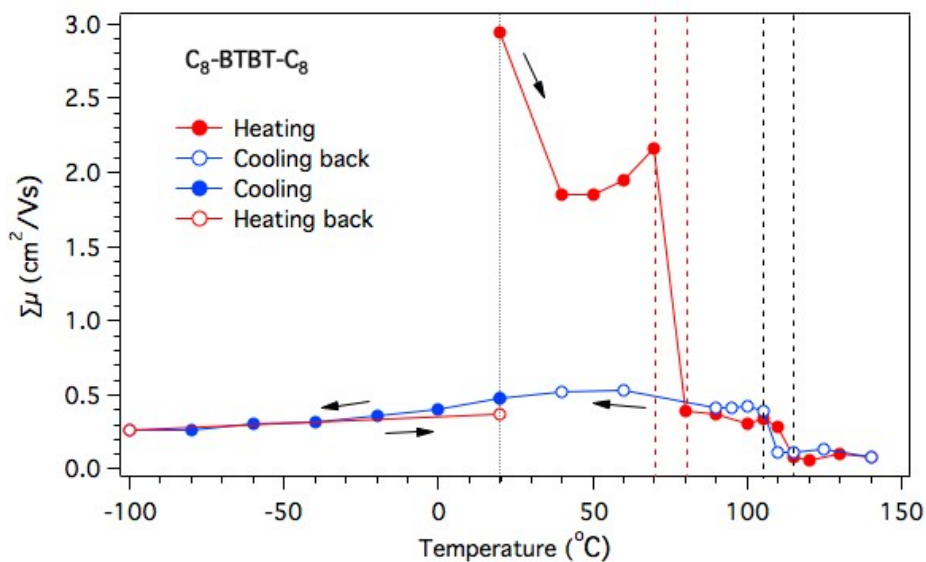
To determine the charge transport properties of the C_n -BTBT- C_n ($n = 8, 10, 12$) derivatives, we studied the temperature dependence of the charge carrier mobility using the PR-TRMC technique described in Chapter 1. PR-TRMC measurements yield information about the charge carrier mobility that can be calculated from the end-of-pulse conductivity, but also on the decay of charge carrier by examining the conductivity as a function time. The latter gives insight in the recombination and trapping of charges.

The temperature-dependent charge carrier mobility of C_n -BTBT- C_n ($n = 8, 10, 12$) derivatives, measured by PR-TRMC (using a 1 ns pulse length) with the same heating and cooling cycles used for each sample (-

$100^{\circ}\text{C} \leq T_{\text{room}} \leq 140^{\circ}\text{C}$) are shown in Figure 4.4. At room temperature, all of the C_n -BTBT- C_n derivatives exhibit remarkably high one-dimensional charge carrier mobility (μ_{1D}) values at room temperature in the crystalline solid state. The values for C_n -BTBT- C_n ($n = 8, 10, 12$) were derived to be $2.94 \text{ cm}^2/\text{Vs}$, $3.02 \text{ cm}^2/\text{Vs}$, and $3.72 \text{ cm}^2/\text{Vs}$, respectively. These mobility values are consistent with values calculated using a thermally activated semi-classical Marcus rate theory calculations, as well as with mobility values derived from solution-processed OFET and OTFT measurements on the same C_n -BTBT- C_n ($n = 8, 10, 12$) derivatives.^{17,18,24-29}

The charge carrier mobility values for all C_n -BTBT- C_n ($n = 8, 10, 12$) samples decreases monotonically as the temperature is increased from room temperature. This is consistent with progressively increasing dynamic disorder in the solid state, leading to reduced mobility values. At around 105°C , all derivatives undergo the Cr \rightarrow SmA phase transition, followed immediately afterward by the SmA \rightarrow I phase transition, in which the molecules melted completely and exhibited their lowest charge carrier mobility values; these observations were consistent with DSC measurements. After the materials were cooled to room temperature, their μ_{1D} values increased due to recrystallization (SmA/I \rightarrow Cr) but, as observed in XRD measurements, none of the derivatives fully returned to their original highly ordered crystalline lattice (Figure 4.2). Consequently, the μ_{1D} of these materials at room temperature decreased by a factor of ~ 2 for both C_{10} -BTBT- C_{10} ($1.35 \text{ cm}^2/\text{Vs}$) and C_{12} -BTBT- C_{12} ($2.09 \text{ cm}^2/\text{Vs}$), while the decrease in μ_{1D} was found to be a factor of 6 for C_8 -BTBT- C_8 ($0.47 \text{ cm}^2/\text{Vs}$). The dramatic decrease in μ_{1D} may be due to the formation of a stable monolayer structure after cooling, instead of the well-ordered herringbone packing due to the rapid rate of cooling (minutes).³⁰ Upon

further cooling ($-100^{\circ}\text{C} \leq T_{\text{room}}$), the μ_{ID} of $\text{C}_8\text{-BTBT-C}_8$, $\text{C}_{10}\text{-BTBT-C}_{10}$, and $\text{C}_{12}\text{-BTBT-C}_{12}$ exhibited charge transports that appears to follow a thermally activated hopping model at low temperatures; this was in contrast reports in literature that some $\text{C}_n\text{-BTBT-C}_n$ derivatives exhibit band-like transport.^{10,24,31}



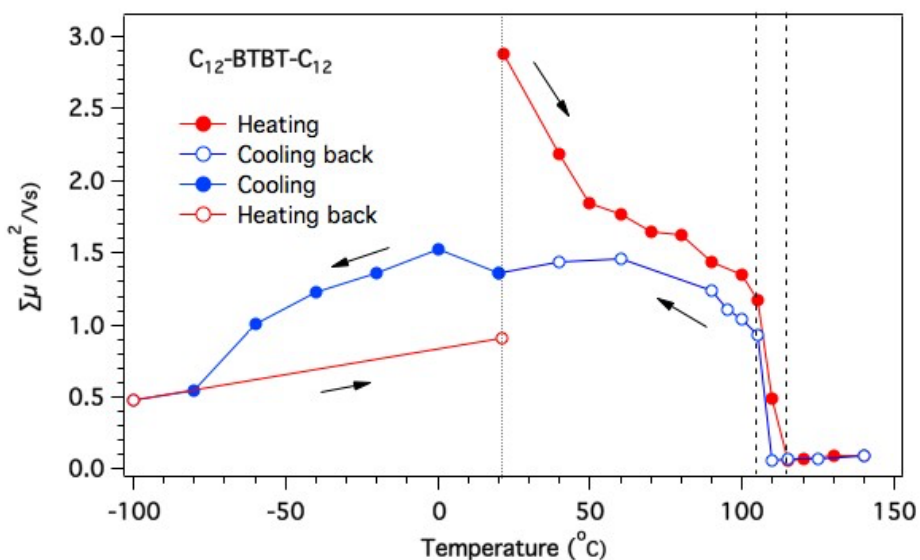


Figure 4.4. Temperature-dependent charge carrier mobilities for a) C_8 -BTBT- C_8 , b) C_{10} -BTBT- C_{10} , and c) C_{12} -BTBT- C_{12} upon heating and cooling, starting from room temperature. Room temperature is indicated by the small dashed lines, while the black dashed lines indicate the phase transition temperatures as calculated from DSC. The red dashed line in C_8 -BTBT- C_8 represents the temperature at which the unexplained charge carrier mobility decrease occurred.

In the measurements presented above the low temperature regime was examined for samples that were already cooled back from the isotropic phase. To confirm that the charge transport mechanism at low temperature follows a thermally activated hopping mechanism also for freshly precipitated materials, additional low temperature measurements were performed using freshly precipitated C_{12} -BTBT- C_{12} , see Figure 4.5. At room temperature, the freshly precipitated C_{12} -BTBT- C_{12} exhibits a high

μ_{1D} value of $3.25 \text{ cm}^2/\text{Vs}$, indicating that reprecipitation yields a similar mobility value as discussed above. The charge carrier mobility decreases upon cooling, confirming a hopping mechanism.³²

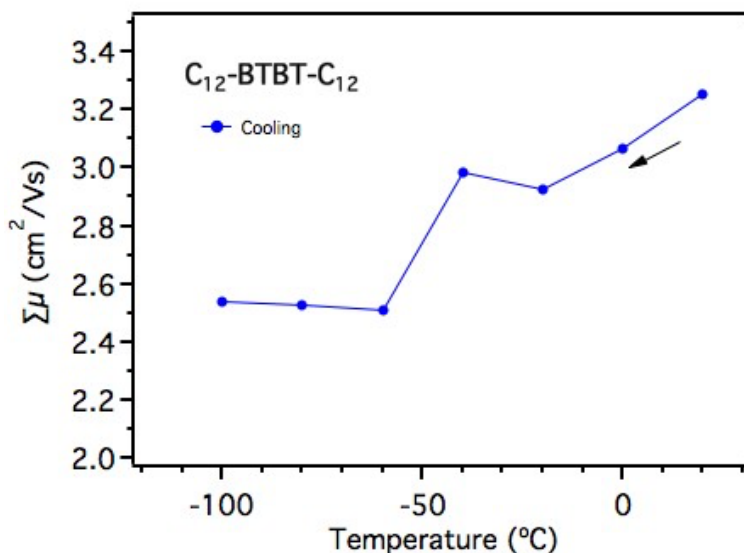
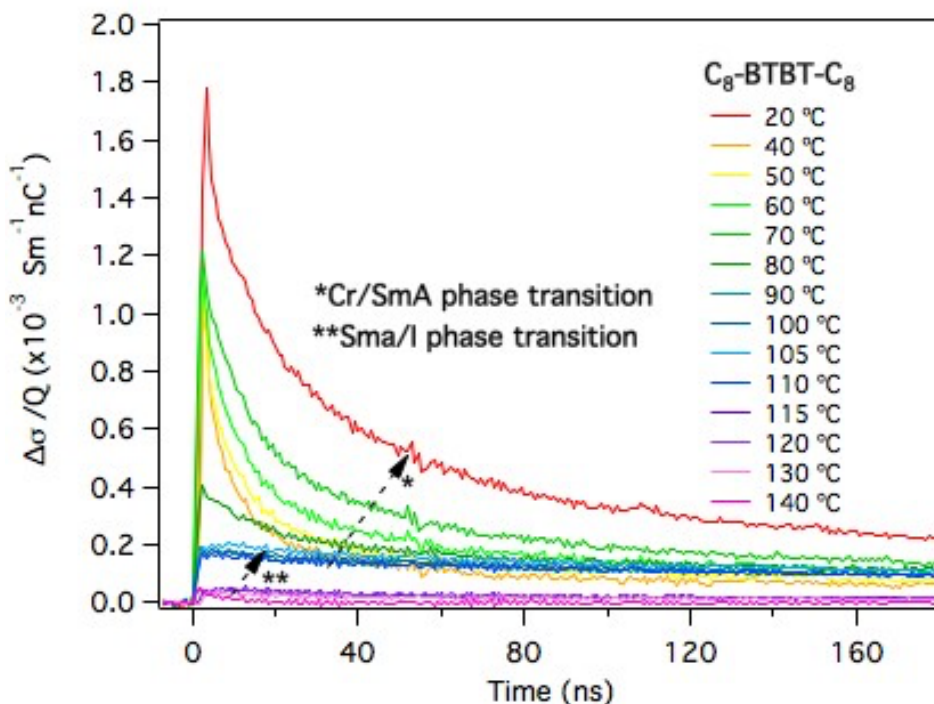


Figure 4.5. Low-temperature charge carrier mobility for freshly precipitated $\text{C}_{12}\text{-BTBT-C}_{12}$

4.2.4. Charge carrier decay kinetics

In Figure 4.6 the change in conductivity in the $\text{C}_{12}\text{-BTBT-C}_{12}$ upon irradiation is shown as a function of times to gain insight in the life-time and decay kinetics of charge carrier. A comparison of PR-TRMC conductivity transients for the different compounds at different temperatures reveals pronounced differences in the carrier lifetimes. As shown in Figure 4.6, the conductivity initially increases during the pulse as mobile charge carriers are generated. Due to charge recombination and/or trapping, the conductivity gradually decays after the pulse.

Upon heating ($T_{\text{room}} \leq 140^\circ\text{C}$), the conductivity of $\text{C}_{12}\text{-BTBT-C}_{12}$ gradually decreased and resulted in notably low conductivity after passing through the phase transitions at higher temperatures (Figure 4.6c). This decrease in conductivity is due to a disruption of the ordered structure within the material in its liquid crystalline state. Interestingly, the lifetime of the carriers becomes longer at higher temperature. A similar trend was observed in $\text{C}_{10}\text{-BTBT-C}_{10}$ and $\text{C}_8\text{-BTBT-C}_8$ (Figure 4.6). The unexpected conductivity (mobility) and increase in charge carrier lifetimes in $\text{C}_8\text{-BTBT-C}_8$ between $40\text{--}70^\circ\text{C}$ might indicate that the molecular order in the crystalline phase improved slightly. It is hard to explain the origin of these changes in the carrier lifetime without more detailed structural characterizations, however, it is clear that both the mobility of charges and their decay kinetic show a strong dependence on the subtle changes in the supramolecular order in the materials.



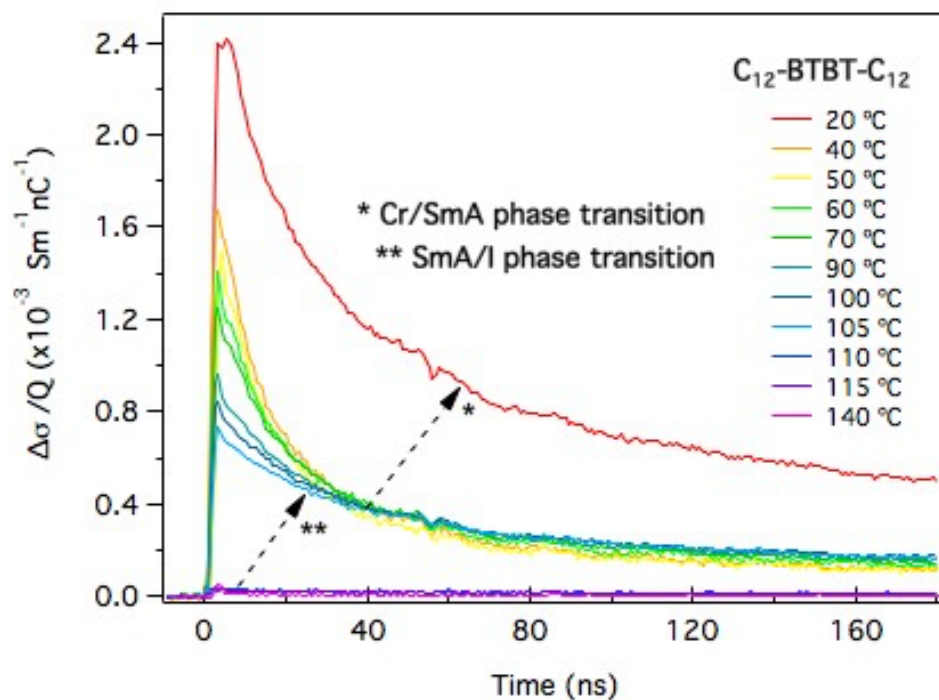
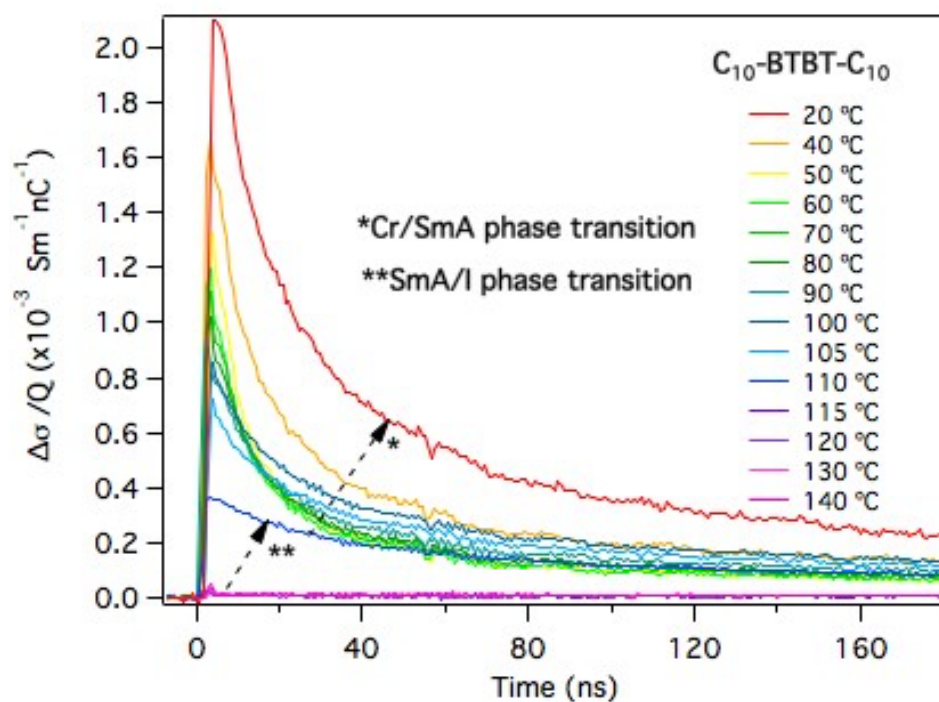


Figure 4.6. Change in conductivity upon irradiation with a 1 ns high-energy electron pulse for a) C₈-BTBT-C₈, b) C₁₀-BTBT-C₁₀, and c) C₁₂-BTBT-C₁₂ upon heating.

4.3. General Discussion

In the literature, it has commonly been assumed that band model transport in organic semiconductors is infeasible due to phonon scattering caused by their considerably narrower bandwidths compared to inorganic semiconductors, such as silicon.³³ Nevertheless, notable exceptions that exhibit band model charge transport in pure single crystals have previously been identified.^{33–39} In a typical band transport model, charge carrier mobility is thermally deactivated; i.e., it decreases with increasing temperature. In contrast to the hopping model, the charge carrier wave functions are delocalized over the entire molecule. Weak interactions control the self-assembly of organic molecules, and it is thus natural to expect the thermal motion of lattices within organic semiconductors. Since the electronic coupling between neighboring molecules is very sensitive to geometrical and structural parameters, thermal molecular motions can cause fluctuations in the electronic coupling between neighboring molecules, which significantly disrupts the translational symmetry of the electronic Hamiltonian and renders band model charge transport impossible.^{40,41} However, surprisingly high charge carrier mobilities have been reported for BTBT compounds.

The highest mobility observed in a 2,7-dioctyl-BTBT reported to date was measured to be 43 cm²/Vs in a C₈-BTBT-C₈ accomplished through FET device fabrication.⁹ Interestingly, computational studies of charge

carrier transport in the same material yielded a charge carrier mobility $< 4 \text{ cm}^2/\text{Vs}$ when using the hopping model. In contrast, a band model mobility was estimated to be between $36\text{--}58 \text{ cm}^2/\text{Vs}$.³³ However, it should be noted that this high band transport model mobility has not been independently reproduced. Furthermore, FET-based mobility measurement techniques are extremely sensitive to the microscopic morphology of the thin films at the interfaces as charge transport takes place in a very thin interface layer. The architecture of the FET device, which is dependent on source-drain electrodes, gate dielectric inhomogeneity, grain boundaries, defects, charge carrier traps, charged-impurity scattering, and non-linearity in FETs, are critical parameters that limit charge carrier mobility and charge carrier mobility extraction.⁴² For example, improving the crystallinity and morphology of thin films by finely controlling crystal formation using deposition techniques increased the charge carrier mobility of single crystal BTBT derivative (C_{12} -BTBT- C_{12}) from $4.4 \text{ cm}^2/\text{Vs}$ to $16.4 \text{ cm}^2/\text{Vs}$ for thin-film transistors fabricated for use in high-performance single-crystal semiconductor devices for large-area applications.^{43,44}

To overcome the limiting parameters that arise in OFET measurements and achieve higher charge carrier mobility values, Seki et al.⁴⁵ proposed a field-induced time-resolved microwave conductivity (FI-TRMC) method for assessing charge carrier mobility at the interface without grain boundary effects in a device with a metal-insulator-semiconductor (MIS) structure. In this technique, charge carriers are generated by selectively applying positive or negative biases, similar to the OFET technique. Evaluating charge carrier mobilities through microwave probing solves the problems associated with insulator effects, local motion, and charge carrier

dynamics at any interfacial structures found in OFETs.⁴⁶ This technique can also be used as an analytical tool for investigating the impact of interfacial trap density and insulating materials on the charge carrier mobility at the nanometer scale.⁴⁷

With this technique, Tsuts et al.¹⁰ measured a remarkably high charge carrier hole mobility of 170 cm²/Vs for an isomer of 2,7-didodecyl-BTBT (C₁₂-BTBT-C₁₂), in contrast to the average saturation mobility of 3-5 cm²/Vs generally exhibited by C₁₂-BTBT-C₁₂ in various solution- and vapor-processed OFET and OTFT device applications.^{17,18,25-27} In that study, the charge carrier mobilities of C₁₂-BTBT-C₁₂ isomers were also theoretically calculated using both charge transport models (hopping versus band transport)¹⁰. The charge transport in C₁₂-BTBT-C₁₂ was assumed to follow the band model based on its high crystallinity, however, for all C_n-BTBT-C_n (*n* = 8, 10, 12) derivatives, the difference between the calculated charge carrier mobilities at room temperature using hopping and band models was remarkably large. It therefore seems unlikely that for a particular compound in the series a bandlike mechanism is operative, while all others follow a hopping mechanism.

4.3.1. PR-TRMC vs. FI-TRMC

Given the similarity between the microwave-based conductivity techniques used in this work and in the work of Tsuts et al.¹⁰ it is of interest to compare them in some detail to identify the origin of the different results. In this chapter we investigated charge carrier mobility and charge transport mechanism of the C_n-BTBT-C_n (*n* = 8, 10, 12) derivatives (Figure 4.1) using a unique contactless microwave technique, PR-TRMC, that has

significant advantages^{48–50} over a wide range of temperatures in the context of liquid crystalline properties. In contrast to other charge carrier mobility measurement techniques (such as TOF and FI-TRMC), where the charges are injected, free charges are homogeneously generated in bulk by ionizing the sample with a high-energy electron pulse. The charge carriers are generated through irradiation by short pulses of high-energy electrons (3 MeV) in bulk—rather than at a very thin interface-layer. The concentration of charges created by the electron pulses can be tuned by changing the duration of the pulses, allowing us to obtain much lower charge carrier concentrations within the sample compared to FI-TRMC.⁴⁶ Since the penetration depth of 3 MeV electrons (~ 1.5 cm for the materials with a density of 1 g/cm^3) is much larger than the sample thickness (microwave cavity; ~ 0.5 cm), the energy deposition and ionization within the bulk sample are close to uniform.⁴⁹ Because we generate a very low uniform concentration of charges in the samples by PR-TRMC, we probe the carrier dynamics in the bulk of the solid state material. This is quite different from the FI-TRMC measurements used by Tsuts et al.¹⁰. In that case the generation of charges, and hence the charge transport, take place in a molecularly thin layer at the interface of the materials. This thin interface layer can have a different molecular organization, but the accumulation of charge in a thin layer can also result in very high charge densities. Both factors can introduce pronounced differences in the conductivity that is measured. We do stress that if the very high mobility value obtained by FI-TRMC measurements is in fact correct, it does not correspond to an intrinsic mobility in the bulk phase of solid BTBT but should be considered as a technique-specific outlier. We also stress that in this chapter, all evidence points to thermally activated transport in BTBTs, even though

the mobility values ($\sim 2\text{-}4\text{ cm}^2/\text{Vs}$) are very high for organic semiconductors.

4.4. Conclusion

To determine the effects of molecular structure and solid-state organization on the mechanism of charge transport, we investigated the temperature-dependence of charge carrier mobility and decay kinetics of $C_n\text{-BTBT-}C_n$ ($n= 8, 10, 12$) derivatives using PR-TRMC. At room temperature in their bulk state, the $C_8\text{-BTBT-}C_8$, $C_{10}\text{-BTBT-}C_{10}$, and $C_{12}\text{-BTBT-}C_{12}$ derivatives exhibited high intrinsic charge carrier mobilities of 2.94, 3.02, and 3.72 cm^2/Vs , respectively. The carrier decay kinetics showed that a large fraction of highly mobile $C_{12}\text{-BTBT-}C_{12}$ charge carriers survived on a longer timescale at room temperature compared to the other derivatives. On heating to the isotropic phase at high temperatures all $C_n\text{-BTBT-}C_n$ ($n= 8, 10, 12$) derivatives exhibited a charge carrier mobility of $\sim 0.1\text{ cm}^2/\text{Vs}$ with long-lived charge carriers, which was higher than the values observed in any other liquid crystalline or crystalline organic semiconductors. This indicates that some order is preserved in a liquid-like state that has been designated as isotropic. Temperature dependent measurement also show that the BTBT compounds investigated show a very strong dependence of charge mobility for the order on a molecular scale. On cooling back from the isotropic phase, the initial crystalline phase obtained from solution-precipitation was not fully recovered. This shows that the processing and temperature treatment very subtly affect the solid-state order, leading to large changes in the conductive properties.

For all compounds studied, charge carrier mobilities were substantially reduced at low temperatures ($-100^{\circ}\text{C} \leq T_{\text{room}}$). Therefore, we are forced to conclude that charge transport occurs via a thermally activated hopping mechanism as the primary mechanism for charge transport in C_n -BTBT- C_n ($n = 8, 10, 12$) derivatives, in contrast to what has been reported on basis of FI-TRMC measurements by Tsuts et al.¹⁰.

4.5. References

1. Martín-Palma, R. J. & Martínez-Duart, J. M. Novel Advanced Nanomaterials and Devices for Nanoelectronics and Photonics. in *Nanotechnology for Microelectronics and Photonics* 243–263 (Elsevier, 2017). doi:10.1016/B978-0-323-46176-4.00011-0.
2. Muccini, M. A bright future for organic field-effect transistors. *Nat Mater* **5**, 605 (2006).
3. Karl, N. Charge carrier transport in organic semiconductors. *Synth Met* **133–134**, 649–657 (2003).
4. Coropceanu, V. *et al.* Charge Transport in Organic Semiconductors. *Chem Rev* **107**, 926–952 (2007).
5. Iino, H. & Hanna, J. Liquid crystalline organic semiconductors for organic transistor applications. *Polym J* **49**, 23–30 (2017).
6. Haase, K. *et al.* High-Mobility, Solution-Processed Organic Field-Effect Transistors from C8-BTBT:Polystyrene Blends. *Adv Electron Mater* **4**, 1800076 (2018).
7. Janneck, R. *et al.* Highly Crystalline C8-BTBT Thin-Film Transistors by Lateral Homo-Epitaxial Growth on Printed Templates. *Advanced Materials* **29**, 1703864 (2017).
8. Schweicher, G. *et al.* Bulky End-Capped [1]Benzothieno[3,2- b]benzothiophenes: Reaching High-Mobility Organic Semiconductors by Fine Tuning of the Crystalline Solid-State Order. *Advanced Materials* **27**, 3066–3072 (2015).
9. Yuan, Y. *et al.* Ultra-high mobility transparent organic thin film transistors grown by an off-centre spin-coating method. *Nat Commun* **5**, 3005 (2014).

10. Tsutsui, Y. *et al.* Charge Carrier Mobility: Unraveling Unprecedented Charge Carrier Mobility through Structure Property Relationship of Four Isomers of Didodecyl[1]benzothieno[3,2-b][1]benzothiophene (*Adv. Mater.* 33/2016). *Advanced Materials* **28**, 7291–7291 (2016).
11. Saito, M. *et al.* One-step synthesis of [1]benzothieno[3,2-b][1]benzothiophene from o-chlorobenzaldehyde. *Tetrahedron Lett* **52**, 285–288 (2011).
12. Bittle, E. G., Basham, J. I., Jackson, T. N., Jurchescu, O. D. & Gundlach, D. J. Mobility overestimation due to gated contacts in organic field-effect transistors. *Nat Commun* **7**, 10908 (2016).
13. Uemura, T. *et al.* On the Extraction of Charge Carrier Mobility in High-Mobility Organic Transistors. *Advanced Materials* **28**, 151–155 (2016).
14. Ruzié, C., Karpinska, J., Kennedy, A. R. & Geerts, Y. H. Synthesis of 1,6-, 2,7-, 3,8-, and 4,9-Isomers of Didodecyl[1]benzothieno[3,2-b][1]benzothiophenes. *J Org Chem* **78**, 7741–7748 (2013).
15. Grigoriadis, C., Niebel, C., Ruzié, C., Geerts, Y. H. & Floudas, G. Order, Viscoelastic, and Dielectric Properties of Symmetric and Asymmetric Alkyl[1]benzothieno[3,2-b][1]benzothiophenes. *J Phys Chem B* **118**, 1443–1451 (2014).
16. Ruzié, C. *et al.* Design, synthesis, chemical stability, packing, cyclic voltammetry, ionisation potential, and charge transport of [1]benzothieno[3,2-b][1]benzothiophene derivatives. *J Mater Chem C Mater* **4**, 4863–4879 (2016).
17. Ebata, H. *et al.* Highly Soluble [1]Benzothieno[3,2-b]benzothiophene (BTBT) Derivatives for High-Performance,

- Solution-Processed Organic Field-Effect Transistors. *J Am Chem Soc* **129**, 15732–15733 (2007).
18. Izawa, T., Miyazaki, E. & Takimiya, K. Molecular Ordering of High-Performance Soluble Molecular Semiconductors and Re-evaluation of Their Field-Effect Transistor Characteristics. *Advanced Materials* **20**, 3388–3392 (2008).
 19. Iino, H., Usui, T. & Hanna, J. Liquid crystals for organic thin-film transistors. *Nat Commun* **6**, 6828 (2015).
 20. Colella, S. *et al.* High Mobility in Solution-Processed 2,7-Dialkyl-[1]benzothieno[3,2- b][1]benzothiophene-Based Field-Effect Transistors Prepared with a Simplified Deposition Method. *Chempluschem* **79**, 371–374 (2014).
 21. Gbabode, G. *et al.* X-ray Structural Investigation of Nonsymmetrically and Symmetrically Alkylated [1]Benzothieno[3,2- b]benzothiophene Derivatives in Bulk and Thin Films. *ACS Appl Mater Interfaces* **6**, 13413–13421 (2014).
 22. Wawrzinek, R. *et al.* Mobility Evaluation of [1]Benzothieno[3,2- b][1]benzothiophene Derivatives: Limitation and Impact on Charge Transport. *ACS Appl Mater Interfaces* **11**, 3271–3279 (2019).
 23. Inokuchi, H. *et al.* A Novel Type of Organic Semiconductors. Molecular Fastener. *Chem Lett* **15**, 1263–1266 (1986).
 24. Nan, G. & Li, Z. Crystal structure versus charge transport in organic single crystals of [1]benzothieno[3,2-b][1]benzothiophene derivatives from a multiscale theoretical study. *J Mater Chem C Mater* **2**, 1447 (2014).
 25. Ruzié, C. *et al.* Design, synthesis, chemical stability, packing, cyclic voltammetry, ionisation potential, and charge transport of

- [1]benzothieno[3,2-b][1]benzothiophene derivatives. *J Mater Chem C Mater* **4**, 4863–4879 (2016).
26. Uemura, T., Hirose, Y., Uno, M., Takimiya, K. & Takeya, J. Very High Mobility in Solution-Processed Organic Thin-Film Transistors of Highly Ordered [1]Benzothieno[3,2-b]benzothiophene Derivatives. *Applied Physics Express* **2**, 111501 (2009).
 27. Wang, Q. *et al.* Low-voltage, High-performance Organic Field-Effect Transistors Based on 2D Crystalline Molecular Semiconductors. *Sci Rep* **7**, 7830 (2017).
 28. Takimiya, K., Shinamura, S., Osaka, I. & Miyazaki, E. Thienoacene-Based Organic Semiconductors. *Advanced Materials* **23**, 4347–4370 (2011).
 29. Kang, M. J. *et al.* Alkylated Dinaphtho[2,3-b:2',3'-f]Thieno[3,2-b]Thiophenes (Cn-DNTTs): Organic Semiconductors for High-Performance Thin-Film Transistors. *Advanced Materials* **23**, 1222–1225 (2011).
 30. Dohr, M. *et al.* Dynamics of Monolayer-Island Transitions in 2,7-Dioctyl-benzothienobenzothiophene Thin Films. *ChemPhysChem* **14**, 2554–2559 (2013).
 31. Liu, C. *et al.* Solution-Processable Organic Single Crystals with Bandlike Transport in Field-Effect Transistors. *Advanced Materials* **23**, 523–526 (2011).
 32. Glarum, S. H. Electron mobilities in organic semiconductors. *Journal of Physics and Chemistry of Solids* **24**, 1577–1583 (1963).
 33. Kobayashi, H. *et al.* Hopping and band mobilities of pentacene, rubrene, and 2,7-dioctyl[1]benzothieno[3,2-b][1]benzothiophene

- (C 8 -BTBT) from first principle calculations. *J Chem Phys* **139**, 014707 (2013).
34. Bredas, J. L., Calbert, J. P., da Silva Filho, D. A. & Cornil, J. Organic semiconductors: A theoretical characterization of the basic parameters governing charge transport. *Proceedings of the National Academy of Sciences* **99**, 5804–5809 (2002).
 35. Jurchescu, O. D., Baas, J. & Palstra, T. T. M. Effect of impurities on the mobility of single crystal pentacene. *Appl Phys Lett* **84**, 3061–3063 (2004).
 36. Kakuta, H. *et al.* Electronic Structures of the Highest Occupied Molecular Orbital Bands of a Pentacene Ultrathin Film. *Phys Rev Lett* **98**, 247601 (2007).
 37. Ohtomo, M., Suzuki, T., Shimada, T. & Hasegawa, T. Band dispersion of quasi-single crystal thin film phase pentacene monolayer studied by angle-resolved photoelectron spectroscopy. *Appl Phys Lett* **95**, 123308 (2009).
 38. Yoshida, H. & Sato, N. Crystallographic and electronic structures of three different polymorphs of pentacene. *Phys Rev B* **77**, 235205 (2008).
 39. Northrup, J. E. Two-dimensional deformation potential model of mobility in small molecule organic semiconductors. *Appl Phys Lett* **99**, 062111 (2011).
 40. Martinelli, N. G. *et al.* Influence of intermolecular vibrations on the electronic coupling in organic semiconductors: the case of anthracene and perfluoropentacene. *ChemPhysChem* **10**, 2265–2273 (2009).

41. Baumeier, B., Kirkpatrick, J. & Andrienko, D. Density-functional based determination of intermolecular charge transfer properties for large-scale morphologies. *Physical Chemistry Chemical Physics* **12**, 11103–11113 (2010).
42. Choi, H. H., Cho, K., Frisbie, C. D., Sirringhaus, H. & Podzorov, V. Critical assessment of charge mobility extraction in FETs. *Nat Mater* **17**, 2–7 (2018).
43. Liu, C. *et al.* Controlling the crystal formation in solution-process for organic field-effect transistors with high-performance. *Org Electron* **13**, 2975–2984 (2012).
44. Minemawari, H. *et al.* Inkjet printing of single-crystal films. *Nature* **475**, 364–367 (2011).
45. Honsho, Y., Miyakai, T., Sakurai, T., Saeki, A. & Seki, S. Evaluation of Intrinsic Charge Carrier Transport at Insulator-Semiconductor Interfaces Probed by a Non-Contact Microwave-Based Technique. *Sci Rep* **3**, 3182 (2013).
46. Seki, S., Saeki, A., Sakurai, T. & Sakamaki, D. Charge carrier mobility in organic molecular materials probed by electromagnetic waves. *Phys. Chem. Chem. Phys.* **16**, 11093–11113 (2014).
47. Choi, W. *et al.* Non-contact, non-destructive, quantitative probing of interfacial trap sites for charge carrier transport at semiconductor-insulator boundary. *Appl Phys Lett* **105**, 033302 (2014).
48. Warman, J. M. *et al.* Charge Mobilities in Organic Semiconducting Materials Determined by Pulse-Radiolysis Time-Resolved Microwave Conductivity: π -Bond-Conjugated Polymers versus π - π -Stacked Discotics. *Chemistry of Materials* **16**, 4600–4609 (2004).

49. Grozema, F. C. & Siebbeles, L. D. A. Charge mobilities in conjugated polymers measured by pulse radiolysis time-resolved microwave conductivity: From single chains to solids. *Journal of Physical Chemistry Letters* **2**, 2951–2958 (2011).
50. Grozema, F. C. & Siebbeles, L. D. A. Mechanism of charge transport in self-organizing organic materials. *Int Rev Phys Chem* **27**, 87–138 (2008).

Chapter 5

Semiconducting Polyamides with Enhanced Charge Carrier Mobility

Abstract

In this chapter we explore the incorporation of conjugated chromophores in polyamide-based engineering properties with the aim to come to polymer materials that combine the mechanical properties of polyamide engineering polymers with the possibility of charge conduction. Two types of conjugated chromophores, bithiophene and perylene bisimide were incorporated in the polymer backbone. Using steady-state optical spectroscopy it is shown that there is considerable interchromophore coupling for both types of polyamides. Pulse radiolysis time-resolved microwave conductivity measurements were performed to evaluate the conductive properties. These measurements show that appreciable charge carrier mobilities can be reached in these materials. This offers interesting possibilities for the future design of (semi-)conducting polyamide-based polymers.

*Part of the results presented in this chapter have been published in:

- Özen, B., N. Candau, C. Temiz, F.C. Grozema, F.F. Tirani, R. Scopelliti, J.M. Chenal, C. J.P. Plummer, H. Frauenrath, *J Mater Chem C Mater* **8**, 6281–6292 (2020).

- Özen, B., N. Candau, C. Temiz, F.C. Grozema, G. Stoclet, C. J.P. Plummer, H. Frauenrath, *Polym Chem* **12**, 6914–6926 (2021).

5.1. Introduction

Polymer semiconductors are an attractive class of high-performance functional polymers, seamlessly merging the advantages of the electrical conductivity of semiconductors and the thermomechanical properties of plastics.¹ While their charge transport properties are similar to conventional organic semiconductors, their unique trait lies in their inherent viscoelastic nature. This arises from their ability to form continuous elastic networks with a locally dissipative response that depends on the time scale of the measurement. As a result, these materials have the potential to exhibit significantly improved strength and toughness compared to low molecular weight organic semiconductors.²

Polymer semiconductors are typically semicrystalline, containing amorphous regions as well as ordered crystalline domains characterized by two-dimensional lamellar stacks with a π -conjugated backbone separated by layers of side chains.^{3,4} The resulting morphology is complex, and understanding the charge transport in such a system has consequently remained challenging. It is essential to highlight that the performance of polymeric semiconductors is intricately tied to factors such as their chemical structure and the extent of structural order, with significant consequences for their macroscopic behavior.⁵ This leads to the exciting possibility of tuning both the mechanical and optoelectronic properties of polymer semiconductors by controlling their structural order at different length scales.³⁻¹¹ Recent studies have shown that efficient intermolecular charge transport might be achieved in high-performance polymer semiconductors that display high degrees of short-range order but no significant long-range order and no phase boundaries, provided that

aligned conjugated chain backbones form continuous paths between the locally ordered domains.^{3,4,10,12}

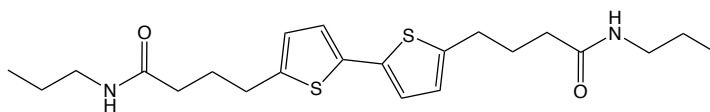
Well-defined short-range but limited long-range order are characteristic features of many polyamides. These polyamides may exhibit lamellar crystalline domains with a thickness of as little as 2 nm in the chain direction, corresponding to fewer than two repeating units, depending on their chemical structure.^{13,14} These materials are highly sought after for engineering applications owing to their excellent specific mechanical strength, stiffness, and heat resistance, particularly when hydrogen bonding between amide groups is combined with a partly or fully aromatic backbone chain.^{15,16} The introduction of hydrogen-bonded side chains into semiconducting polymers has consequently gained considerable recent attention. For instance, in π -conjugated polymers based on diketopyrrolopyrrole^{17,18} or isoindigo^{19,20} repeating units, the inclusion of amide groups in the side chains has been found both to increase the strength of aggregation and crystallinity. This results in enhanced charge carrier mobility and photovoltaic performance compared to the corresponding polymers with non-hydrogen-bonded side chains. Additionally, these modifications enhance energy dissipation during mechanical deformation.^{20,21}

By contrast, the use of amide chemistry to control order and disorder at the nanoscale has not often been investigated from the standpoint of organic electronics. Incorporating hydrogen-bonded segments as non-conjugated spacers into semiconducting polymers has received limited attention. Bao *et al.* introduced a non-conjugated unit containing an amide group into the backbone of a π -conjugated polymer.²² They found that 10 mol% of this co-monomer sufficed to alter the thin film

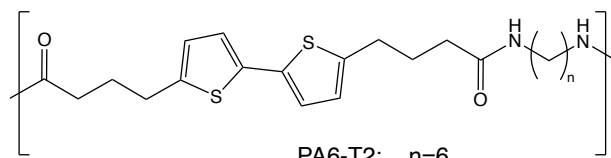
morphology of the polymer network, leading to a reduction in elastic modulus and a moderate increase in crack onset strain—however, no significant change in charge carrier properties. Muguruma *et al.* prepared semi-aromatic polyamides with oligothiophene units but provided no details of their morphology or mechanical and optoelectronic properties.^{23,24}

Here, we report a library of polyamides containing hydrogen bonding interactions and exhibit their optoelectronic properties. These polyamides contain repeating units of electron-deficient, n-type semiconducting dithiophene and dicyanoperylene bisimide, with varying aliphatic spacer lengths. By examining semicrystalline semi-aromatic polyamides with bithiophene units, we found that such materials combine the thermochemical characteristics of typical semi-aromatic engineering polyamides with significant charge carrier mobility. Additionally, polyamides containing dicyanoperylene bisimide repeating units showed not only good thermal stability and shear moduli in the range of 0.75 – 0.93 GPa, but also H-type coupling of the dicyanoperlyene bisimide chromophores in the solid-state. Charge carrier mobilities of about 0.01 cm²/Vs underscore a promising initial step towards functional semiconducting engineering thermoplastics.

A

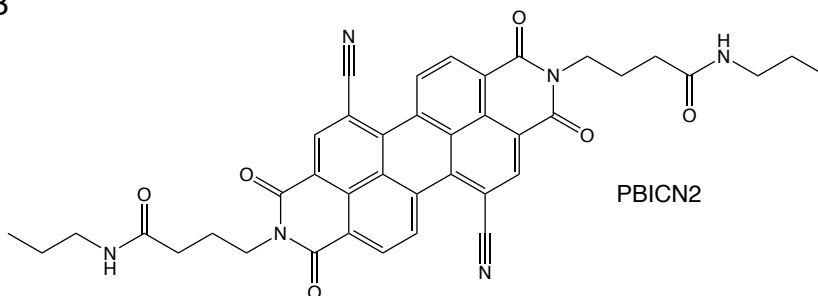


T2a

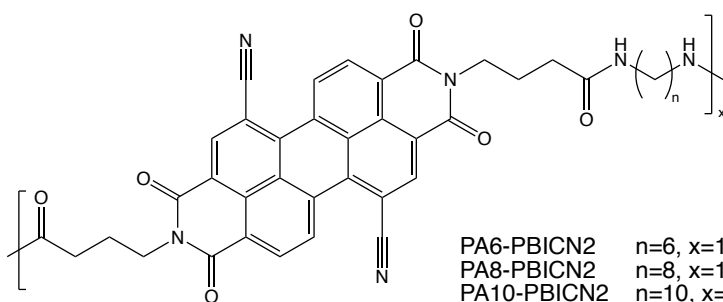


PA6-T2: n=6
PA12-T2: n=12

B



PBICN2



PA6-PBICN2 n=6, x=13.4
PA8-PBICN2 n=8, x=14.8
PA10-PBICN2 n=10, x=12
PA12-PBICN2 n=12, x=19.2

Figure 5.1. Molecular structure of bithiophene-based amides (A) and perylenebisimide-based amides (B).

5.2. Experimental Details

The conductivity of the polymers and reference compounds were measured using the Pulse Radiolysis Time-Resolved Microwave Conductivity (PR-TRMC) technique. In this technique, charges were generated in powder samples (20–50 mg) by irradiation with short pulses (2–20 ns) of high-energy electrons (3 MeV) from a Van de Graaff accelerator. The penetration depth of these high-energy electrons in the materials is several millimeters, resulting in a close to homogenous ionization and hence a uniform concentration of charges throughout the material. The change in conductivity of the material due to charges generated by the irradiation was probed using high frequency microwaves (28 to 38 GHz). The fractional change in the microwave power ($\Delta P/P$) absorbed on irradiation is directly proportional to the change in the conductivity ($\Delta\sigma$) according to

$$\frac{\Delta P}{P} = -A\Delta\sigma$$

where the sensitivity factor, A , is a sensitivity factor that depends on the geometric and dielectric properties of the material.²⁵ The conductivity ($\Delta\sigma$) is related to the mobility of all charged species, and their concentration, N_p , through

$$\Delta\sigma = eN_p \sum \mu$$

where e is the elementary charge ($1.6 \cdot 10^{-19}$ C). This equation allows the mobility of the charge carriers to be calculated, given a reasonable estimate

of their concentration. Such an estimate may be obtained from dosimetry measurements, which provides the amount of energy deposited by the electron pulse, as described in detail previously.²⁶

5.3. Results & Discussion

UV-vis optical absorption

The polyamides and model compounds shown in Figure 1 were synthesized and characterized as described by Ozen *et al.*^{14,27}

UV-vis absorption and fluorescence spectroscopy used gain insight in the packing and the photophysical properties of the polyamide compounds and their model systems. For the thiophene- and PBI-based series the representative compounds **PA6-PBICN2** & **PA6-T2** and the model compounds **PBICN2** & **T2a** were selected for UV-vis spectroscopy.

The UV-vis absorption spectra of **PA6-T2** and the model compound **T2a** in hexafluoroisopropanol (HFIP) solution and on a quartz substrate are shown in Figure 5.2. In solution both compounds show an absorption band with a maximum at 317 nm and a shoulder at around 340 nm. Thin films of **PA6-T2** and the model compound **T2a** spin-coated onto quartz substrates exhibit similar absorptions except for a small solid-state red shift, with absorption maxima at 323 and 321 nm, respectively, and shoulders at around 360 nm. This clearly indicates some electronic interaction between neighboring chromophores in the solid state. No clear difference between the polymer **PA6-T2** and the model compound **T2a** is observed.

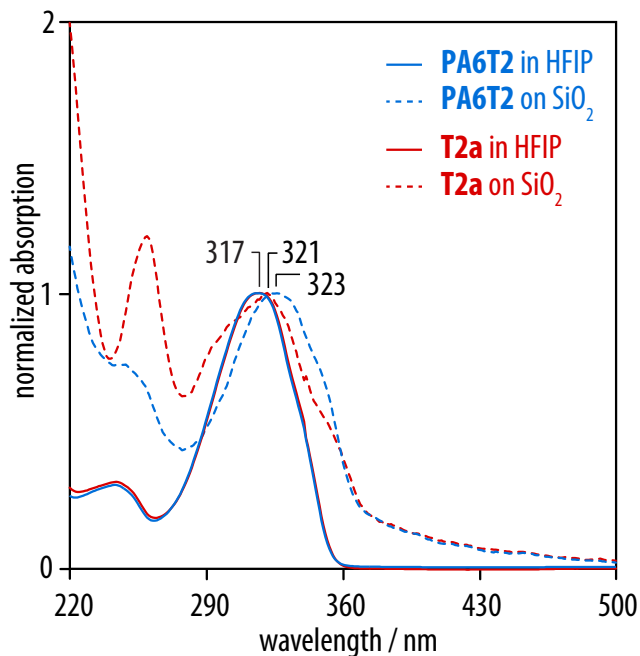


Figure 5.2. UV-vis absorption spectra of PA6-T2 and T2a in HFIP solution and on a SiO₂ substrate.

The UV-vis absorption and fluorescence spectra for **PBICN** and **PA6-PBICN2** are shown in Figure 3, both in solution and in the solid state. In trifluoro acetic acid (TFA) solution ($c = 10^{-4}$ mol/L), both **PA6-PBICN** and **PBICN2** show a strong $S_0 - S_1$ absorption at 527 nm (0-0) with higher vibronic bands at 492 nm (0-1) and 462 nm (0-2). The ratio of the 0-0 and the 0-1 (A_{0-0} / A_{0-1}) absorption intensities was around 1.48, which is similar to the typical values of perylene bisimide derivatives in solution and indicated spectroscopic aggregates to be absent in TFA at this concentration.²⁸⁻³⁰ Emission spectra from diluted solutions of both **PA6-PBICN** and **PBICN2** in TFA ($c = 10^{-6}$ mol/L) revealed a Stokes shift of 15 nm and well-resolved vibronic fine structure patterns with fluorescence

maxima at 542 nm and shoulders at 574 nm mirroring the corresponding absorption spectra.

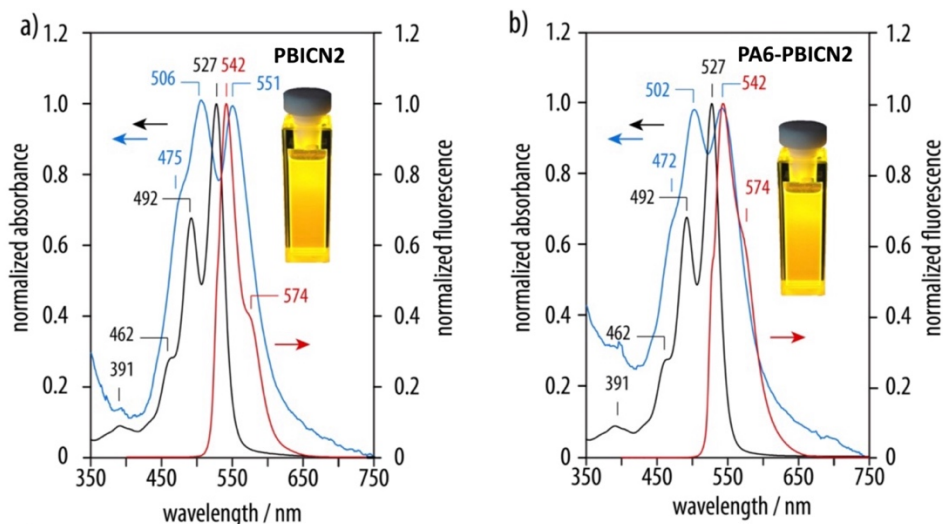


Figure 5.3. Normalized UV-vis (solution-phase and thin film) absorption and solution-phase fluorescence spectra of a) model compound **PBICN2** and b) **PA6-PBICN2**. The solution-phase spectra were obtained from TFA solutions (black: absorption spectra, $c = 10^{-4}$ mol/L; red: fluorescence spectra $c = 10^{-6}$ mol/L), while thin film spectra were obtained from spin-coated thin films on quartz substrates (blue). The inset shows the corresponding specimens under UV light (254 nm).

Thin films of **PA6-PBICN** and **PBICN2** prepared by spin-coating from TFA ($c = 10^{-3}$ mol/L) onto quartz substrates exhibited spectral signatures with two main absorptions at 551 nm and 506 nm for **PBICN2**, and 542 nm and 522 nm for **PA6-PBICN** with the shoulders at 472 nm and 475 nm for **PBICN2** and **PA6-PBICN** respectively. The weak red-shift (15-20 nm) of the highest-wavelength absorption peak, the strong decrease

in the respective $A_{0.0} / A_{0.1}$ ratios to 0.98 for **PBICN2** and 1.0 for **PA6-PBICN**, and almost complete quenching of fluorescence suggested pronounced H-type coupling of the dicyanoperylene bisimide chromophores. H-type coupling is commonly seen almost cofacial, parallel-displaced arrangement of these type of chromophores in the solid state.³¹⁻³⁴ Overall, these results for both the polymer and the model compound show that there is sufficient interchromophore coupling to lead to significant changes in the UV-vis spectrum. The splitting of the absorption bands in the solid state seems somewhat more pronounced for the model compound **PBICN2** than for the polymer **PA6-PBICN2**.

Pulse-radiolysis TRMC measurements

In order to gain insight in the conductive properties of both series of polyamides and the corresponding model compounds we have performed pulse-radiolysis time-resolved microwave conductivity (PR-TRMC) experiments on all of these materials at room temperature, as described above.

The results from PR-TRMC measurements on the **PA n -T2** series are shown in Figure 5.4. The figure shows the change in conductivity upon irradiation with a 10 ns pulse of high-energy electrons. The conductivity signal is seen to increase during the irradiation pulse due to the formation of charges, and subsequently decays. The latter can be due to trapping of charges or recombination. Further measurements using different initial concentrations of charges reveal a first order decay kinetics, indicating that charges primarily decay by trapping.

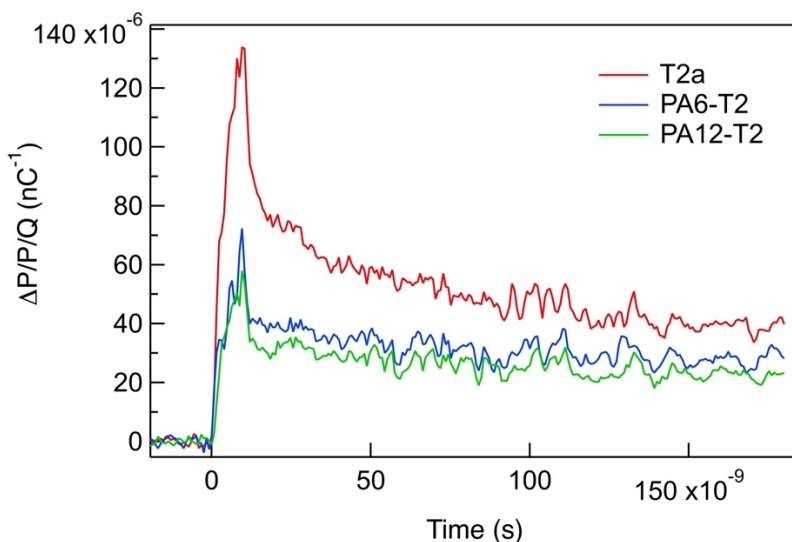


Figure 5.4. Change in conductivity in thiophene-based polyamide compounds upon irradiation with a 10 ns pulse of 3 MeV electrons.

As discussed above, a value for the mobility of charge carriers can be derived from the radiation-induced conductivity if the initial concentration of charges is known. From the measurements presented in Figure 4, one-dimensional charge carrier mobility determined from the end-of-pulse conductivity resulted in mobilities, μ_{1D} , of $0.044 \text{ cm}^2\text{V}^{-1}\text{s}^{-1}$ (**T2a**), $0.017 \text{ cm}^2\text{V}^{-1}\text{s}^{-1}$ (**PA6-T2**) and $0.018 \text{ cm}^2\text{V}^{-1}\text{s}^{-1}$ (**PA12-T2**), as summarized in Table 5.1. We assume one-dimensional charge transport in the materials since structural analysis shows that the stacking of the bithiophenes leads to 1D pathways in the solid state.

The mobility for **T2a** is around one order of magnitude higher than the highest values of $0.005 \text{ cm}^2 \text{V}^{-1} \text{s}^{-1}$ reported for other bithiophene-based systems,³⁵ and close to those in crystalline quaterthiophene and sexithiophene-based systems.^{36–39} This can be seen as an indication of the beneficial effect of hydrogen bonded substituents on the packing of π -

conjugated systems and hence the charge transport properties of the materials.⁴⁰ For the **PAn-T2** polymer compounds, the mobility lowers by more than a factor two, which can be explained by the restricted conformational freedom due to the incorporation of the bithiophene in a polymer chain.

Table 5.1. Chemical Structures of bithiophene-based and perylenebisimid-based amide model compounds, polyamides and their charge carrier mobility values measured by PR-TRMC at room temperature.

Compound	Charge Carrier Mobility ($\times 10^{-2} \text{ cm}^2/\text{Vs}$)
T2a	4.4
PA6-T2	1.7
P12-T2	1.8
PBICN2	1.4
PA6-PBICN2	1.1
PA8-PBICN2	1.2
PA10-PBICN2	1.0
PA12-PBICN2	1.0

The results from PR-TRMC measurements on the perylene bisimide-based compounds are shown in Figure 5.5. The measurements resulted in clear conductivity transients, similar to those for the bithiophene-based compounds in Figure 5.4. This resulted in one-

dimensional charge carrier mobilities, $\mu_{ID} = 1.4 \times 10^{-2} \text{ cm}^2/\text{Vs}$ for **PBICN2**, $1.1 \times 10^{-2} \text{ cm}^2/\text{Vs}$ for **PA6-PBICN2**, $1.2 \times 10^{-2} \text{ cm}^2/\text{Vs}$ for **PA8-PBICN2**, $1.0 \times 10^{-2} \text{ cm}^2/\text{Vs}$ for **PA10-PBICN2** and **PA12-PBICN2**, as listed in the Table 5.1. For bisubstituted perylene bisimides, including liquid crystalline molecules values in excess of $0.1 \text{ cm}^2/\text{Vs}$ have been reported,⁴¹ which is an order of magnitude higher than the values reported here. The values are, however, comparable to those for other hydrogen-bonded perylene bisimide organogelators.⁴² It is well-known that the mobility in perylene derivatives strongly depends on the solid-state packing, even for highly crystalline materials.⁴³ Clearly, the incorporation of hydrogen bonding moieties and inclusion in a polymer chain leads to stacking conformations that are not optimal for charge transport. Nevertheless, the observation of a significant charge carrier mobility is encouraging for the design of polyamide-based polymer systems that can transport charge.

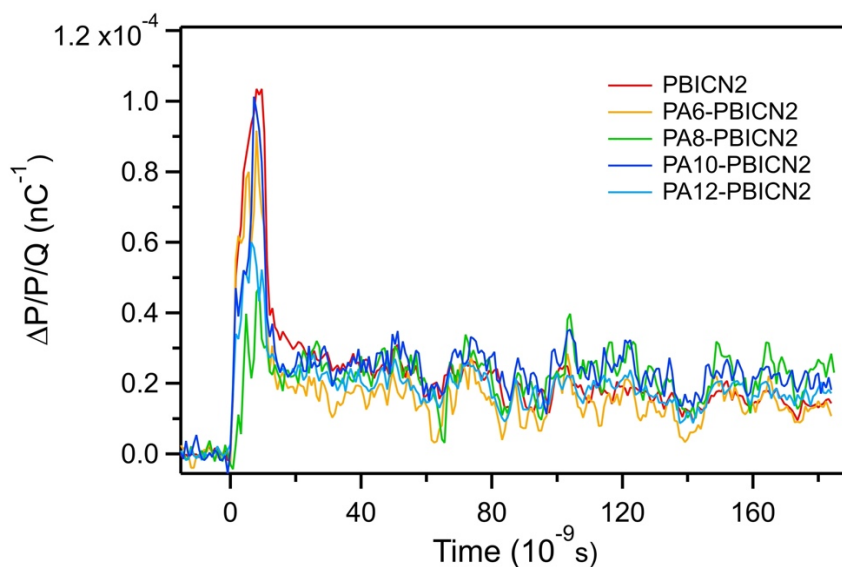


Figure 5.5. Change in conductivity in perylene bisimide-based polyamide compounds upon irradiation with a 10 ns pulse of 3 MeV electrons.

The charge carrier mobility values of the polymers are significantly lower than for the small molecule equivalent. It is likely that the incorporation of the monomers into a polymer restricts the possibility of finding an optimal geometry for charge transport.

5.4. Conclusion

The results presented in this chapter show that the incorporation of conjugated chromophores in polyamide chains can result in polymer compounds that combine the desirable mechanical properties of common polyamides with a sufficiently high conductance to make them interesting for applications. The optical properties of the polymers and model compounds show that there is substantial electronic interaction between the conjugated subunits in the solid state, induced by interchain hydrogen bonding. From PR-TRMC measurements we conclude that this interaction is sufficient to lead to significant charge carrier mobilities in the materials.

5.5. References

1. Root, S. E., Savagatrup, S., Printz, A. D., Rodriquez, D. & Lipomi, D. J. Mechanical Properties of Organic Semiconductors for Stretchable, Highly Flexible, and Mechanically Robust Electronics. *Chem Rev* **117**, 6467–6499 (2017).
2. Heeger, A. J. Semiconducting and Metallic Polymers: The Fourth Generation of Polymeric Materials. *J Phys Chem B* **105**, 8475–8491 (2001).
3. McCullough, R. D., Tristram-Nagle, S., Williams, S. P., Lowe, R. D. & Jayaraman, M. Self-orienting head-to-tail poly(3-alkylthiophenes): new insights on structure-property relationships in conducting polymers. *J Am Chem Soc* **115**, 4910–4911 (1993).
4. Sirringhaus, H. *et al.* Two-dimensional charge transport in self-organized, high-mobility conjugated polymers. *Nature* **401**, 685–688 (1999).
5. Koch, F. P. V. *et al.* The impact of molecular weight on microstructure and charge transport in semicrystalline polymer semiconductors—poly(3-hexylthiophene), a model study. *Prog Polym Sci* **38**, 1978–1989 (2013).
6. Rivnay, J., Mannsfeld, S. C. B., Miller, C. E., Salleo, A. & Toney, M. F. Quantitative Determination of Organic Semiconductor Microstructure from the Molecular to Device Scale. *Chem Rev* **112**, 5488–5519 (2012).
7. Grozema, F. C. & Siebbeles, L. D. A. Mechanism of charge transport in self-organizing organic materials. *Int Rev Phys Chem* **27**, 87–138 (2008).

8. Sirringhaus, H. 25th Anniversary Article: Organic Field-Effect Transistors: The Path Beyond Amorphous Silicon. *Advanced Materials* **26**, 1319–1335 (2014).
9. Osaka, I. Semiconducting polymers based on electron-deficient π -building units. *Polym J* **47**, 18–25 (2015).
10. Noriega, R. *et al.* A general relationship between disorder, aggregation and charge transport in conjugated polymers. *Nat Mater* **12**, 1038–1044 (2013).
11. Yang, Y., Liu, Z., Zhang, G., Zhang, X. & Zhang, D. The Effects of Side Chains on the Charge Mobilities and Functionalities of Semiconducting Conjugated Polymers beyond Solubilities. *Advanced Materials* **31**, (2019).
12. Nikolka, M. *et al.* High-mobility, trap-free charge transport in conjugated polymer diodes. *Nat Commun* **10**, 2122 (2019).
13. Lee, S. S. & Phillips, P. J. Melt crystallized polyamide 6.6 and its copolymers, Part I. Melting point – Lamellar thickness relations in the homopolymer. *Eur Polym J* **43**, 1933–1951 (2007).
14. Candau, N. *et al.* High-performance polyamides with engineered disorder. *Polym Chem* **12**, 6426–6435 (2021).
15. Marchildon, K. Polyamides – Still Strong After Seventy Years. *Macromol React Eng* **5**, 22–54 (2011).
16. Jalal Uddin, A. *et al.* Melt spinning and laser-heated drawing of a new semiaromatic polyamide, PA9-T fiber. *J Polym Sci B Polym Phys* **42**, 433–444 (2004).
17. Yao, J. *et al.* Significant Improvement of Semiconducting Performance of the Diketopyrrolopyrrole–Quaterthiophene

- Conjugated Polymer through Side-Chain Engineering via Hydrogen-Bonding. *J Am Chem Soc* **138**, 173–185 (2016).
18. Ocheje, M. U. *et al.* Amide-Containing Alkyl Chains in Conjugated Polymers: Effect on Self-Assembly and Electronic Properties. *Macromolecules* **51**, 1336–1344 (2018).
 19. Charron, B. P. *et al.* Electronic properties of isoindigo-based conjugated polymers bearing urea-containing and linear alkyl side chains. *J Mater Chem C Mater* **6**, 12070–12078 (2018).
 20. Lin, Y.-C., Shih, C.-C., Chiang, Y.-C., Chen, C.-K. & Chen, W.-C. Intrinsically stretchable isoindigo–bithiophene conjugated copolymers using poly(acrylate amide) side chains for organic field-effect transistors. *Polym Chem* **10**, 5172–5183 (2019).
 21. Ocheje, M. U. *et al.* Influence of amide-containing side chains on the mechanical properties of diketopyrrolopyrrole-based polymers. *Polym Chem* **9**, 5531–5542 (2018).
 22. Oh, J. Y. *et al.* Intrinsically stretchable and healable semiconducting polymer for organic transistors. *Nature* **539**, 411–415 (2016).
 23. Muguruma, H., Yudasaka, M. & Hotta, S. Vapor polymerization deposition of new polyamide thin films having oligothiophene segments in the main chain. *Thin Solid Films* **339**, 120–122 (1999).
 24. Muguruma, H., Matsumura, K. & Hotta, S. Molecular orientation of oligothiophene-based polyamide thin films fabricated by vapor deposition polymerization. *Thin Solid Films* **405**, 77–80 (2002).
 25. Infelta, P. P., de Haas, M. P. & Warman, J. M. The study of the transient conductivity of pulse irradiated dielectric liquids on a nanosecond timescale using microwaves. *Radiation Physics and Chemistry (1977)* **10**, 353–365 (1977).

26. Warman, J. M. *et al.* Charge Mobilities in Organic Semiconducting Materials Determined by Pulse-Radiolysis Time-Resolved Microwave Conductivity: π -Bond-Conjugated Polymers versus π - π -Stacked Discotics. *Chemistry of Materials* **16**, 4600–4609 (2004).
27. Özen, B. *et al.* Semiaromatic polyamides with enhanced charge carrier mobility. *Polym Chem* **12**, 6914–6926 (2021).
28. Yagai, S. *et al.* Supramolecularly Engineered Perylene Bisimide Assemblies Exhibiting Thermal Transition from Columnar to Multilamellar Structures. *J Am Chem Soc* **134**, 7983–7994 (2012).
29. Kaufmann, C., Bialas, D., Stolte, M. & Würthner, F. Discrete π -Stacks of Perylene Bisimide Dyes within Folda-Dimers: Insight into Long- and Short-Range Exciton Coupling. *J Am Chem Soc* **140**, 9986–9995 (2018).
30. Giaimo, J. M. *et al.* Excited Singlet States of Covalently Bound, Cofacial Dimers and Trimers of Perylene-3,4:9,10-bis(dicarboximide)s. *J Phys Chem A* **112**, 2322–2330 (2008).
31. Spano, F. C. The Spectral Signatures of Frenkel Polarons in H- and J-Aggregates. *Acc Chem Res* **43**, 429–439 (2010).
32. Würthner, F., Chen, Z., Dehm, V. & Stepanenko, V. One-dimensional luminescent nanoaggregates of perylene bisimides. *Chemical Communications* 1188 (2006) doi:10.1039/b517020f.
33. Seibt, J. *et al.* On the geometry dependence of molecular dimer spectra with an application to aggregates of perylene bisimide. *Chem Phys* **328**, 354–362 (2006).

34. Dehm, V. *et al.* Helical Growth of Semiconducting Columnar Dye Assemblies Based on Chiral Perylene Bisimides. *Org Lett* **9**, 1085–1088 (2007).
35. Schoonbeek, F. S. *et al.* Efficient Intermolecular Charge Transport in Self-Assembled Fibers of Mono- and Bithiophene Bisurea Compounds. *Angewandte Chemie International Edition* **38**, 1393–1397 (1999).
36. Pratihari, P. *et al.* Self-assembly and semiconductivity of an oligothiophene supergelator. *Beilstein Journal of Organic Chemistry* **6**, 1070–1078 (2010).
37. Wegewijs, B., de Haas, M. P., de Leeuw, D. M., Wilson, R. & Sringhaus, H. Charge carrier mobilities in mesomorphic α,ω -dihexylquaterthiophene: A comparative microwave conductivity and thin film transistor study. *Synth Met* **101**, 534–535 (1999).
38. Grozema, F. C. *et al.* Frequency dependence of the charge carrier mobility in DH4T. *Synth Met* **119**, 463–464 (2001).
39. de Haas, M. P. *et al.* Mobile charge carriers in pulse-irradiated poly- and oligothiophenes. *Synth Met* **101**, 524–525 (1999).
40. Gebers, J. *et al.* Crystallization and Organic Field-Effect Transistor Performance of a Hydrogen-Bonded Quaterthiophene. *Chemistry – A European Journal* **26**, 10265–10275 (2020).
41. Struijk, C. W. *et al.* Liquid Crystalline Perylene Diimides: Architecture and Charge Carrier Mobilities. *J Am Chem Soc* **122**, 11057–11066 (2000).
42. Li, X.-Q. *et al.* Functional organogels from highly efficient organogelator based on perylene bisimide semiconductor. *Chem. Commun.* 3871–3873 (2006) doi:10.1039/B611422A.

43. Delgado, M. C. R., Kim, E.-G., Filho, D. A. da S. & Bredas, J.-L. Tuning the Charge-Transport Parameters of Perylene Diimide Single Crystals via End and/or Core Functionalization: A Density Functional Theory Investigation. *J Am Chem Soc* **132**, 3375–3387 (2010).

Summary

Organic semiconductors emerge as a class of alternative materials for electronic applications. These materials offer tunable optoelectronic properties through chemical synthesis and modification, low production cost, relatively easy and flexible processing, and potential for large-area applications. Achieving efficient charge transport in these materials relies on controlling the local- and long-range arrangement of the individual molecules, which can be tuned by changes in their chemical structure. This dissertation primarily focuses on the manipulation of the supramolecular order by targeted changes in the molecular structure, specifically focusing on the relation between the ordering and the optoelectronic properties.

Chapter 1 introduces the main concepts used in this thesis and provides an overview of self-assembling liquid crystalline materials. The chapter starts with a brief overview of organic semiconductor materials and their device applications. After a brief discussion of self-assembling liquid crystalline materials and the intermolecular interactions that control their assembly properties, this thesis discusses two main structural ordering patterns: calamitic and discotic mesogens. Next, we discuss the theoretical background of charge transport in organic semiconductors and describe the possible transport mechanisms involved, together with a brief literature survey and some remarks on the relevance of the research reported in this thesis. Finally, we briefly discussed some common methods for measuring charge transport, including the Four-Contact Probe Method, Time-of-Flight (TOF), Space-Charge Limited Current (SCLC), Organic Field-Effect Transistors (OFET), Pulse-Radiolysis Time-

Resolved Microwave Conductivity (PR-TRMC) and Field-Induced Time-Resolved Microwave Conductivity (FI-TRMC).

Chapter 2 describes the synthesis of two novel peripherally substituted discotic liquid crystalline hexa-*peri*-hexabenzocoronene (HBC) compounds and the influence of substitution position (*meta*- vs *para*-) on the aggregation properties in solution. We showed that the position of the substituent (*meta*- vs *para*-) has a pronounced effect on the aggregation. A detailed temperature- and concentration-dependent ^1H -NMR analysis shows that both *meta*- and *para*- position substituted alkoxy side chains on the phenyl rings attached to the HBC core exhibit a high tendency to aggregate. However, further concentration and temperature-dependent optical measurements displayed that the derivative with *para*-position substitution (ParaHBC) has increased π - π interactions between neighboring cores and stronger interlocking of hexa-phenyl rings at the side chains, leading to the enhanced aggregate formation in solution, as compared to the *meta*-position substituted derivative, MetaHBC. This is attributed to the larger conformational freedom present in *meta*-HBC, which can adopt more disordered conformations that hamper aggregation. The NMR measurements also suggest different stacking conformations for the two compounds, which can have a noticeable effect on the charge transport properties. Finally, this chapter highlights the role of solvent properties on the aggregation properties in solution. In all common good and bad solvents, *para*-HBC shows a higher tendency to aggregate.

In Chapter 3 we study the relationship between supramolecular organization and molecular design of tailored HBC derivatives in the solid state. By performing temperature-dependent charge transport measurements, we also gain insight into the charge transport of the

different mesophases in these HBC isomers. This chapter demonstrates that one of the main factors that determines the charge transport is the degree of order in the columnar structures, which is temperature-dependent. DSC analysis shows that both HBC isomers retain their liquid crystalline properties across the full temperature range (from $-100\text{ }^{\circ}\text{C}$ to $>400\text{ }^{\circ}\text{C}$) with no clear isotropization temperature. ParaHBC exhibits a thermally stable ordered columnar phase (Col) at ambient temperature with a charge carrier mobility of $0.135\text{ cm}^2/\text{Vs}$ and a plastic crystalline phase (Col_p) at low temperatures with slightly increased charge carrier mobility of $0.139\text{ cm}^2/\text{Vs}$. Introducing bulky alkoxy side chains substituted with free-to-rotate phenyl rings on the *meta*-position induces steric restrictions that influence the stacking behavior, leading to more disorder. PR-TRMC measurements of MetaHBC show that this results in a substantially lower charge carrier mobility, $0.06\text{ cm}^2/\text{Vs}$ at room temperature. The mobility monotonically decreases with decreasing temperature, corresponding to a thermally activated hopping mechanism. Preliminary studies also show that changes in the preparation procedures and recrystallization of HBC derivatives can improve the columnar order of MetaHBC.

Chapter 4 focuses on the charge transport mechanism and comparison of investigated intrinsic charge carrier mobility in rod-like liquid crystalline [1]benzothieno[3,2-b][1]benzothiophene (BTBT) derivatives with varying side chain length in the bulk state by investigating the following parameters: crystal packing, molecular structure, mesomorphism, disorder, defects, traps, and temperature. All C_n -BTBT- C_n ($n = 8, 10, 12$) derivatives exhibit herringbone packing motifs that introduce 2D charge transport pathways. The temperature dependence of the charge carrier mobility and decay kinetics of C_n -BTBT- C_n ($n = 8, 10,$

12) were investigated by PR-TRMC measurements. Remarkably high intrinsic charge carrier mobilities of 2.94, 3.02, and 3.72 cm²/Vs, respectively, were obtained for these compounds. Analysis of the decay kinetics shows that a large fraction of highly mobile C₁₂-BTBT-C₁₂ charge carriers survived on a longer timescale at room temperature compared to the other derivatives. However, charge carrier mobilities were dramatically reduced at low temperatures (down to -100°C) for all derivatives, and conductivity transients decayed faster because of charge recombination and increased trapping. Dynamic and static deviations from the original perfect crystalline arrangements acted as a strong source of disorders at all temperatures, leading to the localization of charge carriers and strengthened the argument for a thermally activated hopping model as the primary mechanism for charge transport in C_n-BTBT-C_n (n = 8, 10, 12) derivatives.

In Chapter 5, we report on a series of polyamides that can exhibit interchain hydrogen bonds, and describe their optoelectronic properties. These polyamides contain repeating units of electron-deficient, n-type semiconducting bithiophene and dicyanoperylene bisimide, with varying aliphatic spacer lengths. We find that such materials combine the thermochemical characteristics of typical semi-aromatic engineering polyamides with significant charge carrier mobility. PR-TRMC results showed that the length of the aliphatic spacer length does not significantly affect the intracolumnar charge transport in such polyamide derivatives. However, both bithiophene and dicyanoperylene bisimide containing polyamides showed increased charge carrier mobility values compared to their analogues in the literature, indicating the beneficial effect of

hydrogen-bonded substituents on the packing of π -conjugated systems and hence the charge transport properties of the materials.

Samenvatting

Organische halfgeleiders zijn een opkomende klasse alternatieve materialen voor elektronische toepassingen. Voordelen van deze materialen zijn onder andere de mogelijkheid om de opto-elektronische eigenschappen aan te passen door middel van chemische synthese, goedkope en relatief gemakkelijke en flexibele verwerking en fabricage, de potentiële kosteneffectiviteit bij massaproductie en mogelijke toepassingen op grote oppervlakken. Het bereiken van efficiënt ladingstransport in deze materialen is echter afhankelijk van controle over de rangschikking van de individuele moleculen op verschillende lengteschalen door middel van modificaties in hun chemische structuur. Dit proefschrift richt zich primair op de manipulatie van de supramoleculaire orde door gerichte veranderingen in de moleculaire structuur, waarbij de nadruk specifiek ligt op de relatie tussen de moleculaire ordening en de opto-elektronische eigenschappen.

Hoofdstuk 1 introduceert de belangrijkste concepten die in dit proefschrift worden gebruikt en geeft een overzicht van zelf-organiserende vloeibaar-kristallijne materialen. Het hoofdstuk begint met een kort overzicht van organische halfgeleidermaterialen en hun toepassingen in elektronische componenten (devices). Na een korte discussie over zelf-organiserende vloeibaar-kristallijne materialen en de intermoleculaire interacties die hun assemblage-eigenschappen controleren, worden twee belangrijke structurele organisaties besproken die in dit proefschrift voorkomen; namelijk calamitische en discotische mesogenen. Vervolgens bespreken we de theoretische achtergrond van ladingstransport in

organische halfgeleiders en beschrijven we de mogelijke transportmechanismen, samen met een kort literatuuronderzoek en enkele opmerkingen over de relevantie van het onderzoek beschreven in dit proefschrift. Ten slotte worden kort enkele veelgebruikte methoden besproken voor het meten van ladingstransport, waaronder Four-Contact Probe Method, Time-of-Flight (TOF), Space-Charge Limited Current (SCLC), Organic Field-Effect Transistors (OFET), Pulse-Radiolysis Tijdsopgeloste microgolfsgeleiding (PR-TRMC) en veldgeïnduceerde tijdsopgeloste microgolfsgeleiding (FI-TRMC).

Hoofdstuk 2 beschrijft de synthese van twee nieuwe gesubstitueerde discotische vloeibaar-kristallijne hexa-peri-hexabenzocoroneen (HBC) verbindingen en de invloed van de substitutiepositie (meta- versus para-) op de aggregatie-eigenschappen in oplossing. Er wordt aangetoond dat de positie van de substituent (meta-versus para-) een uitgesproken effect heeft op de aggregatie. Een gedetailleerde temperatuur- en concentratieafhankelijke $^1\text{H-NMR}$ -analyse toont aan dat zowel verbindingen met meta- als para-positie gesubstitueerde alkoxy-zijketens op de fenylringen die aan de HBC-kern zijn bevestigd een hoge neiging tot aggregatie vertonen. Uit verdere concentratie- en temperatuurafhankelijke optische metingen blijkt echter dat in de verbinding met substitutie op de para-positie (ParaHBC) de π - π -interacties tussen aangrenzende moleculen de onderlinge interactie groter is, wat leidt tot verbeterde aggregaatvorming in oplossing, in vergelijking met het meta-positie gesubstitueerde derivaat, MetaHBC. Dit wordt toegeschreven aan de grotere conformationele vrijheid die aanwezig is in meta-HBC, die meer wanordelijke conformaties kan aannemen die aggregatie belemmeren. De NMR-metingen suggereren ook verschillende

manieren van moleculaire organisatie voor de twee verbindingen, wat een merkbaar effect kan hebben op de ladingstransporteigenschappen. Tot slot belicht dit hoofdstuk de rol van het type oplosmiddel op de aggregatie-eigenschappen in oplossingen. In alle algemeen goede en slechte oplosmiddelen vertoont para-HBC een grotere neiging tot aggregatie.

In **Hoofdstuk 3** bestuderen we de relatie tussen de supramoleculaire organisatie en het moleculaire ontwerp van HBC-verbindingen in de vaste stof. Door temperatuurafhankelijke ladingstransportmetingen uit te voeren, krijgen we ook inzicht in het ladingstransportmechanisme in de verschillende mesofasen van deze HBC-isomeren. Dit hoofdstuk laat zien dat een van de belangrijkste factoren die het ladingstransport bepalen de mate van ordening in de kolomvormige structuren is. Deze ordening is temperatuurafhankelijk. DSC-analyse toont aan dat beide HBC-isomeren hun vloeibaar-kristallijne eigenschappen behouden over het volledige temperatuurbereik (van -100 °C tot > 400 °C) zonder duidelijke isotropisatietemperatuur. ParaHBC vertoont een thermisch stabiele geordende kolomvormige fase (Col) bij kamertemperatuur met een ladingsdragermobiliteit van $0,135$ cm²/Vs en een plastisch kristallijne fase (Colp) bij lage temperaturen met een licht verhoogde ladingsdragermobiliteit van $0,139$ cm²/Vs. Het introduceren van ‘bulky’ alkoxy-zijketens gesubstitueerd met vrij te roteren fenylringen op de meta-positie leidt tot sterische beperkingen die de moleculaire ordening beïnvloeden, wat leidt tot een grotere wanorde. PR-TRMC-metingen aan MetaHBC laten zien dat dit resulteert in een substantieel lagere mobiliteit van ladingsdragers, $0,06$ cm²/Vs bij kamertemperatuur. De mobiliteit neemt monotoon af met afnemende temperatuur bij afkoeling, wat wijst op een thermisch geactiveerd ‘hopping’-mechanisme.

Deze voorlopige resultaten laten ook zien dat veranderingen in de bereidingsprocedures en herkristallisatie van HBC-derivaten de moleculaire ordening van MetaHBC kunnen verbeteren.

Hoofdstuk 4 richt zich op het ladingstransportmechanisme en de vergelijking van de onderzochte intrinsieke mobiliteit van ladingsdragers in staafachtige vloeibaar-kristallijne [1]benzothieno[3,2-b][1]benzothiofeen (BTBT) derivaten met variërende zijketenlengte in de bulktoestand door de volgende parameters in ogenschouw te nemen: kristalpakking, moleculaire structuur, mesomorfisme, wanorde, defecten, ‘trapping’ van ladingen en temperatuur. Alle C_n -BTBT- C_n ($n = 8, 10, 12$) derivaten vertonen een zogenaamde ‘herringbone’ moleculaire pakking die 2D-ladingstransportroutes introduceren. De temperatuurafhankelijkheid van de mobiliteit van de ladingsdragers en de vervalkinetiek in C_n -BTBT- C_n ($n = 8, 10, 12$) werden onderzocht door PR-TRMC-metingen. Voor deze verbindingen werden opmerkelijk hoge intrinsieke ladingsdragermobiliteiten van respectievelijk $2,94 \text{ cm}^2/\text{Vs}$, $3,02 \text{ cm}^2/\text{Vs}$ en $3,72 \text{ cm}^2/\text{Vs}$ verkregen. Analyse van de vervalkinetiek laat zien dat een groot deel van de zeer mobiele C_{12} -BTBT- C_{12} -ladingsdragers bij kamertemperatuur op een langere tijdschaal overleefde, in vergelijking met de andere verbindingen. Voor alle verbindingen is de mobiliteit van de ladingsdragers dramatisch verminderd bij lage temperaturen (tot -100°C), en de levensduur van de geleidingssignalen nam sneller af als gevolg van ladingsrecombinatie en toegenomen ‘trapping’. Dynamische en statische afwijkingen van de oorspronkelijke perfecte kristallijne arrangementen leiden tot hindering van ladingstransport bij alle temperaturen. Dit versterkt het argument voor een thermisch geactiveerd hopping-model als

het primaire mechanisme voor ladingstransport in C_n -BTBT- C_n ($n = 8, 10, 12$) verbindingen.

In **Hoofdstuk 5** beschrijven we een reeks polyamiden waarin waterstofbruggen tussen verschillende polymeerketens gevormd kunnen worden en beschrijven we hun opto-elektronische eigenschappen. De polyamiden hebben in hun zijketens ofwel p-type bithiofeen ofwel n-type dicyanoperyleenbisimide als elektronisch actieve groep. We vinden dat dergelijke materialen de thermochemische eigenschappen van typische semi-aromatische ‘engineering’ polyamiden combineren met een aanzienlijke mobiliteit van ladingsdragers. PR-TRMC-resultaten tonen aan dat de lengte van de alifatische spacer geen significante invloed heeft op het intra-columnaire ladingstransport in dergelijke polyamidederivaten. Zowel bithiofeen- als dicyanoperyleenbisimide bevattende polyamiden vertoonden echter verhoogde waarden voor de mobiliteit van ladingsdragers in vergelijking met hun analogen in de literatuur, wat wijst op het gunstige effect van waterstofbruggen op de pakking van π -geconjugeerde systemen en daarmee op de ladingstransporteigenschappen van de materialen.

Acknowledgement

Life is a journey full of flat roads and huge mountains. It was one of my best decisions to buy that Sony camera in 2014 summer with a free flight ticket to anywhere in Europe in any time. I have used this ticket in the right time to meet great scientists in the Netherlands that I admire their work, and eager to be a part of their team as a PhD student. That trip was, no doubt, one of the most satisfactory and life-changing trips of my life. Just after my MSc studies, I was enjoying the feeling of happiness, proud and relief as in walking down the hill after a long climbing. Here today, while writing the last bit of my PhD thesis, I am feeling exactly in the same way. Indeed, this part of the journey was longer and more challenging. It enhanced my knowledge, broadened my horizons, and shaped my personality. And these would not happen without those who contributed to this journey with all unforgettable, amazing memories.

I would like to express my gratitude to my supervisors **Ferdinand C. Grozema** and **Rienk Eelkema**. I would like to thank you both for giving me the opportunity to pursue my PhD studies in the groups of Optoelectronic Materials and Advanced Soft Matter Sections at TU Delft. I do appreciate the privilege of being a part of such bright, diverse, scientifically, and socially engaged groups. I have learnt the most valuable thing from you both: How to be and think like an independent scientist / researcher.

Ferdinand, thanks for keeping your door always open, being my go-to person, having your research team at your house in every Christmas and cooking delicious foods for us for hours. I know I was not the most likable PhD student of yours, but hopefully I was not so bad & annoying.

☺ Beside everything you do, you also work on your personal growth which made you a great model for me. I would recommend everyone to have some passionate scientific discussions, and light conversations with you to feel energized.

Rienk, thanks for being there for me whenever I needed scientific support, challenging me, showing me how to be comfortable with asking questions and giving direct answers. Your scientific integrity and passion for open science as well as publishing the failures is inspiring. Thanks a lot for your generous patience and understanding on my mess in my fume hood— running 2 colorful reactions at a time recommendation did not help much with it though. ☺

I would love to appreciate **Stephen Picken**, for being a part of my defense committee, and especially for teaching me POM, discussing XRD data with me, and for his awesome personality. The joy of having out-of-box brainstorms, learning science and chemistry behind everything from you and talking about music with you is priceless. Furthermore, I'd love to extend my sincere gratitude to **Walter Jager**. I am thankful for your expert advice, support, guidance, and kindness, discussing my research with me, clearing any doubts of mine on choosing the right synthetic routes and providing the right references at any time and day during my PhD research. Having you close by was a great privilege of mine.

I would like to thank all the members of the defense committee, **Jan van Esch, Laurens Siebbeles, Antonia Denkova, Dirk Vanderzande** for their critical evaluation of my thesis. I would like to express my special thanks to **Arjan Houtepen** for all continuous help, support, diverse conversations over science and life.

I have had more than four wonderful years with so many friendly, talented, bright scientists & engineers being around at Optoelectronic Materials and Advanced Soft Matter groups. I will miss my laboratory and office mates. I feel deeply happy and lucky to have you in my life as my friends.

Jos, my friend, my brother, thank you very much for being my fun laboratory-buddy. It is great having you close by in good and bad times. Thankfully you are not in Turkey, so you are not in jail because of your fabulous Erdogan jokes. **Vasu**, my brother, my friend, it was such a pure joy to work on soft robotics at nights with you and hearing your multilanguage songs.

Rajeev, we shared the pain and gain of colorful synthesis together. I do hope to dance and attend conferences with you and having your support and smile around more. There are some people we understand at the first sight that we have a special bond. **Alexandra, Qian and Meng**, you are one of them. Thank you very much for sharing the late nights and weekends in the department & in Delft, and joyful dinner tables with card games together.

Lars, Ruben, Ben, Jos, Nick, Marcel, Duco, Stephen, Xiaohui, Lennart, thank you very much for all technical support, help and joyful moments together. **Veby & Adinda**, thank you very much for solving all my management issues swiftly, and dealing with all the paperwork, highly appreciated.

Crazy cool chemists, ASMers, **Eduardo, Susan, Sander, Bowen, Michelle, Angie, Fanny, Tobias, Peggy, Reece, Benjamin, Elmira, Guotai, Yiming, Hendrik, Irene, Sarah, Reece, Suellen, Vincent, Walter, Chandan, Eduardo, Roman, Matija, Serhii, Tomasz,**

laboratory, office, conferences, group presentations, scientific discussions, poster sessions, coffee breaks, lunches, parties would not be that fun without you all. Thank for your very much for all fruitful conversations, colorful moments & borrels together. I will always remember our Sinterklaas gatherings with a big smile. And I will be missing the “We heard this song and the artist enough Cansel, change!” DJ of the lab very much. ☺

My dear OMers, **Damla, Sudeep, Hamit, Jence, Dengyang, Ryan, Gianluca, Aditya, Prashant, Davide, Frank, Ward, Valentina, Tom, Nick, Francesca, Maryam** thank you very much for your great company in the laboratory, department, breaks, group presentations, scientific discussions, trips, borrels and conferences.

Michele, Kevin, Magnus, Nico, Jaco, Silke, my dearest office mates, thank you very much for your great company and generous support during my research. PhD is, definitely!, permanent head damage with awesome people in it.

Maria, Solrun, Eline, I will miss our passionate talks over feminism, climate, academia, science, system at our dinners together so much. It was an awesome empowerment to be surrounded by awesome scientists, learning from each other, and having your support.

My dearest expat family in the Netherlands, **Gözde**, my sister, thank you very much for being in my life in all good and bad times. Having you close by is one of my biggest lucks in here. And without you, how could I see and learn about a quantum computer?? Thank you very much for introducing **Mario** to me, my deepest love, as well. **Fatma, Aytaç, Hakan, Cevdet, Yasemin**, one of our brainstorm over dinners and drinks will save the future but I don't know which one. Thanks a lot for your great

company. **Muscan**, thanks for being my water, your nurturing, fun friendship and supportive partnership in my life, career, passions, and ambitions for 3 years.

Herre, Davide, Maria, Diana in Physics Department, I deeply enjoyed our collaboration and partnership on break junction projects. Thank you very much for all fun and fruitful discussions, brainstorming, times together and our friendship.

My lovely 1st year students and BSc and MSc students **Anthea & Ariwan**, the most fulfilling and satisfactory moments of my whole PhD journey was seeing the happiness, passion, and light in your eyes in our times together in the lab, and hearing that you want to continue in STEM. I have also learnt a lot from you all, thank you very much for your all contribution, efforts, being my fuel and fun times together! (And sorry for my rigid attitude from time to time, safety first and you are more important than any reaction...) Wishing you all the brightest future. Keep in touch.

Canım ailem, my beautiful family, **Aysel, Yusuf, Yuksel, Selma, Marcel**... I couldn't do it without you, without your continuous emotional, personal, and professional support and unconditional love. **Mommy, annecim**, and **daddy, babacim**, any word or anything is not enough to express my gratitude to you. You both worked and sacrificed a lot for me and for my brother. Thank you very much for everything you have done for me. **Annecim**, thanks a lot for being my rock all the time, taking all the responsibilities from my shoulders especially in the moments when I was not able to carry, and making me happy and laugh even in the moments you were not happy. You are one of my biggest role models in my life. **Babacim**, knowing that whatever happens in life I have your unconditional

love and support in any time is my pure luck. Daddy, get ready for the photo - your daughter and son have their PhDs! 😊

Mevsim, Cansu, Bengisu, Pinar, Irem, our sisterhood bond, forever together!!

I'm sure and I do know that I have missed many more amazing people and highly valuable names in here. I sincerely acknowledge you all, thank you very much for everything. I seriously should stop writing. 😊

List of Publications

- 1- Engineering polymers with improved charge transport properties from bithiophene-containing polyamides, Özen, B., N. Candau, **C. Temiz**, F.C. Grozema, F.F. Tirani, R. Scopelliti, J.M. Chenal, C. J.P. Plummer, H. Frauenrath, *J Mater Chem C Mater*, 2020, **8**, 6281–6292.
- 2- Semiaromatic polyamides with enhanced charge carrier mobility, Özen, B., N. Candau, **C. Temiz**, F.C. Grozema, G. Stoclet, C. J.P. Plummer, H. Frauenrath, *Polym Chem*, 2021, **12**, 6914–6926.
- 3- Synthesis & Optical Spectroscopy of Discotic Hexa-*peri*-hexabenzocoronene Derivatives: Self-Assembly Properties of Molecular Nanowires in Solution, **C. Temiz**, E. Galan, R. Eelkema, F.C. Grozema, *in preparation*.
- 4- Supramolecular Organization and Charge Transport Properties of Hexa-*peri*-hexabenzocoronene Derivatives: Self-Assembly Molecular Nanowires in the Solid State, **C. Temiz**, R. Eelkema, F.C. Grozema, *in preparation*.
- 5- Effect of substituent groups on quinoxaline-based random copolymers on the optoelectronic and photovoltaic properties, S.C. Cevher, G. Hizalan, **C. Temiz**, Y.A. Udum, L. Toppare, A. Cirpan, *Polymer*, 2016, 101, 208-216.

List of Awards

Best Poster Prize, European Conference of Molecular Electronics (ECME), 2017, Dresden / Germany

Most outstanding student, International Fall School on Organic Electronic (IFSOE), 2016, Moscow / Russia

About the Author

Cansel Temiz was born in Ankara, Turkey in 1990. She received her Bachelor of Science in Chemistry starting from 2008 till 2013 at Middle East Technical University. During her BSc, she did internships in Novartis, Pfizer and Prof. Dr. Guiducci's research group at EPFL with the focus on biotechnology and pharmaceuticals coming from her passion to find some solutions and help people in need. In her last year of BSc, she worked in nature-inspired bio-based polymers in Prof. Dr. Volkan's research group and decided to continue in sustainability and polymer science. Between 2013-2015, she pursued her Master of Science in Polymer Science and Technology under the supervision of Prof. Dr. Toppare and Prof. Dr. Cirpan at Middle East Technical University. She worked on synthesis and characterization of organic random copolymers for polymer solar cells and organic light emitting diodes. Later, she moved to the Netherlands to continue her academic career. She started her PhD in October 2015 in the department of Chemical Engineering / Applied Science at TU Delft under the supervision of Prof. Dr. Grozema and Dr. Eelkema.

Propositions

Belonging to the thesis, entitled
**Unraveling the Relationship Between Molecular Design and Charge
Transport in Self-Assembling Systems**

By

Cansel TEMIZ

1. Combining computational and experimental studies increases scientific progress in any field.
2. A promising approach to achieve high charge transport efficiencies in discotic supramolecular materials is to control the supramolecular organization through modification of the side chains of the individual molecules.
Adv. Funct. Mater., 15, 893-904 (2005)
3. Purification and crystal growth techniques are vital to develop materials exhibiting high charge carrier mobilities.
(Chapter 2 & Chapter 3)
4. Pulse-radiolysis time-resolved microwave conductivity (PR-TRMC) is a suitable method to measure the charge carrier transport mechanism of soft organic materials without having to deposit electrodes or constructing a full device.
Chapter 4
5. Any world leader attending the climate change conferences with private jets should be excluded from decision making processes.
6. PhD process should be allowed to proceed without an obligation of PhD Thesis. Instead, publishing a review paper related to the PhD topic should be made mandatory to increase the knowledge, confidence, contribution, and scientific research skills of the PhD candidates in the first years.
7. Putting the social pressure of being normal onto individuals is a big part of conservative cultures trying to have control and power over

individuals. Young generations, at any time and in any culture, should question the norms, who defines them and the reasons to follow them.

8. There should be one fixed and automated formatting style for all scientific journals to increase the efficiency of publication processes and to make the life of researchers easier.
9. In a system where academics prioritize their names, titles and impact factors over genuine scientific inquiries and outcomes, it is clear that the system is corrupted.
10. 'The best female scientist' awards in Dutch national science conferences need re-evaluation to align with modern principles of gender-neutral and egalitarian ethos within the realm of science. Rather than fostering support and recognition, such distinctions inadvertently diminish the credibility and standing of women in the scientific community.

These propositions are regarded as opposable and defensible, and have been approved as such by the promotor Prof. dr. F.C. Grozema and Dr. R. Eelkema

